Research Activities

– Synchrotron Radiation Experiments –

The electronic structure of O-Fe(001) thin films grown on MgO(001) studied by angle-resolved photoelectron spectroscopy and density functional theory

Mingtian Zheng[a], Eike F. Schwier[b] and Kenya Shimada[b]

[a]*Graduate School of Science, Hiroshima University, Higashi-Hiroshima 739-8526, Japan*
[b]*Hiroshima Synchrotron Radiation Center, Hiroshima University, Higashi-Hiroshima 739-0046, Japan*
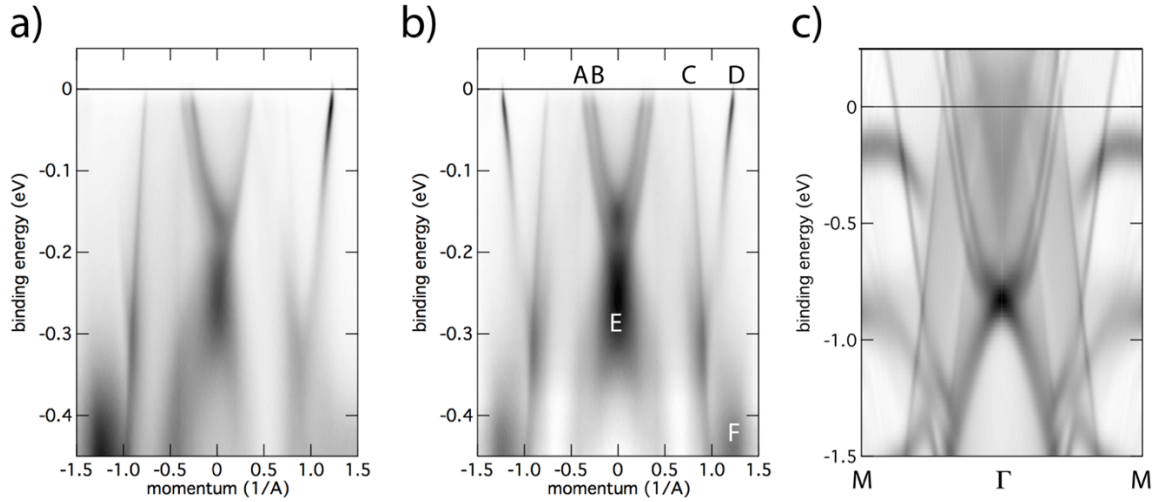
Keywords: Magnetism, Angle Resolved Photoelectron Spectroscopy, Density Functional Theory, Surface States

O-Fe(001) thin films grown on MgO(001) have attracted much interest within various areas of research. It has been investigated for the magnetic tunneling junctions (Fe-MgO-Fe) where the interface is made up of O-Fe bonds [1]. The oxygen adsorbed Fe(001) surface can work as a highly efficient spin filter, and has been used in the Very-Low-Energy Electron Diffraction (VLEED) based spin ARPES machines [2]. From a more fundamental point of view the correlated nature of the Fe $3d$ electrons is of interest.

In a previous study we found that O adsorption vastly reduces the scattering rate for photoelectrons, allowing an unobstructed view on the electronic structure of surface [3] and bulk [4] states alike. Leading to the extraction of self-energy information related to both electron-phonon and electron-electron(magnon) many-body interactions. Here, we report a detailed comparison between high quality ARPES data and our recent density functional theory calculations (DFT).

In Figure 1 a) we show an ARPES spectrum at a selected photon energy of 50 eV along the $\overline{\Gamma}\overline{M}$ - direction measured in the *p*-polarization geometry (*p*-pol) at BL-1 of HiSOR [6]. This spectrum was chosen from several photon energy, polarization and high-symmetry direction dependent measurements as it shows most of the bands present in the system. We symmetrized the spectrum with respect to the momentum origin as a guide-to-the-eye in Figure 1b), while the following discussion is based on a detailed analysis of the raw intensity of Figure 1 a). At least four bands can be identified to cross the Fermi level. Two electron-like bands around the $\overline{\Gamma}$ -point (A and B) and two almost linear bands close to the $\overline{M}$ -point (C and D). At a binding energy of ~250 meV, an additional hole-like band is situated at the $\overline{\Gamma}$ -point (E) and at 500 meV a flat band is visible at the $\overline{M}$ -point (F). In the current geometry ($\overline{\Gamma}\overline{M}$ and p-pol) the following orbitals can be detected in the ARPES spectrum: Fe $3d$ ($3z^2$-r^2, xy, $[x+y]z$) and O $2p$ (z and $x+y$). These basis functions do not change their sign under the symmetry operation of $x \rightleftarrows y$. The Fe $3d_{[x+y]z}$ and O $2p_{[x+y]}$ can be obtained by a linear combination of the orthogonal complex basis vectors $3d_{xz}$ and $3d_{yz}$ and $2p_x$ and $2p_y$ respectively. This linear combination is necessary in order to obtain an orthogonal basis set of pure even and odd symmetries with regard to the $\overline{\Gamma}\overline{M}$ high symmetry measurement direction.

Having obtained such high quality data, we used DFT to calculate the electronic structure of a 41 ML thick Fe(001) slab covered with a p(1×1) O layer. DFT calculations were performed using the openMX code [7]. The slab was constructed from a fully relaxed bulk Fe lattice structure and the atomic positions in the slab where sub sequentially relaxed with residual force being smaller than 10^{-4} Bohr/Hartree. By analyzing the overlap matrix elements as well as the LCAO coefficients of the resulting Kohn Sham Hamiltonian, the contribution of each orbital of each atom to the spectral weight can be estimated. This method allows to determine the orbital hybridization as well as spin structure of the surface and more bulk-like regions deeper inside the slab. In the current analysis however, we focus on the contribution from the surface region alone. By combining orbitals with even symmetry with respect to the $\overline{\Gamma}\overline{M}$ high symmetry direction a simulation of spectral weight can be obtained and compared to the high resolution ARPES measurements.

FIGURE 1: a) Raw ARPES spectrum of O-Fe(001): p(1×1) surface obtained along the $\overline{\Gamma M}$ -direction in *p*-polarization geometry. b) Same as a) but symmetrized around k=0. c) Calculated orbital weight along the $\overline{\Gamma M}$ -direction with *p*-polarization geometry.

In Figure 1 c) the resulting orbital weight of the DFT calculation is plotted. The image plot is a summation over all orbitals of even symmetry within the topmost 4 atoms including oxygen. Comparing the DFT band structure with ARPES, it becomes clear that the electron pockets and hole pockets are well described qualitatively, but not quantitatively in energy. While all bands (A-F) of the ARPES spectrum can be matched to the DFT calculation, the theoretical binding energy of the electron- (A and B) and holepocket (E) around the $\overline{\Gamma}$ -point is too high by a factor of ~3. The energy of the electron pockets at the $\overline{M}$ -point is also increased by a factor of 3, if one considers the crossing point of C and D as a reference (ARPES ~300 meV vs DFT ~900 meV). The binding energy of the flat band (F) around the $\overline{M}$ -point deviates by a factor of ~2.

This difference of calculated and experimental binding energies can be explained as a result of mass-enhancement due to the correlated nature of Fe 3*d* orbitals. Indeed, in a previous study [8], the mass enhancement in bulk Fe(110) was estimated to be $m/m_0 \sim 3$. However, mass enhancement usually does not result in a change of the k_F value of bands. There is however a discrepancy between bands A and C, whose k_F values predicted by the DFT are much closer than in the ARPES spectrum. An explanation for this discrepancy could be the effects of the charge transfer between oxygen and the finite iron slab as well as effects related to a DFT functional dependent over- or under-estimation of exchange splitting. Since calculated magnetic moment at the surface (~3 μ_B at the topmost Fe compared to ~2.1 μ_B inside the slab) is significantly enhanced at the surface, the latter possibility has to be considered.

Such effects might also be responsible for the presence of the occupied hole-like band at the $\overline{M}$ -point with a binding energy of ~200 meV that is not found in the ARPES spectrum. The character of the band is highly surface dependent and can be identified to be a surface state decoupled from a bulk state with a binding energy of ~ 1 eV (which was matched to band F in the ARPES after mass renormalization). Such a surface band might become unoccupied as a result of more realistic description of the charge compensation between the different orbitals at the surface and their magnetic moments.

Based on such promising matching between theory and experiment, the next steps of analysis will be the comparison of charge transfer effects between oxygen and iron. An analysis of orbital hybridization based on the calculated band structure as well as a comparison with fully relaxed clean Fe(001) slabs is underway and expected to shine further light on the experimental findings.

REFERENCES

1. A. Cattoni *et al.*, Physical Review B **80**, 104437 (2009).
2. T. Okuda *et al.*, Review of Scientific Instruments **82**, 103302 (2011).
3. M. Zheng *et al.*, HiSOR Activity reports for proposal numbers 13-A-39, 14-A-52, 15-A-64.
4. HiSOR Activity reports for proposal numbers 16AG038
5. H. Iwasawa et al., J. Synchrotron Rad. **24**, 836–841 (2017).
6. http://openmx-square.org
7. X.Y. Cui et al. Physical Review B **82**, 195132 (2010)

2-dimensional Surface Bands in $Pb_{1-x}Sn_xTe$ Thin Films

Ryota Akiyama[a] Yusuke Otaki[b], Yuta Tomohiro, Keita Miyauchi, Ryosuke Nakanishi[a], Ryo Ishikawa[b], Tomonari Yamaguchi[b], Hitoshi Sato[c], Akio Kimura[d], Eike F. Schwier[c], Koji Miyamoto[c], Kenya Shimada[c], Shuji Hasegawa[a], and Shinji Kuroda[b]

[a]*Department of Physics, The University of Tokyo, Tokyo, Japan*
[b]*Institute of Materials Science, University of Tsukuba, Tsukuba, Japan*
[c]*Hiroshima Synchrotron Radiation Center, Hiroshima University, Hiroshima, Japan*
[d]*Department of Physics, Hiroshima University, Hiroshima, Japan*

Keywords: Topological insulator, Topological crystalline insulator, Spin-orbit interaction, 2D material, Thin film
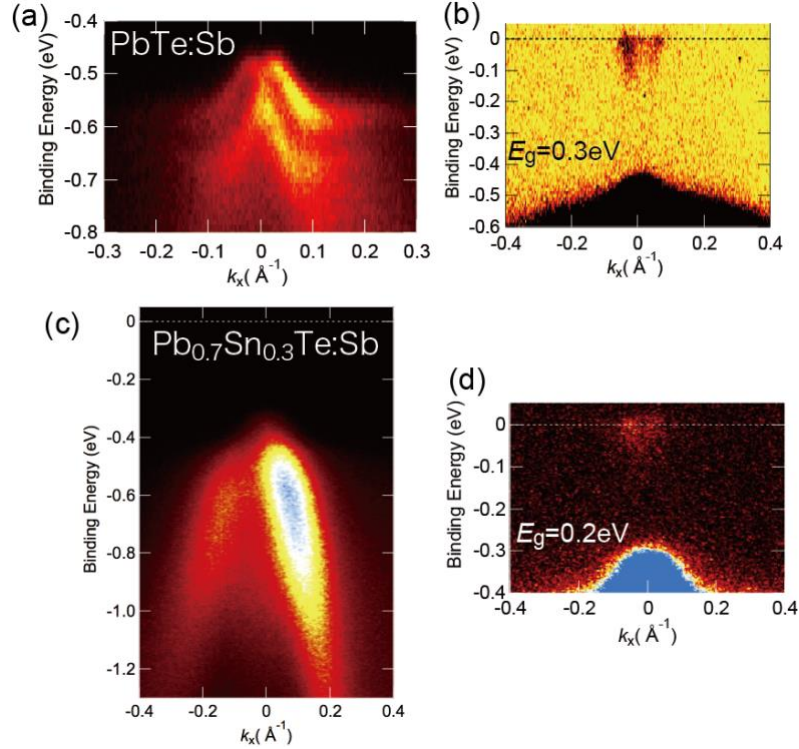
Topological insulators (TIs) are the new class of materials and have been investigated intensivly these days because of their abundant interesting and novel properties such as spin-momentum locking, spin-split band, Dirac Fermion, and Majorana Fermion. In 3-dimensional TIs, the surface state is metallic whereas the bulk is insulating and has a linear band dispersion of a Dirac cone. Such surface state is called the topological surface state (TSS), and the band is split for each spin except for the Kramers degeneracy points ($k = 0$). The TSS is protected by the time-reversal symmetry and induced by the band inversion due to the strong spin-orbit interaction.

Topological crystalline insulators (TCIs) are the group of TIs, but the TSS of TCIs is protected by the crystal mirror symmetry instead of the time-reversal symmetry. As typical TCI materials, SnTe[1], SnSe[2], $Pb_{1-x}Sn_xTe$[1], $Pb_{1-x}Sn_xSe$ [3] have been proposed and confirmed. The band characteristics of the TSS in SnTe were demonstrated experimentally by the angle-resolved photoemission spectroscopy (ARPES) with bulk crystals of (001) and (111) orientation in 2012 and 2013, respectively[1,4]. On the other hand, the electrical transport was measured in the thin films so far[5-8]. However, it has been difficult to obtain the TSS of SnTe directly because SnTe tends to be heavily doped p-type. Especially, the detailed TSS of the thin film $Pb_{1-x}Sn_xTe$ (111) is unclear so far because there is almost no systematic investigation with changing the incident photon energy (PE).
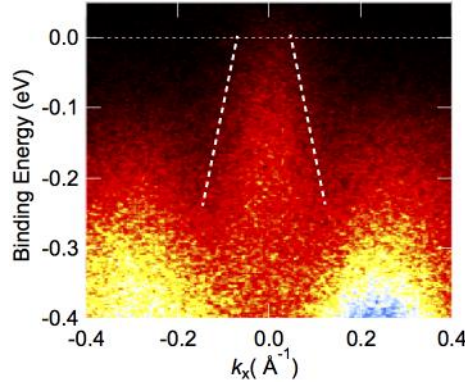
We have found that the Fermi level tuning by Sb doping can be realized and investigated the 2-dimentional transport characteristic in Sb-doped $Pb_{1-x}Sn_xTe$ so far. In this research, we aim to observe the surface band, particularly Dirac point, directly by ARPES. In TCIs, there is almost no work to check the change of the Dirac cone by doping magnetic atoms. This is mainly because we can not see the surface band around the Dirac point clearly due to heavily p-type nature. Thus, the mechanism of the gap opening in TCI is still unknown experimentally. If we investigate the gap with respect to such as quantum anomalous Hall effect (QAHE), the effective tuning of the Fermi level is essential.

The band inversion of the valence and conduction band at L point occurs in $Pb_{1-x}Sn_xTe$, and it is required to realize the TSS. According to the previous reports, it occurs and the TSS persists with $x > \sim 0.25$. We confirmed that the carrier compensation occurs with doping Sb by electrical transport measurements. The carrier density is changed with changing Sb concentration. Especially, $Pb_{0.6}Sn_{0.4}Te$:Sb can be tuned to both p and n-type conduction. Thus, we tuned the Fermi level in the sample for ARPES to see the surface band and to be topologically non-trivial by optimizing Pb content. Figures 1(a) and (c) show ARPES images of Γ-M dispersion observed at PE of 60 eV in PbTe:Sb and $Pb_{0.7}Sn_{0.3}Te$:Sb thin films. Intriguingly, the valence band shows Rashba-like splitting in the case of PbTe:Sb as shown in Fig. 1(a). Around this binding energy, no similar bulk band is reproduced by calculations but some surface spin split bands exist. The precise band coordination is sensitive for the termination and it has not been decided yet. Figure 1(b) and (d) represent the enlarged and the contrast-tuned images to see the vicinity of the band gap well. The conduction band is observed their band gaps are 0.25 and 0.3 eV in PbTe:Sb and $Pb_{0.7}Sn_{0.3}Te$:Sb, respectively. Although the

intensity of the surface band in $Pb_{0.7}Sn_{0.3}Te$:Sb is not so strong, but it is surely observed in PE of 105 eV as shown as white dot lines in Fig.2. This band is unchanged with changing PE, which indicates the 2-dimensional band nature. It is suggested that the reason why the surface band at PE = 60 eV is not seen clearly is because the surface band of TIs is often easy to be seen at lower PE than 60 eV; the lower or higher energy is better to see the surface band in this system.

FIGURE 1. ARPES images of Γ-M dispersion observed at the incident photon energy of 60 eV in PbTe:Sb **(a,b)** and $Pb_{0.7}Sn_{0.3}Te$:Sb **(c,d)**, respectively.

FIGURE 2. ARPES images of Γ-M dispersion observed at the incident photon energy of 105 eV in $Pb_{0.7}Sn_{0.3}Te$:Sb **(c,d)**. The white dot lines represent the surface band.

REFERENCES

[1] Y. Tanaka, Zhi Ren, T. Sato, K. Nakayama, S. Souma *et al.*, Nat. Phys. **8**, 800 (2012).
[2] Z. Wang, J. Wang, Y. Zang, Q. Zhang, J.-A. Shi *et al.*, Adv. Mater. **27**, 4150 (2015).
[3] P. Dziawa, B. J. Kowalski, K. Dybko, R. Buczko, A. Szczerbakow *et al.*, Nat. Mat. **11**, 1023 (2012).
[4] Y. Tanaka, T. Shoman, K. Nakayama, S. Souma, T. Sato *et al.*, Phys. Rev. B **88**, 235126 (2013).
[5] A. A. Taskin, F. Yang, S. Sasaki, K. Segawa, and Y. Ando, Phys. Rev. B **89**, 121302 (2014).
[6] B. A. Assaf, F. Katmis, P. Wei, B. Satpati, Z. Zhang *et al.*, Appl. Phys. Lett. **105**, 102108 (2014).
[7] M. Safdar, Q. S. Wang, M. Mirza, Z. X. Wang, K. Xu, J. He, Nano Lett. **13**, 5344 (2013).
[8] R. Akiyama, K. Fujisawa, T. Yamaguchi, R. Ishikawa, and S. Kuroda, Nano Research **9**, 490 (2016).

Observation of the Eu $4f^6$ multiplet structure in EuPt$_2$Si$_2$ by angle-resolved photoemission spectroscopy

H. Anzai[a], E. F. Schwier[b], K. Shimada[b], H. Namatame[b], M. Taniguchi[b], A. Mitsuda[c], H. Wada[c], and K. Mimura[a]

[a] Graduate School of Engineering, Osaka Prefecture University, Sakai 599-8531, Japan
[b] Hiroshima Synchrotron Radiation Center, Hiroshima University, Higashi-Hiroshima 739-0046, Japan
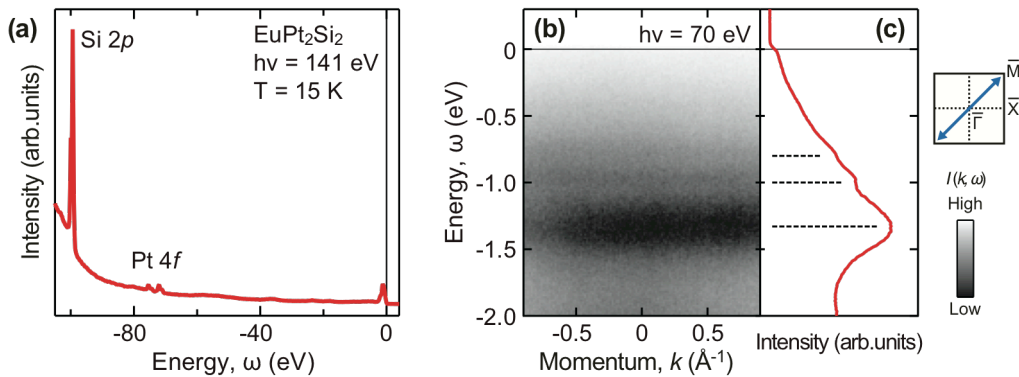[c] Graduate School of Science, Kyushu University, Fukuoka 819-0395, Japan

Keywords: c-f hybridization, Eu compound, angle-resolved photoemission spectroscopy.

EuPt$_2$Si$_2$ with CaBe$_2$Ge$_2$-type structure exhibits an antiferromagnetic order at 15 K and keeps a nearly divalent Eu state independent of temperature [1]. However, recent transport measurements have revealed that temperature dependence of the electrical resistivity cannot be understood by single simple explanation based on the Eu^{2+} ions [2,3]. Specifically, it is predicted that the competitive states among magnetic order, valence fluctuation and Kondo effect are associated with unusual response of the electrical resistivity [2,3,4]. To understand the behavior of the electronic properties in EuPt$_2$Si$_2$, it is essential to observe the electronic structure near Fermi level (E_F) and unveil the detailed of Eu $4f$ and conduction bands.

Angle-resolved photoemission spectroscopy (ARPES) is a direct probe to measure the band dispersions in energy and momentum spaces. Here, we report on a study of the electronic band structure of EuPt$_2$Si$_2$ obtained by ARPES with synchrotron radiation. The experiments were performed at BL-1 of the Hiroshima Synchrotron Radiation Center.

Figure 1(a) shows the photoemission spectra of EuPt$_2$Si$_2$ over a wide energy region taken with $h\nu = 141$ eV at $T = 15$ K. Intense peak at $|\omega| \sim 100$ eV originates from the Si $2p$ states. The spin-orbit split Pt $4f$ states are observed at ~72 and ~76 eV. The well-defined peak is identified at ~1 eV near E_F.

To understand the valence electronic structure, we performed ARPES measurements using $h\nu = 70$ eV photons. Figure 1(b) shows ARPES spectra, $I(k,\omega)$, taken along the $\bar{\Gamma}$-$\bar{M}$ direction of the surface Brillouin zone. Three flat bands are observed at $|\omega| \sim 0.8$, 1.0, and 1.3 eV. The bands at ~1.3 and ~1.0 eV are assigned to the surface contribution from the topmost and subsurface region of Eu^{2+} ions, respectively [5]. In contrast, the band at ~0.8 eV is the bulk components of the Eu $4f$ states [6].

Figure 1. (a) Photoemission spectra of EuPt$_2$Si$_2$ over a wide energy region. The data were obtained by using $h\nu = 141$ eV at $T = 15$ K. (b) ARPES spectra $I(k,\omega)$ near E_F taken with $h\nu = 70$ eV along the $\bar{\Gamma}$-$\bar{M}$ direction of the surface Brillouin zone, as marked at the right side of panel (c). (c) Angle-integrated spectra for the data in (b). The dashed lines represent the peak positions.

As shown by the angle-integrated spectra in Fig. 1(c), the photoemission intensity below $|\omega| \sim 0.8$ eV seems to be an oscillating character. A similar staircase-like structure near E_F was also observed in the photoemission spectra of Eu thin film on W(110) and assigned to the ^7F_J multiplet derived from the electron configurations of $4f^6$ final states [7]. Thus, we assume that the peak at ~0.8 eV is the $^7F_6$ terms.

The previous ARPES studies on $EuNi_2P_2$ with $ThCr_2Si_2$-type structure have revealed the hybridization effect between the ^7F_J ($J = 3$-6) terms and Ni $3d$ states [8]. In current study, we have not detected the conduction bands near E_F and their hybridization with the Eu $4f$ bands. More detailed experiments over wide momentum and temperature ranges are required to understand the energy balance among the antiferromagnetic ordering, the valence transformation and the Kondo effect in $EuPt_2Si_2$.

REFERENCES

1. R. Nagarajan *et al*., Physica B **163**, 591 (1990).
2. A. Mitsuda *et al*., Acta Phys. Pol. B **34**, 1149 (2003).
3. Y. Ikeda *et al*., J. Magn. Magn. Mater. 310, e62 (2007).
4. A. Mitsuda *et al*., Physica B **403**, 786 (2008).
5. T. Kinoshita *et al*., J. Phys. Soc. Jpn. **71**, 148 (2002).
6. K. Mimura *et al*., J. Electron Spectrosc. Relat. Phenom. **137**, 529 (2004).
7. G. Kaindl *et al*., Phys. Rev. B **51**, 7920 (1995).
8. S. Danzenbächer *et al*., Phys. Rev. Lett. **102**, 026403 (2009).

Low-energy heavy-fermion bands in YbCdCu₄ revealed by angle-resolved photoemission spectroscopy

H. Shiono[a], S. Ishihara[a], K. Mimura[a], H. Sato[b], E. F. Schwier[b], K. Shimada[b],
M. Taniguchi[b], S. Ideta[c], K. Tanaka[c], T. Zhuang[d], K. T. Matsumoto[d],
K. Hiraoka[d], and H. Anzai[a]

[a] Graduate School of Engineering, Osaka Prefecture University, Sakai 599-8531, Japan
[b] Hiroshima Synchrotron Radiation Center, Hiroshima University, Higashi-Hiroshima 739-0046, Japan
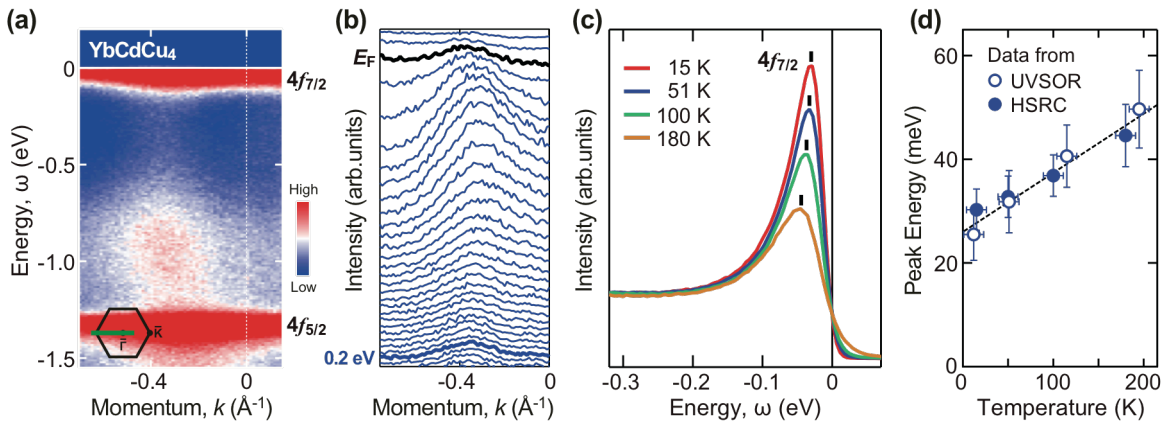[c] UVSOR Facility, Institute for Molecular Science, Okazaki 444-8585, Japan
[d] Graduate School of Science and Engineering, Ehime University, Matsuyama 790-8577, Japan

In rare-earth compounds, the hybridization effect between conduction and localized-$4f$ electrons (c-f hybridization) leads to the formation of heavy electrons, and it is characterized by a renormalized band structure near the Fermi level (E_F) [1]. According to the single-impurity Anderson model, a sharp resonance peak in the electronic excitation spectrum appears at the energy scales of the Kondo temperature T_K, which is a measure of the hybridization strength [2]. The intensity of the Kondo resonance exhibits a strong temperature dependence that reflects magnitudes of the c-f hybridization. Hence, temperature dependence of the Kondo resonance peak near E_F will provide important insights for understanding the heavy fermion state.

YbCdCu₄ with C15b-type structure is known as a heavy fermion compound with the electronic specific heat coefficient $\gamma \sim 175$ mJ/K^{2}mol [3,4]. The Kondo temperature is estimated to be $T_K \sim 220$ K from the magnetic susceptibility measurements [5,6]. To understand the heavy fermion behavior of YbCdCu₄, it is essential to observe the electronic excitation spectrum and unveil the detailed of the Yb $4f$ and conduction bands. Angle-resolved photoemission spectroscopy (ARPES) is a direct probe to measure the band dispersions in energy and momentum spaces. Here, we report on a study of the hybridization effect in YbCdCu₄ based on ARPES data near E_F. The experiments were performed at BL-1 of the Hiroshima Synchrotron Radiation Center (HSRC) and BL7U of the UVSOR facility.

Figure 1. (a) ARPES spectra of YbCdCu₄ taken along the $\bar{\Gamma}$-$\bar{K}$ direction at 15 K. The data were obtained using $h\nu = 50$ eV photons at BL-1 of the HSRC. (b) Momentum distribution curves near E_F. (c) Angle-integrated spectra at various temperatures. The vertical bars indicate the peak positions. (d) Energy shift of the Yb^{2+} $4f_{7/2}$ peak shown in panel (c), together with the data obtained in the UVSOR facility. Dashed line represents the result of the linear fits.

Figure 1(a) shows ARPES spectra of YbCdCu$_4$ taken along the $\overline{\Gamma}$-$\overline{K}$ direction of the surface Brillouin zone. Two flat bands at $|\omega| \sim 0.02$ and 1.3 eV are assigned to the spin-orbit split Yb^{2+} $4f_{7/2}$ and $4f_{5/2}$ states, respectively. A dispersive band was observed over an energy range of $0.1 < |\omega| < 1.2$ eV. This conduction band intersects with the $4f_{7/2}$ state and reaches E_F, as seen from the peaks of momentum distribution curves in Fig. 1(b). Thus, Fermi surface of YbCdCu$_4$ at least consists of one hole band around the $\overline{\Gamma}$ point.

For quantification of the hybridization strength, we investigated the temperature dependence of the $4f_{7/2}$ state. Figure 1(c) shows the temperature dependence of the $4f_{7/2}$ peak. We found an energy shift and an intensity enhancement of the $4f_{7/2}$ peak with decreasing temperature. It is noteworthy that integrated spectral intensity of the peak is not conserved, and this behavior is incompatible with the simple thermal broadening of the metallic density of states. In contrast, the temperature evolution of the $4f_{7/2}$ peak is consistent with the prediction of the single-impurity Anderson model [2]. The observed $4f_{7/2}$ peak near E_F can therefore be assigned to the Kondo resonance peak in YbCdCu$_4$.

The sharpness of the $4f_{7/2}$ peak is sufficient even at 180 K and thus allows for precise determination of the peak energy. Figure 2(b) shows the energy of the Kondo resonance peak as a function of temperature, together with the data obtained in the UVSOR facility. The results coincide with each other within the error bars, indicating the consistency of our experimental data. The peak energies decrease linearly with decreasing temperature. The appearance of the Kondo resonance at $k_B T_K$ in the limit of zero temperature represents the formation of the singlet ground state [2]. Thus, we have estimated the energy scale of the Kondo temperature at $T = 0$ K. As shown by the dashed line in Fig. 2(b), the energy extrapolated to $T = 0$ K is estimated as ~ 26.5 meV, which corresponds to $T_K \sim 308$ K. This value is approximately consistent with T_K obtained by the magnetic susceptibility measurements [5,6]. This consistency demonstrates that the heavy fermion behavior of YbCdCu$_4$ stems from the hybridization between the observed $4f_{7/2}$ and conduction bands. Further experiments over wide momentum and temperature ranges are required to understand the mechanism of the heavy fermion behavior of YbCdCu$_4$.

REFERENCES

1. A. N. Tahvildar-Zadeh, M. Jarrell, and J. K. Freericks, Phys. Rev. Lett. **80**, 5168 (1998).
2. N. E. Bickers, D. L. Cox, and J. W. Wilkins, Phys. Rev. B **36**, 2036 (1987).
3. K. Hiraoka K. Kojima, T. Hihara, and T. Shinohara, J. Magn. Magn. Mater. 140, 1243 (1995).
4. J. L. Sarrao, C. D. Immer, and Z. Fisk, C. H. Booth, E. Figueroa, and J. M. Lawrence, R. Modler,
   A. L. Cornelius, M. F. Hundley, G. H. Kwei, and J. D. Thompson, F. Bridges, Phys. Rev. B **59**, 6955 (1999).
5. T. Koyama, M. Matsumoto, T. Tanaka, H. Ishida, T. Mito, and S. Wada, Phys. Rev. B **66**, 014420 (2002).
6. I. Felner and I. Nowik, Phys. Rev. B **33**, 617 (1986).

Disturbance Influence on Conduction Pathway for Electron Carriers Doped near Anatase TiO$_2$ Surface

Yoshihiro Aiura,[a] Kenichi Ozawa,[b] Eike F. Schwier,[c] and Kenya Shimada[c]

[a]*Electronics and Photonics Research Institute, National Institute of Advanced Industrial Science and Technology (AIST), Tsukuba, Ibaraki 305-8568, Japan*
[b]*Department of Chemistry, Tokyo Institute of Technology, Meguro, Tokyo 152-8551, Japan*
[c]*Hiroshima Synchrotron Radiation Center, Hiroshima University, Higashi-Hiroshima, Hiroshima 739-0046, Japan*
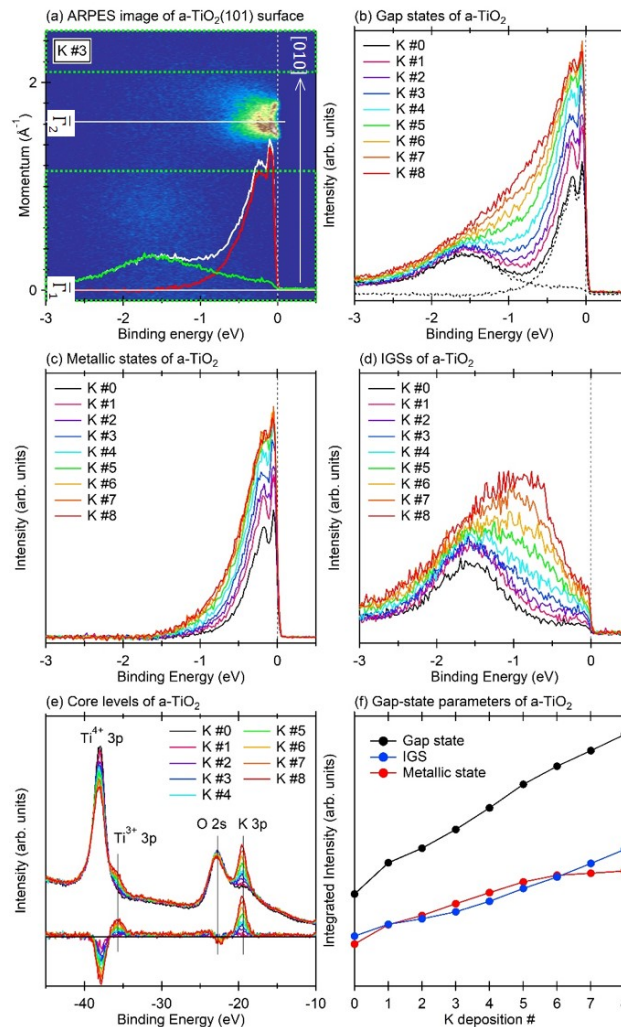
TiO$_2$ is one of the most important oxide materials used in applications such as photocatalysis [1]. Naturally grownTiO$_2$ exists in three different polymorphs rutile, anatase, and brookite, and it is well known that anatase TiO$_2$ (a-TiO$_2$) shows a higher catalytic activity than rutile phase. Since such photocatalysis is closely related to the semiconducting properties, the microscopic electronic structure has been actively studied by means of various spectroscopies. By irradiating ultraviolet (UV) light, it is well known that oxygen vacancies are easily generated on TiO$_2$ surfaces that are closely related to the photocatalysis [1]. Therefore, elucidating the microscopic behavior of the electrons doped by the oxygen vacancies near the surface will be crucial to understand its photocatalytic properties. For a-TiO$_2$, a metallic surface state, the so-called two-dimensional electron gas/liquid (2DEG/L), was reported to be formed upon irradiating with UV-light [2]. Such UV-light irradiation induces oxygen vacancies in the conduction pathway near the surface, and so, the electronic behavior of the doped electrons is considered to be directly affected by the oxygen vacancies. Recently, such a 2DEG/L was also observed by depositing potassium on the a-TiO$_2$ surface [3]. Since the potassium ions are deposited on the surface, the doped electrons are supposed to be affected only by loose and indirect disturbances in the conduction pathway. As inferred from a previous study of cuprate [4], the physical properties of oxides such as the semiconducting/conducting and catalytic properties are considered to be sensitive to the conduction pathway. In order to understand the disturbance influence on the conduction pathway for the electron carriers doped near the a-TiO$_2$ surface, the electronic states induced by depositing potassium were studied by means of photoemission spectroscopy (PES). Based on a simple band picture [5], the electrons doped into a-TiO$_2$ are supposed to conduct through a pathway of the antibonding bands composed of the Ti 3d$_{xy}$ and oxygen 2p orbitals, which are located at the conduction band minimum. The electrons doped by deposing potassium mainly occupy the metallic state just below the Fermi level (E_F), and are considered to be the carriers responsible for the conductivity. The remaining small number of electrons are loosely trapped near the potassium ions at the surface, and form a (dispersion-less) localized state with a finite spectral intensity at E_F, which contributes in part to the surface conductivity. Elucidating the disturbance influence on the conduction pathway for the doped electron carriers of a-TiO$_2$ is crucial for understanding the catalytically and semiconducting properties such as the mobility and dopability of the electron carriers.

Single crystals of a-TiO$_2$ grown naturally were used (SurfaceNet GmbH, Germany). Although the ideal stoichiometric a-TiO$_2$ should be an insulator based on band calculations [5], the naturally grown a-TiO$_2$ used in this study is a semiconductor, with a mobility of 1.3 cm^{2}V^{-1}s^{-1} estimated from Hall measurement. Since no impurity was detected from X-ray fluorescence spectroscopy and energy dispersive X-ray spectroscopy, it is believed that the conduction properties are a result of the electron carriers derived from the oxygen vacancies in the bulk. The orientation of the a-TiO$_2$ surface was set to be the naturally cleaving (101) plane. The momentum direction shown in the angle-resolved photoemission spectroscopy (ARPES) images was set to the [010] axis. To prevent the composition from deviating from the bulk value, clean surfaces were obtained by fracturing the single crystal in situ below a pressure of 10^{-8} Pa. PES measurements were performed using BL-1 of Hiroshima Synchrotron Radiation Center (HiSOR) [6]. In order to simultaneously detect not only the valence bands including the gap states but also the shallow core levels such as O 2s, Ti

3p, and K 3p, the photon energy was set as 100 eV. Linearly polarized synchrotron radiation (SR) in the horizontal plane of incidence, i.e., that is, in *p*-polarization geometry, was used. The PES spectra were normalized with the focusing mirror current. The valence bands and gap states were measured in the angular mode, whereas the shallow core levels such as K 3p, O2s, and Ti3p were recorded in the transmission mode. The energy distribution curves (EDCs) of the valence band and gap states were obtained by integrated the ARPES spectra along the acceptance angle of the energy analyzers. The spectra were taken at 20 K. The instrumental energy resolution due to the energy analyzer and the SR was about 70 meV.

FIGURE 1. PES spectra of a-TiO$_2$ (101) surface after potassium deposition. (a) Example of an ARPES image after potassium deposition, corresponding to K #3 in Figure (f). The ARPES image was recorded along the [010] direction. (b) Potassium deposition dependence of the gap states. The gap states are deconvoluted into metallic states and IGSs, as shown by the dotted lines. (c) and (d) Potassium deposition dependence of the metallic states and IGSs, respectively. (e) Potassium deposition dependence of Ti 3p, O2s, and K 3p core levels, and the differential spectra between those observed after (K #1-#8) and before (K #0) potassium deposition. (f) Potassium-deposition dependence of the spectral intensities of the gap states (black line), IGSs (blue line), and metallic states (red line).

The spectral change in the gap states upon depositing potassium was investigated. Nine PES spectra in the gap states upon depositing potassium of a-TiO$_2$, which are numbered K #0 to K #8, were successively taken. As shown in Figure 1(e), the spectral intensity of the Ti^{4+} 3p core level monotonically reduces with the deposition of potassium, whereas that of the Ti^{3+} 3p core level gradually increases. A successive reduction in the spectral intensity of the O 2s core levels is also shown, but this is considerably smaller compared with the spectral enhancement observed in the K 3p core levels. Since oxygen vacancies were hardly formed near the surface by irradiating the SR, the observed slight reduction in the spectral intensity of the O2s core level is considered to be caused by the deposition of potassium on the surface. On the contrary, the clear changes in the Ti 3p core level (Figure 1(e)) and in the gap states (Figure 1 (b)) are considered to be attributable to the potassium deposition. The gap states were deconvoluted into metallic states and in-gap states (IGSs). Figures 1(c) and 1(d) show the spectral contributions of the metallic states and IGSs, respectively. Since the
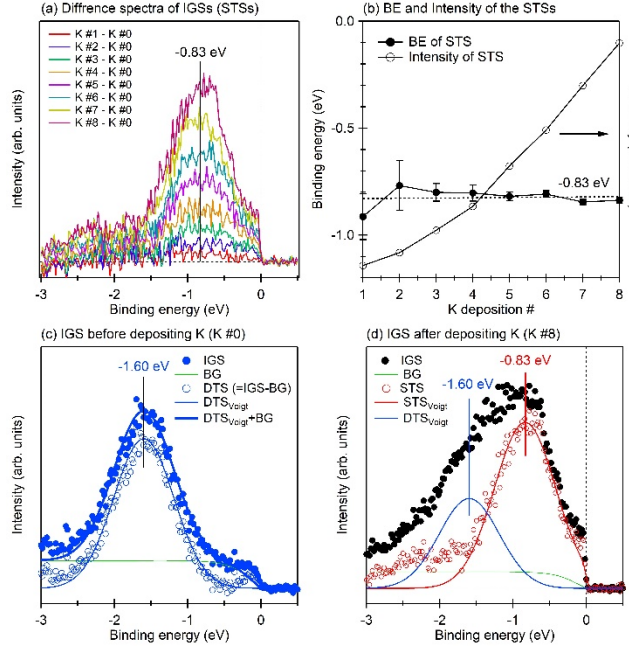
spectra were taken at low temperatures, the clear dip structures of the metallic state, caused by electron-phonon coupling, could be shown. The spectral width of the metallic states gradually increased with increasing spectral intensity. The spectrum of the IGS just after cleaving (K #0) is almost symmetric around the binding energy of -1.60 eV, but that after deposition (K #8), it shows an asymmetric shape, consisting of a peak centered at about -1 eV and a tail structure on its high binding energy side. The changes in the integrated spectral intensities of the gap states (black line), IGSs (blue line), and metallic states (red line) are summarized in Figure 1(f). From this figure, it is seen that the integrated intensities monotonically increase with the deposition of potassium.

As shown by the black line in Figure 1(c), the metallic state of the a-TiO$_2$ surface before potassium deposition shows a clear dip structure at the binding energy of about 0.1 eV. From recent PES studies of a-TiO$_2$ [2, 3], it is considered that the dip structure of the metallic state is derived from electron-phonon coupling, as discussed considerably for cuprates [4]. The energy position of the dip structure is almost consistent with the energy of a longitudinal optical (LO) E_u phonon mode in the ab-plane and/or of a LO A_{2u} phonon mode along the c axis. The dip structure of the metallic state gradually becomes obscure with increasing amount of deposited potassium. The metallic state of pristine a-TiO$_2$ before potassium deposition is formed by the original electron carriers in the bulk. After potassium deposition, on the other hand, the metallic state is derived from the electron carriers doped near the surface, in addition to the original bulk contribution. Recently, such electron-phonon coupling strengths for a-TiO$_2$ and SrTiO$_3$ surfaces were reported to strongly depend on the carrier density [3]. In addition, it was shown that the surface phonon energy of a-TiO$_2$ depends on the orientation, and is somewhat different from that of the bulk. Therefore, it is considered that the observed successive changes in the spectral shape of the dip structure in the metallic state were caused by the increase in the electron carriers at the surface by depositing potassium, and/or by the change in the surface phonon energy. For pristine a-TiO$_2$, just after cleaving, the finite spectral intensity in the vicinity of E_F in the IGSs is shown by the black line in Figure 1(d). Observing it in detail, the spectral intensity gradually increases from E_F, and the shape is somewhat different from a stepped-like feature characteristic of a Fermi-Dirac function. This spectral intensity near E_F appears almost uniformly across the entire measured momentum space. For rutile TiO$_2$, on the other hand, almost no spectral intensity was observed near E_F. These results suggest that the finite spectral intensity of the IGSs near E_F shown for pristine a-TiO$_2$ is closely related with the metallic state, i.e., it is a result of the secondary photoelectrons derived from the inelastic scattering of the metallic states. Now, we shall discuss the change in the spectral intensity of the IGSs near E_F caused by the deposition of potassium, shown in Figure 1(d). As the spectral intensity of the IGSs near E_F increases with the deposition of potassium, the background intensity around the binding energy of -3 eV also increases, but not so much compared with that of the IGSs. When potassium is heavily deposited (K #8), especially, it is important to note that the background intensity becomes smaller than that of the IGS near E_F. This suggests that the net increase in the spectral intensity of IGS near E_F due to potassium deposition is mainly caused by a phenomenon that is different from the inelastic scattering of the metallic state. As will be discussed later in detail, a dispersion-less state at - 0.83 eV is induced by potassium deposition. The state at -0.83 eV is close to E_F compared to the IGS derived from the oxygen vacancies in the bulk of the pristine a-TiO$_2$ before potassium deposition (-1.60 eV), and so, there is a finite spectral intensity near E_F. From another point of view, this suggests that the metallic state formed by potassium deposition is less subject to the inelastic scattering, and does not contribute much to the background. It is considered that the electrons produced upon the depositing potassium are doped near the surface, and that the state at -0.83 eV is confined to the vicinity of the surface [3]. Those surface contribution induced by potassium deposition should be hard to be accompanied by the background produced by the inelastic scattering.

Subsequently, we will discuss the origin of the IGS at -1.60 eV and the state at -0.83 eV shown for the potassium-deposited surface, which are extracted by subtracting the metallic contribution from the gap state. It is seen from Figure 2 (c) that the IGS of the pristine surface just after cleaving consists of a dispersive-less state located at the binding energy of -1.60 eV and the background. On the basis of the spectral width, the IGS has no spectral intensity near E_F, suggesting no contribution to electrical conduction. Previous soft-x-ray PES spectra of electron-doped SrTiO$_3$ also showed the dispersion-less state located near the midpoint of the band gap and discussed its origin in detail. In our previous PES studies on electron-doped SrTiO$_3$, it was shown that the spectral intensity of the gap state is closely related with the number of doped electrons, suggesting that the gap state is not derived from the oxygen vacancies at the surface caused by the cleaving process or the short SR irradiation before the first measurement. A similar IGS in the a-TiO$_2$ was observed in the vicinity of the center of the band gap from resonant inelastic X-ray scattering measurement, and was concluded to be attributed to the oxygen vacancies in the bulk. Therefore, it seems reasonable to consider
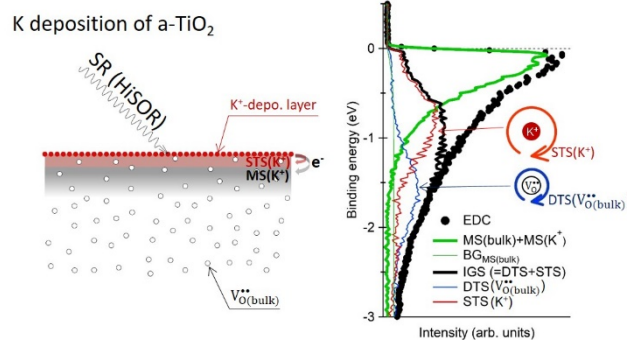
that the IGS located at -1.60 eV in our PES spectra also represents an intrinsic electronic structure derived from the oxygen vacancies in the bulk and is unique to naturally grown a-TiO$_2$. The IGS at -1.60 eV is considered to be a localized state, in which a fraction of the doped electrons are tightly trapped in the vicinity of the oxygen vacancies. Therefore, the IGS at -1.60 eV is hereafter referred to as a deep-trap state (DTS). Theoretical calculations also predicted such a DTS for the a-TiO$_2$ with oxygen vacancies in the bulk. Since the DTS has almost no spectral intensity around E_F, it is considered that the conductivity in the bulk is derived from the metallic state, while the DTS is closely related with the (electron) carrier generation efficiency, or the dopability of the doped electrons.

FIGURE 2. (a) Difference spectra for a-TiO$_2$ before and after potassium deposition. (b) Peak position and integrated intensity of the difference spectra. (c) IGS spectra before potassium deposition (blue solid circles). The Shirley background derived from the metallic state is denoted by the green line. An empirical DTS (blue open circles) was estimated by subtracting the background (BG) from the IGS. The DTS was fitted using the Voigt function with the Shirley background (DTSVoigt, blue thin line). The peak position of the DTS was estimated at -1.60 eV. (d) An example of the IGS spectra after potassium deposition. The empirical shallow-trap state (STS; red open circles) was estimated by subtracting the BG and DTSVoigt from the IGS. The STS could be well fitted with the Voigt function multiplied with a Fermi-Dirac function (red line). The peak position was estimated at -0.83 eV.

As shown in Figure 1 (d), the DTSs at -1.60 eV can still be observed as a shoulder structure even after potassium deposition. This suggests that the electrons generated upon potassium deposition are doped only close to the surface [3], and the bulk contribution observed in the PES spectra just after cleaving can also be observed after potassium deposition. In order to extract the essential contribution of potassium deposition, we subtracted the DTS before potassium deposition from the IGSs after potassium deposition. From the difference spectra in Figure 3(a), it is clearly seen that another state gradually appears at -0.83 eV, which is almost constant regardless of the amount of deposited potassium. The state at -0.83 eV appears over a wide momentum area and shows no clear dispersion. Similar to the case of the DTS, a fraction of the electrons doped due to potassium deposition are trapped in the vicinity of the potassium ions, which produces another localized state near the surface. The peak position of the localized state (-0.83 eV) induced by potassium deposition is about half that of the DTS (-1.60 eV) induced by the oxygen vacancies. The difference in the peak position of the localized state is considered to be caused by that in the valence between the oxygen vacancies in the bulk (formally divalent) and the potassium ions at the surface (monovalent). The traps of the doped electrons in the vicinity of the monovalent potassium ions seem to be loose and incomplete, and so, the localized state at -0.83 eV induced by potassium deposition has a finite spectral intensity at E_F. This suggests that the surface conduction observed after potassium deposition is mainly caused by the metallic state, but is also partially attributed to the localized state at -0.83 eV. Hereafter, we refer to the localized state at -0.83 eV as a shallow-trap state (STS). In Figure 2 (d), an example of the IGS spectra after potassium deposition (black solid circles), together with the DTS (blue open circles) and STS (red open circles) contributions, is shown. The DTS could be easily fitted by the Voigt function (blue line) with the background

(black line). Similarly, the STS could be well reproduced by the Voigt function multiplied with a Fermi-Dirac function (red line). Interestingly, the spectral shape of the STS is almost the same as that of the DTS, as shown in Figure 2 (e), except for the finite spectral intensity of the STS.

FIGURE 3. Schematic view of the gap state of a-TiO$_2$ due to the electrons doped by potassium deposition.

Figure 3 presents a schematic view of the gap state due to the electrons doped near the surface by potassium deposition. Elucidating the microscopic relationship between the metallic surface state and the IGS on the surface will be crucial in understanding the macroscopic semiconducting properties such as the (electron) carrier generation efficiency and mobility. The enhancement in the metallic state as a result of potassium deposition can be interpreted as being simply caused by the doping of the electrons into the surface state called 2DEG/L. In addition to the metallic surface state, a fraction of the doped electrons are loosely trapped around the monovalent potassium ions (-0.83 eV), and are shown as a STS having a finite spectral intensity at E_F, which is considered to contribute partially to the surface conductivity. Since the oxygen vacancies in the bulk are formally divalent, on the other hand, it is supposed that the electrons around these vacancies are more tightly trapped (-1.60 eV). As a result, the DTS reveals no spectral intensity at E_F, suggesting no contribution to the bulk conductivity. The oxygen vacancies in the bulk cause a direct disorder in the conduction pathway, and so, the intensity of the metallic state relative to the DTS, or the (electron) carrier generation efficiency, is considered to decrease with increasing oxygen vacancies. On the other hand, the potassium ions on the surface do not directly disturb the (electron) carrier motion in the conduction pathway, the ratio of the spectral intensities of the metallic state and the STS is hardly affected by the amount of deposited potassium. It seems that the (electron) carriers at the surface are effectively generated by potassium deposition and the efficiency is hardly sensitive to the amount of deposited potassium.

In conclusion, we doped electrons near a-TiO$_2$ surface by potassium deposition. Electrons are supplied by the potassium ions outside the conduction pathway. Since there are formally no oxygen and tin vacancies in the conduction pathway, the motion of the doped electrons is supposed to be only *weakly* and *indirectly* influenced by the potassium ions. The electrons doped by potassium deposition mainly function as the carriers responsible for the surface conductivity, and the few remaining are trapped around the deposited potassium ions. Since the trap is loose and incomplete, the STS induced by the trapped electrons around the monovalent potassium ions has a finite DOS at E_F. That is, there are two kinds of (electron) carrier sources: the metallic state and the STS induced by potassium deposition. Minohara et al. showed that electrons can be doped onto a-TiO2 by a heterointerface between a-TiO$_2$ and the LaO-terminated polar surface of LaAlO$_3$ (001). [7] On the basis of the reported sheet carrier density, most of the electrons generated at the interface are considered to behave as electron carriers. In addition, the mobility observed empirically is high (25 cm^{2}V^{-1}s^{-1} at room temperature), compared with that of the impurity/vacancy-doped a-TiO$_2$ reported previously. Although such semiconducting properties are thought to be originated from electron carriers doped into ideal conduction pathway without the disturbance, it is hard to explain the temperature dependence of the resistivity merely based on the metallic state. Like the potassium-deposited a-TiO$_2$ surface shown here, a fraction of the electrons doped onto the interface are considered to be weakly and indirectly trapped/scattered by the lanthanum/oxygen ions outside the conduction pathway. As a result, it is expected that weakly and indirectly trapped/scattered electrons also partially contribute to the interface conductivity, along with the coherent electrons.

REFERENCES

1. A. Fujishima, X. Zhang, D. A. Tryk, *Surf. Sci. Rep.* **63**, 515-582 (2008)

2. T. C. Rödel, F. Fortuna, F. Bertran, M. Gabay, M. J. Rozenberg, A. F. Santander-Syro, P. Le Fèvre, *Phys. Rev. B* **92**, 041106(R) (2015)..

3. R. Yukawa, M. Minohara, D. Shiga, M. Kitamura, T. Mitsuhashi, M. Kobayashi, K. Horiba, H. Kumigashira, *Phys. Rev. B* **97**, 165428 (2018).

4. H. Eisaki, N. Kaneko, D. L. Feng, A. Damascelli, P. K. Mang, K. M. Shen, Z.-X. Shen, M. Greven, *Phys. Rev. B* **69**, 064512 (2004).

5. R. Asahi, Y. Taga, W. Mannstadt, A. J. Freeman, *Phys. Rev. B* **61**, 7459-7465 (2000).

6. H. Iwasawa, K. Shimada, E. F. Schwier, M. Zheng, Y. Kojima, H. Hayashi, J. Jiang, M. Higashiguchi, Y. Aiura, H. Namatamea, M. Taniguchia, *J. Synchrotron Rad.* **24**, 836–841 (2017).

7. M. Minohara, T. Tachikawa, Y. Nakanishi, Y. Hikita, L. F. Kourkoutis, J.-S. Lee, C.-C. Kao, M. Yoshita, H. Akiyama, C. Bell, H. Y. Hwang, *Nano Lett.* **14**, 6743−6746 (2014).

Angle-resolved Photoelectron Spectroscopy Study of Ce1-2-10 systems III

H. Yamaoka[a], E. F. Schwier[b], Y. Yamamoto[c], K. Ohno[d],
T. Nishioka[d], K. Shimada[b], and J. Mizuki[c],

[a]*RIKEN SPring-8 Center, Sayo, Hyogo 679-5148, Japan*
[c]*Hiroshima Synchrotron Radiation Center, Hiroshima University, Higashi-Hiroshima, Hiroshima 739-0046, Japan*
[b]*Graduate School of Science and Technology, Kwansei Gakuin University, Sanda, Hyogo 669-1337, Japan*
[d]*Graduate School of Science, Kochi University, 2-5-1 Akebono, Kochi 780-8520, Japan*

Keywords: electronic structure, photoelectron spectroscopy, Ce1-2-10, DFT calculations, hybridization

Ternary intermetallic compounds of CeM_2Al_{10} (M = Ru, Os, Fe) have attracted many interests because of their unusual physical properties [1,2]. An anomaly in CeT_2Al_{10} was observed due to its anisotropic magnetic order. Paramagnetic susceptibility exhibits large anisotropy in CeM_2Al_{10}, $\chi_a > \chi_c > \chi_b$ at $T > T_0$, where χ_i is the susceptibility along i-axis and T_0 being the transition temperature to the antiferromagnetic (AFM) state. However, at $T < T_0$ the AFM order occurs along the c-axis, not along the easy a-axis. Kondo *et al.* suggested that a larger $c-f$ hybridization along the a-axis could flip the magnetization easy axis towards the c-axis [3]. Thus, the anomalies in CeT_2Al_{10} may correlate to an anisotropy of the hybridization strength. In CeM_2Al_{10} a detailed study of the complex electronic structure, especially direct evidence of the anisotropy of the hybridization strength, has not been performed yet. By substituting Ru with Rh in $Ce(Ru_{1-x}Rh_x)_2Al_{10}$ (x~0.03-0.05) the axis of magnetization is flipped from c-axis to a-axis   and the magnetic moment increases to $0.8\mu_B$/Ce. This makes the Rh substitution an ideal method to study the $c-f$ hybridization anisotropy.

We performed XRD study for $Ce(Ru_{1-x}Rh_x)_2Al_{10}$, indicating no structural change. We measure x-ray absorption spectra at Ce L_3 edge with partial fluorescence mode (PFY-XAS), corresponding to the high-resolution absorption spectra [4]. The c-f hybridization effect appears as increase of f^0 intensity and decrease of f^1 intensity in the PFY-XAS spectra, resulting increase of the Ce valence with the Rh substitution to Ru site. This may suggest a possible Lifshitz transition. We reported previously that the ARPES at the $4d$–$4f$ resonance showed the anisotropy of the hybridization strength directly and the anisotropy changed drastically with a small amount of Rh-doping to the Ru site in $CeRu_2Al_{10}$. Here, we newly report the ARPES result for $CeFe_2Al_{10}$. Figure 1(a) shows the ARPES results of $CeFe_2Al_{10}$ at $h\nu$ = 115 eV. The angle-integrated spectra are shown in Fig. 1(b) for $CeRu_2Al_{10}$ and Fig. 1(c) for $CeFe_2Al_{10}$. Note that the intensity ratio of $4f^1$ near the Fermi level to $4f^0$ around 2.5 eV is a measure of the c-f hybridization strength. In $CeRu_2Al_{10}$ strong anisotropy of the hybridization strength is observed and the hybridization along the a-axis is much stronger compared to that along the c-axis. While the anisotropy of the hybridization strength was weakened in $CeFe_2Al_{10}$ as shown in Fig. 1(c).

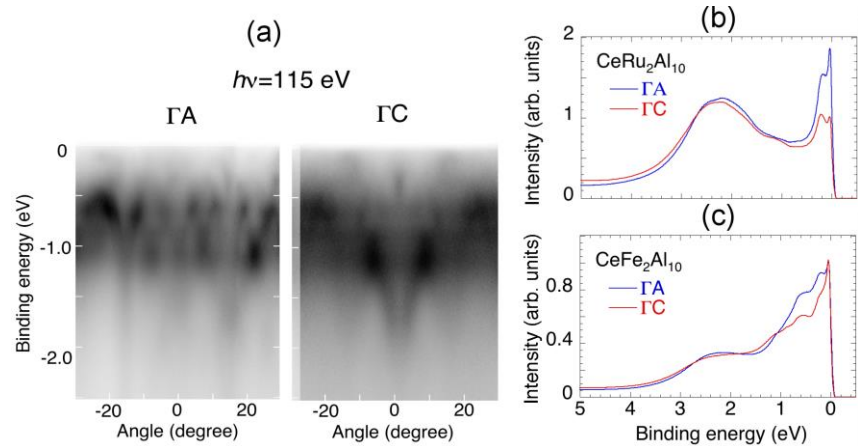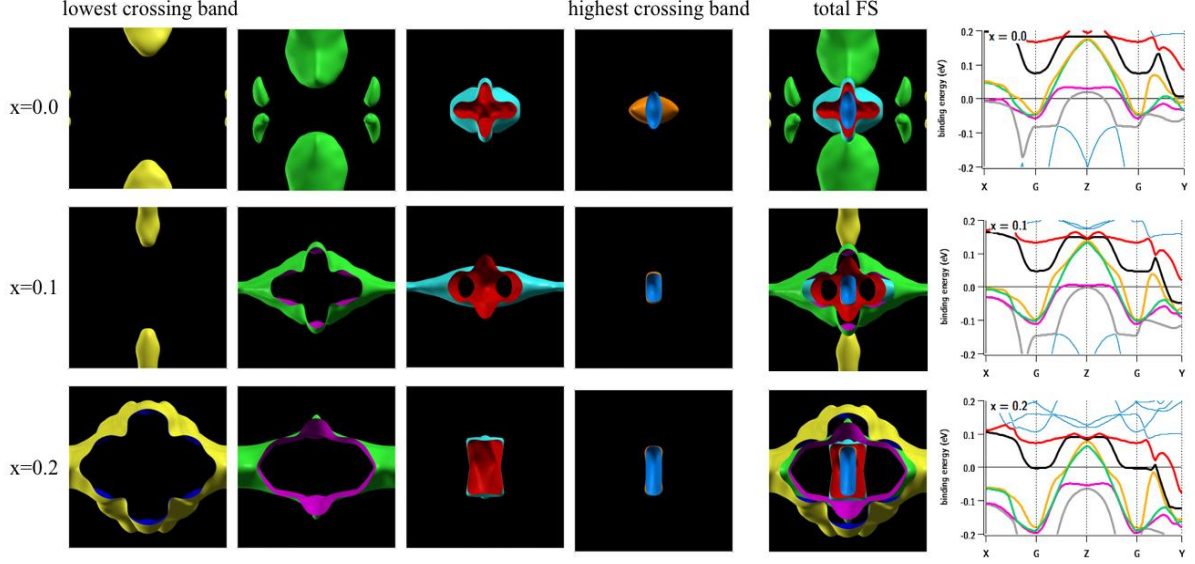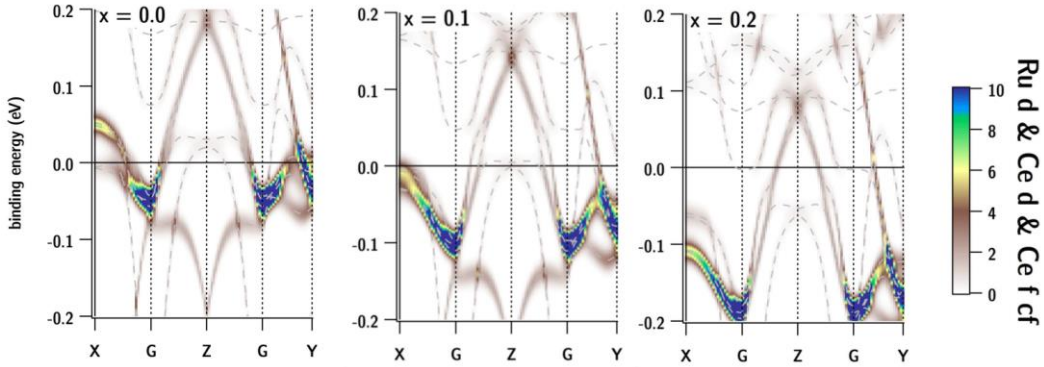We also performed DFT calculations for $CeRu_2Al_{10}$. The results are shown in Fig. 2. Electron doping the unit-

FIGURE 1. (a) ARPES results of $CeFe_2Al_{10}$ at $h\nu$ = 115 eV. (b) Angle-integrated spectra of $CeRu_2Al_{10}$. (c) Angle-integrated spectra of $CeFe_2Al_{10}$.

cell leads to (in first-order) a rigid-type band shift. This has significant influence on the Fermi Surface (see Fig. 2), but more importantly on the *c-f* hybridization at the Fermi level. For the undoped case the *c-f* hybridization is strongest along GY followed by GX. Upon electron doping the *c-f* band along GY becomes fully occupied and the GX direction dominates the *c-f* hybridization at the Fermi level (see Fig. 3).

FIGURE 2. The results of the DFT calculations with the Fermi surfaces of XZ plane (right figures) for Ce(Ru$_{1-x}$Rh$_x$)$_2$Al$_{10}$.

FIGURE 3. The results of the DFT calculations: Rh-doping dependence of the *c-f* hybridization for Ce(Ru$_{1-x}$Rh$_x$)$_2$Al$_{10}$.

REFERENCES

1. V. M. T. Thiede, T. Ebel, and W. Jeitschko, *J. Mater. Chem.* **8**, 125 (1998).
2. T. Nishioka, Y. Kawamura, T. Takesaka, R. Kobayashi, H. Kato, M. Matsumura, K. Kodama, K. Matsubayashi, and Y. Uwatoko, *J. Phys. Soc. Jpn.* **78**, 123705 (2009).
3. A. Kondo, J. Wang, K. Kindo, Y. Oogane, Y. Kawamura, S. Tanimoto, T. Nishioka, D. Tanaka, H. Tanida, and M. Sera, *Phys. Rev. B* **83**, 180415 (2011).
4. Y. Zekko, Y. Yamamoto, H. Yamaoka, F. Tajima, T. Nishioka, F. Strigari, A. Severing, J.-F. Lin, N. Hiraoka, H. Ishii, K.-D. Tsuei, and J. Mizuki, *Phys. Rev. B* **89**, 125108 (2014).
5. *elk* version 4.0.16 (http://elk.sourceforge.net)

Electronic structure of $Pr_{1-x}Y_xCoO_3$ in comparison with copper delafossites studied by resonant photoemission spectroscopy

D. Kanai[a], R. Takayanagi[a], K. Takahashi[a], M. Okawa[a],
Y. Kobayashi[b], and T. Saitoh[a]

[a]*Department of Applied Physics, Tokyo University of Science, Katsushika, Tokyo 125-8585, Japan*
[b]*Department of Physics, Tokyo Medical University, Shinjuku, Tokyo 160-8402, Japan*

Perovskite-type cobaltites $RECoO_3$ (RE: rare earths or Y) typically show a broad and strange magnetic/electronic transition(s) with temperature [1-4], which has long been a major research interest on the properties of $RECoO_3$. So far, it has been established that the phenomenon essentially originates from unusual spin-state evolution in the Co $3d$ electrons although it has not been completely understood. By contrast, it has long been considered that the RE site acts merely as a charge reservoir and plays no important role in the magnetism and the electronic structure of $RECoO_3$, even in the case of Ce, Pr, Nd, etc., which have magnetic $4f$ electrons. Considering the localized nature of the $4f$ electrons, it is reasonable to assume that they are independent of the Co $3d$ electrons.

Recently, however, Kobayashi *et al*. found that the magnetism of $Pr_{1-x}Y_xCoO_3$ can't be explained by such a simple picture; $Pr_{1-x}Y_xCoO_3$ shows temperature dependent Van Vleck paramagnetism for the smaller Y content ($x \leq 0.4$) while it shows a Curie-Weiss-like behavior for the lager content ($0.5 \leq x \leq 0.9$) [5]. Because the effective moment deduced from the Curie-Weiss term was able to be explained by the $4f^1$ electron configuration, they speculated that the Pr $4f$ electron of Pr^{3+} ($4f^2$) was partly transferred to the Co $3d$ state due to the hybridization between Pr $4f$ and Co $3d$ via O $2p$ states in the diluted Pr (namely, large x) range.

In this work, we performed Pr $4d$-$4f$ resonant photoemission spectroscopy (RPES) measurements on $Pr_{1-x}Y_xCoO_3$ ($x=0.5$ and 0.8) in order to examine the validity of this "Pr $4f$−O $2p$−Co $3d$ hybridization model".

Polycrystalline samples of $Pr_{1-x}Y_xCoO_3$ ($x=0.5$ and 0.8) were prepared by the sol-gel method [5]. RPES experiments were performed at the beamline BL-1 of the Hiroshima Synchrotron Radiation Center (HiSOR) using a Scienta R4000 electron analyzer. The total energy resolution was 90-200 meV at 110-150 eV photon energy range. Clean and fresh surface was prepared by fracturing the samples *in situ* right before the measurements.

Figure 1(a) shows RPES spectra of $Pr_{0.5}Y_{0.5}CoO_3$ in the Pr $4d$-$4f$ resonance region ($h\nu$=110eV-150eV). The on- (123 eV) and off- (120 eV) resonance energies, highlighted by thick lines, were determined from the constant-initial-state (CIS) spectra deduced from the RPES intensity shown in Panel (a) (not shown for $x=0.8$). The valence band continues from ~0.5 eV to about 8 eV and one can see the leading peak at 1 eV characteristic of the Co^{3+} oxides with the low-spin state [6,9].

Figure 1(b) shows the on-off difference spectra of $Pr_{1-x}Y_xCoO_3$ ($x=0.5$, 0.8) together with the on- and off-resonant spectra. The difference spectra experimentally represent the Pr $4f$ partial density of states (PDOS). It is noted that the experimental Pr $4f$ PDOS of this system (including $PrCoO_3$ ($x=0$) [9]) has a double-peak (α and β) structure whereas that of $PrMO_3$ (M = Mn or Ni) shows a single peak [7,8]. This fact indicates that the combination of Pr^{3+} and Co^{3+} is rather exceptional but it is similar to $Y_{0.2}Pr_{0.8}Ba_2Cu_3O_{7-y}$ [10]. In order to understand the double-peak structure, Saitoh *et al*. proposed a Pr $4f$−O $2p$ hybridization model based on the Fehrenbacher-Rice model for PBCO [9,11]. They also inferred that this exceptional situation would originate from a large Pr $4f$−O $2p$−Co $3d$ effective hybridization due to the large Co $3d$ DOS at the binding energy of ~1eV [9]. According to their interpretation, α and β are mainly due to $|4f^0 L\rangle$ and $|4f^1\rangle$ final state, and hence roughly correspond to $4f^1$ and $4f^2$ initial state electron configuration, respectively. (Here, L denotes a ligand state.) In Panel (b), one can observe that the intensity ratio and relative location of α and β
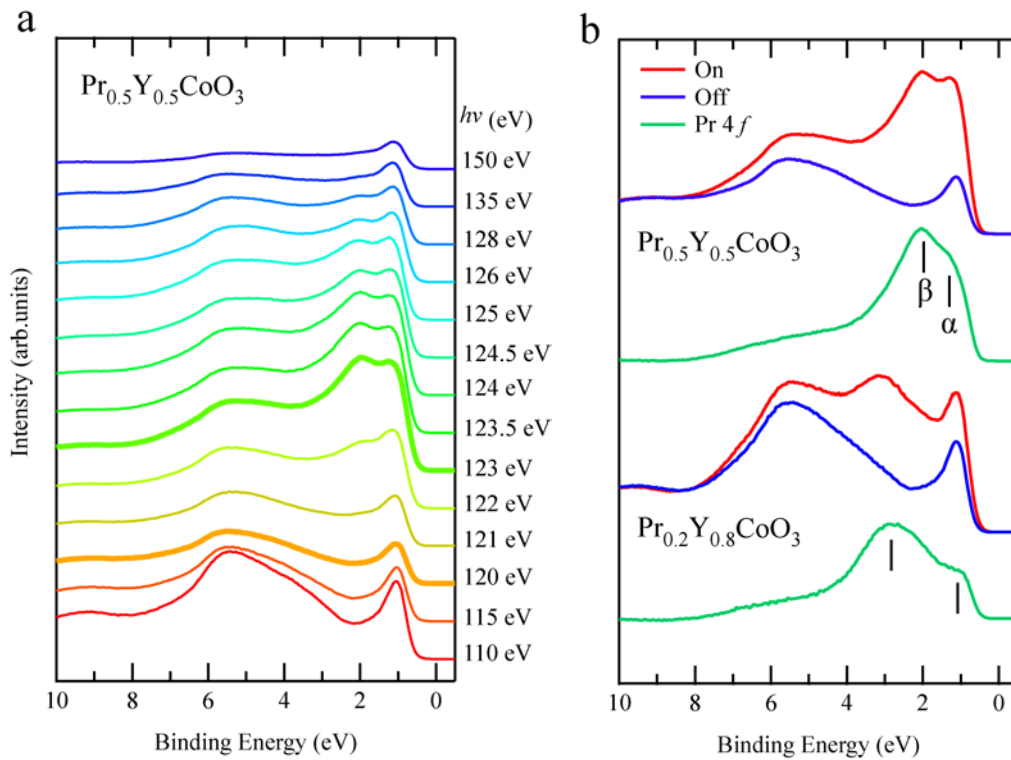
change with x. In fact, α grows compared to β with increasing x, which is consistent with the evolution of the magnetic property with x. Hence this change is possibly interpreted as an increase in the strength of the Pr $4f$−O $2p$−Co $3d$ effective hybridization with x, although a further study should be needed.

Finally, we point out similarities between the electronic structure of $Pr_{1-x}Y_xCoO_3$ and a copper delafossite $CuCrO_2$. Yokobori $et\ al$. have proposed a Cu $3d$−O $2p$−Cr $3d$ charge transfer model in order to explain the Cu^{2+} signal in the photoemission spectra of Cu^+CrO_2 [12], which is similar to the present case, the Pr^{4+} signature in the magnetic measurements in $Pr^{3+}CoO_3$. Here Cu $3d$ and Cr $3d$ corresponds to Pr $4f$ and Co $3d$. The two completely different systems thus realize each unusual valence state due to an unexpected but similar effective hybridization mechanism.

REFERENCES

1. G. Thornton, F. C. Morrison, S. Partington, B. C. Tofield, and D. E. Williams, J. Phys. C **21**, 2871 (1988).
2. M. Itoh, M. Mori, S. Yamaguchi, and Y. Tokura, Physica B **259-261**, 902 (1999).
3. M. Itoh, J. Hashimoto, S. Yamaguchi, and Y. Tokura, Physica B **281-282**, 510 (2000).
4. S. Yamaguchi, Y. Okimoto, and Y. Tokuram, Phys. Rev. B **54**, R11022 (1996).
5. Y. Kobayashi, Y. Terakado, and K. Asai, J.Phys. Soc. Jpn. **83**, 104704 (2014).
6. T. Saitoh, T. Mizokawa, A. Fujimori, M. Abbate, Y. Takeda, and M. Takano, Phys. Rev. B **55**, 4257 (1997).
7. J.-S. Kang, C. G. Olson, J. H. Jung, S. T. Lee, T. W. Noh, and B. I. Min, Phys. Rev. B **60**, 13257 (1999).
8. E. Sakai, K. Yoshimatsu, K. Tamamitsu, K. Horiba, A. Fujimori, M. Oshima, and H. Kumigashira, Appl. Phys. Lett. **104**, 171609 (2014).
9. T. Saitoh, D. Ishii, A. Hachimura, M. Hirose, T. S. Naing, Y. Kobayashi, K. Asai, M. Nakatake, M. Higashiguchi, K. Shimada, H. Namatamec, and M. Taniguchi, J. Magn. Magn. Mater. **310**, 981 (2007).
10. J.-S. Kang, S. Haffner, C. G. Olson, J. H. Kim, M. B. Maple, S. K. Kwon, and B. I. Min, Phys. Rev. B **66**, 052503 (2002).
11. R. Feherenbacher and T. M. Rice, Phys. Rev. Lett. **70**, 3471 (1997).
12. T. Yokobori, M. Okawa, K. Konishi, R. Takei, K. Katayama, S. Oozono, T. Shinmura, T. Okuda, H. Wadati, E. Sakai, K. Ono, H. Kumigashira, M. Oshima, T. Sugiyama, E. Ikenaga, N. Hamada, and T. Saitoh, Phys. Rev. B **87**, 195124 (2013).

FIGURE 1. Resonant photoemission spectra of $Pr_{0.5}Y_{0.5}CoO_3$ and $Pr_{0.2}Y_{0.8}CoO_3$ taken at 300K. (a) resonant photoemission spectra of $Pr_{0.5}Y_{0.5}CoO_3$. The on- and off- resonant spectra are shown by thick lines; (b) difference spectra of $Pr_{0.5}Y_{0.5}CoO_3$ and $Pr_{0.2}Y_{0.8}CoO_3$ deduced from the on- and off-resonant spectra.

High Resolution Probing of the Energy Levels in Carbon Nanotubes

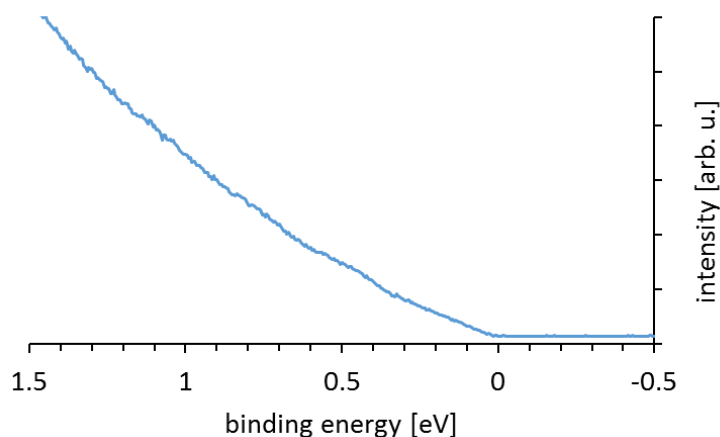Gunther Andersson[a], Cameron Shearer[a], Joe Shapter[a]

[a] Flinders Centre for Nanoscale Science and Technology, School of Chemistry and Physical Sciences, Flinders University of South Australia, Bedford Park, SA 5042, Australia

Keywords: carbon nanotubes, valence electron structure.

Single walled carbon nanotubes (SWCNTs) are a remarkable material that can be metallic or semiconducting depending upon the arrangement of carbon atoms in the cylinder, defined by chirality. [1] It is now possible to prepare samples with defined chirality via multi-step purification of an initially mixed ensemble. [1] The density of states (DOS) of the SWCNTs depend on their chirality and can range from metallic to semiconducting. The DOS determine how the SWCNTs can be used in electronic devices like solar cells.

The purpose of the visit at the beamline B1 in December 2017 was measuring the density of states of single wall carbon nanotubes. The measurements require low excitation energies in the range of a few 10 eV with high intensity. These conditions are provided at BL-1 at HiSOR.

Semiconducting SWCNTs with a large range of chiralities have been measured at BL-1. In Figure 1, a spectrum of P2 SWCNTs are shown measured at an excitation energy of 30 eV and a pass energy of the analyser of 20 eV. A range of further samples have been measured. We are currently drafting a manuscript for publication.

FIGURE 1 Valence electron spectrum of P2 SWCNTs measured at an excitation energy of 30 eV.

REFERENCES

1. B. Liu, F. Wu, H. Gui, M. Zheng and C. Zhou, *ACS Nano*, 2017, 11, pp. 31.

ARPES study of multi-band Bi chalcogenides

T. Mizokawa[a], Y. Matsuzawa[a], T. Morita[a], N. L. Saini[b],
T. Asano[c], T. Nakajima[c], R. Higashinaka[c], T. D. Matsuda[c], Y. Aoki[c],
E. F. Schwier[d], K. Shimada[d], H. Namatame[d]

[a] *Department of Applied Physics, Waseda University, Shinjuku-ku, Tokyo 169-8555, Japan*
[b] *Department of Physics, University of Roma "La Sapienza", Piazzale Aldo Moro 2, 00185 Roma, Italy*
[c] *Department of Physics, Tokyo Metropolitan University, Hachioji 192-0397, Japan*
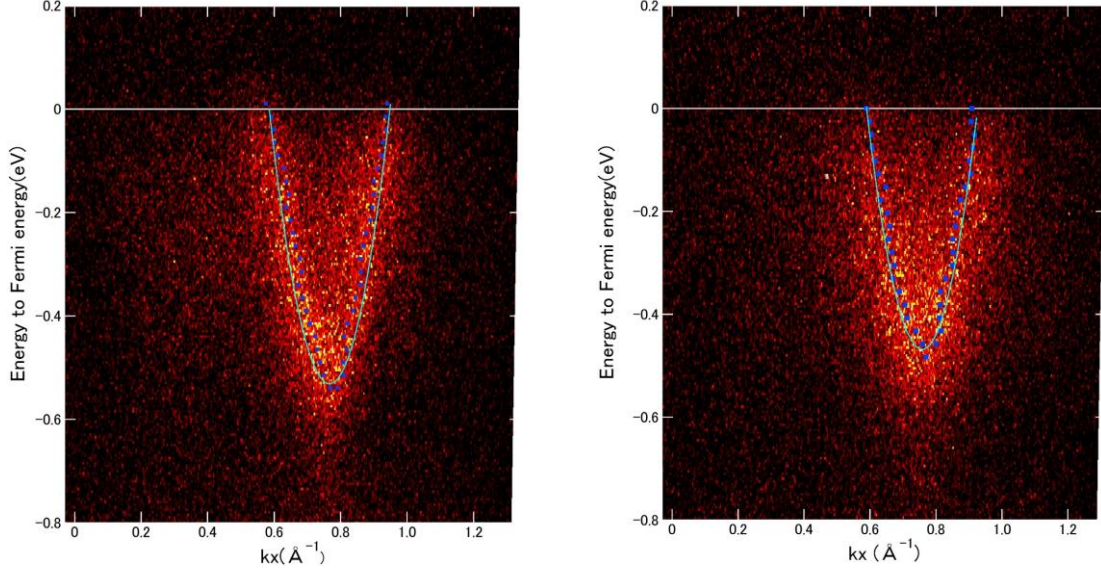[d] *HiSOR, Hiroshima University, Higashihiroshima, Hiroshima 739-0046, Japan*

The discovery of a BiS_2-based superconductor by Mizuguchi et al. [1] has been followed by extensive experimental and theoretical studies on the BiS_2-based superconductors including $RE(O,F)BiS_2$ systems (RE=rare earth element) [2-7]. In a typical $RE(O,F)BiS_2$ system, the F substitution for O in the RE(O,F) layer introduces electrons to the electronically active BiS_2 layer. The theoretical calculations indicate that the Fermi surfaces are constructed from the Bi $6p_x$ and Bi $6p_y$ orbitals [2]. The orbital character of the Fermi surfaces has been investigated by means of angle-resolved photoemission spectroscopy (ARPES) in $Ce(O,F)BiS_2$, and the ARPES results are consistent with the theoretical predictions [8]. In $Ce(O,F)BiS_2$, the Ce^{3+}/Ce^{4+} valence fluctuation is suppressed by the F doping and the decrease of the Pr valence tends to reduce the number of electrons in the BiS_2 layer. In order to understand the effect of the rare earth site in the BiS_2-based superconductors, we have performed angle-resolved photoemission spectroscopy on $Pr(O,F)BiS_2$ at BL-1, HiSOR. We cleaved the single crystalline samples in situ under ultrahigh vacuum in order to obtain clean (001) surface. The total energy resolution including both monochromator and electron energy analyzer was set to 21 meV. All the measurements were taken at 30 K.

Figure 1 shows the ARPES data across the electron pocket around the X point for x=0.3 and x=0.5 of $PrO_{1-x}F_xBiS_2$. Here, k_x is the wave number along the ΓX direction. In going from x=0.3 to 0.5, the bottom of the electron band is shifted towards the Fermi level, inconsistent with electron doping by the F substitution for O. Although the F doping is expected to introduce electrons in the BiS_2 layer, the Pr valence may decrease by the F doping just like $Ce(O,F)BiS_2$ and the doped electron can be compensated. Indeed, the Pr^{3+}/Pr^{4+} valence fluctuation is seen in core level spectra and the Pr^{4+} component is reduced with the F doping.

As for the Fermi surfaces, rectangular Fermi pockets around X point are clearly observed at x=0.5 and their area is much smaller than the value expected from the F doping level. The missing electrons can be accommodated by the Bi $6p_z$ orbitals with strong mixture of Pr 4f. In this scenario, the change of orbital anisotropy of Bi 6p (from $6p_x/6p_y$ to $6p_z$) is coupled with the Pr valence change (from Pr^{4+} to Pr^{3+}). Interestingly, some straight portions of the Fermi pockets disappear at x=0.3 although the area of the Fermi pockets would be consistent with the F doping level. The partial deletion of the Fermi surfaces suggests that charge-orbital fluctuations are stronger in the low doping level. In addition, the spectral shape near the Fermi level indicates strong electron-lattice coupling.

The present ARPES results show that $Pr(O,F)BiS_2$ exhibits interesting interplay between the Bi 6p orbital degeneracy and the Pr valence fluctuation. The strong electron-lattice coupling associated with the Bi 6p orbital degeneracy may play important roles in the emergence of the superconductivity.

FIGURE 1. Band dispersion along the ΓX direction taken at 30 K for x=0.3 (left panel) and x=0.5 (right panel).

REFERENCES

1. Y. Mizuguchi, H. Fujihisa, Y. Gotoh, K. Suzuki, H. Usui, K. Kuroki, S. Demura, Y. Takano, H. Izawa, and O. Miura, Phys. Rev. B **86**, 220510(R) (2012).
2. H. Usui, K. Suzuki, and K. Kuroki, Phys. Rev. B **86**, 220501(R) (2012).
3. S. Demura, Y. Mizuguchi, K. Deguchi, H. Okazaki, H. Hara, T. Watanabe, S. J. Denholme, M. Fujioka, T. Ozaki, H. Fujihisa, Y. Gotoh, O. Miura, T. Yamaguchi, H. Takeya, and Y. Takano, J. Phys. Soc. Jpn. **82**, 033708 (2013).
4. T. Sugimoto, B. Joseph, E. Paris, A. Iadecola, T. Mizokawa, S. Demura, Y. Mizuguchi, Y. Takano, and N. L. Saini, Phys. Rev. B **89**, 201117(R) (2014).
5. S. Demura, K. Deguchi, Y. Mizuguchi, K. Sato, R. Honjyo, A. Yamashita, T. Yamaki, H. Hara, T. Watanabe, J. Denholme, M. Fujioka, H. Okazaki, T. Ozaki, O. Miura, T. Yamaguchi, H. Takeya, and Y. Takano, J. Phys. Soc. Jpn. **84**, 024709 (2015).
6. T. Machida, Y. Fujisawa, M. Nagao, S. Demura, K. Deguchi, Y. Mizuguchi, Y. Takano, and H. Sakata, J. Phys. Soc. Jpn. **83**, 113701 (2014).
7. Masanori Nagao, Akira Miura, Satoshi Demura, Keita Deguchi, Satoshi Watauchi, Takahiro Takei, Yoshihiko Takano, Nobuhiro Kumada, Isao Tanaka, Solid State Commun. **178**, 33 (2014).
8. T. Sugimoto, D. Ootsuki, C. Morice, E. Artacho, S. S. Saxena, E. F. Schwier, M. Zheng, Y. Kojima, H. Iwasawa, K. Shimada, M. Arita, H. Namatame, M. Taniguchi, M. Takahashi, N. L. Saini, T. Asano, R. Higashinaka, T. D. Matsuda, Y. Aoki, T. Mizokawa, Phys. Rev. B **92**, 041113 (2015).

Laser ARPES study on surface-doped black phosphorus
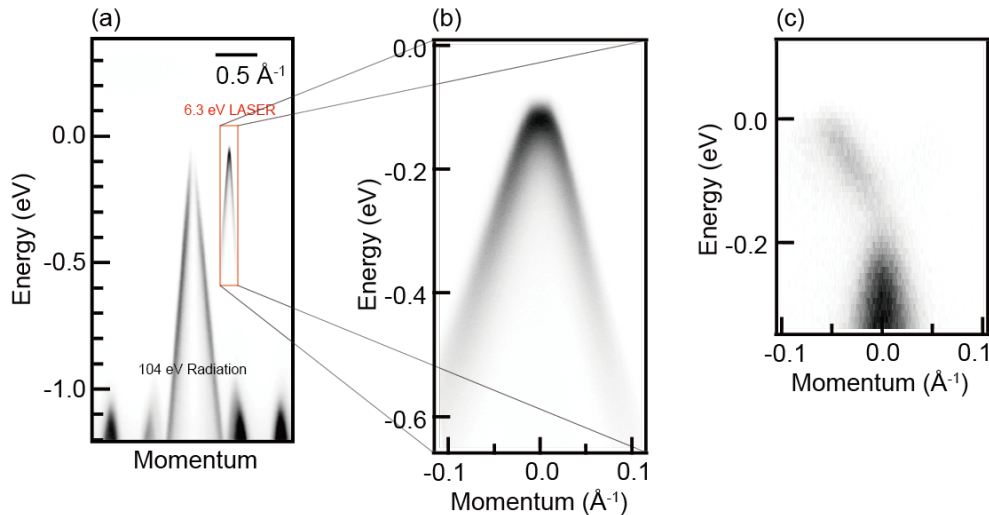
Woo Jong Shin[a, b] and Keun Su Kim[a]

[a]*Department of Physics, Yonsei University, Seoul 03722, Korea*
[b]*Department of Physics, Pohang University of Science and Technology, Pohang 37673, Korea*
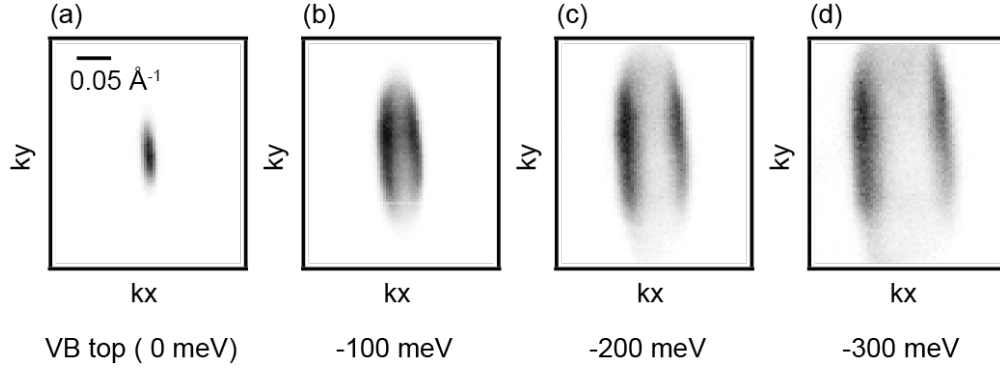
Keywords: black phosphorus, kink, angle-resolved photoemission spectroscopy

Two-dimensional (2D) van der Waals crystals, such as graphene, transition-metal dichalcogenide (TMD), and black phosphorus (BP), have been widely studied not only for their novel quantum phenomena, but also for their potential for application in nanoelectronics [1, 2]. Among them, BP is a narrow-gap semiconductor that shows a high charge carrier mobility together with high on-off current modulation ratio. Owing to this promising device characteristics, there is renewed interest in the study of few-layer BP and its applications [3]. BP is also attractive in that it has rather simple lattice and band structures for the study of fundamental quantum phenomena and manybody interactions. Recently, it was reported that BP decorated with alkali metal atoms exhibits an unexpected superconductivity with the critical temperature of 3.8 K [4]. This motivates us to study the possible strong electron-phonon interactions in alkali-metal doped black phosphorus.

Angle-resolved photoemission spectroscopy (ARPES) is a powerful technique, which can not only measure the band dispersion of quasiparticles, but also provide information on electron-phonon interactions. The latter is the effect of band renormalization that typically appears as an abrupt kink in the band dispersion at the energy of the involved phonons. By systematically analyzing the measured ARPES spectra, one can extract the electron-phonon self-energy that contains the strength of electron-phonon coupling. Consequently, electron-phonon coupling constant of surface-doped BP can possibly be quantified [5].

FIGURE 1. ARPES spectra taken from pristine BP along the armchair direction: (a) Data taken with the synchrotron radiation at the Advanced Light Source ($h\nu$ = 104 eV). (b) Data taken with the laser at HiSOR ($h\nu$ = 6.3 eV), which is also directly compared with that taken with the synchrotron radiation in (a). (c) Data taken after the deposition of K atoms on the surface of BP.

FIGURE 2. Series of constant-energy maps taken for the valence band of pristine BP at the energy shown at the bottom.

To address this issue, we employ high-resolution ARPES apparatus equipped with the Ti:sapphire laser at HiSOR. The ARPES spectral taken from pristine BP with laser-ARPES is shown in Fig. 1(b) and directly compared with that taken at the Advanced Light Source (ALS) with the synchrotron radiation [Fig. 1(a)]. The ARPES data taken with the laser show a much narrower spectral width than that with the synchrotron radiation, which indicates the improved energy and momentum resolutions owing to the low excitation energy of the LASER and its small spot size. After doping, however, the spectral feature gets broadened, diminishing the merit of high energy and momentum resolutions. This makes the expected kink feature not apparent in our data as shown in Fig. 1(c). Furthermore, ARPES spectra in Fig. 1(c) is strongly asymmetric with respect to the Gamma point, which is not expected at all for surface-doped BP. This could be due to a slight misalignment of the sample or the effect of light polarization. Indeed, the symmetry of constant-energy maps taken for the valence states of pristine BP is slightly tilted with respect to vertical and horizontal axes, as shown in Fig. 2. We expect that the possible use of a fully motorized 6-axis manipulator might improve this experimental situation for future studies.

REFERENCES

1. K.S. Novoselov *et al.*, *Science* **306**, 666-669 (2004).
2. K.S. Novoselov *et al.*, *PNAS* **102**, 10451-10453 (2005).
3. Xi Ling *et al.*, *PNAS* **112**, 4523-4530 (2015).
4. R. Zhang *et al.*, *Nat. Comm.* **8**, 15036 (2017).
5. A. V. Fedorov *et al.*, *Nat. Comm.* **5**, 3257 (2014).

Growth and ARPES Measurement of Hydrogenated Silicene on Ag(111)

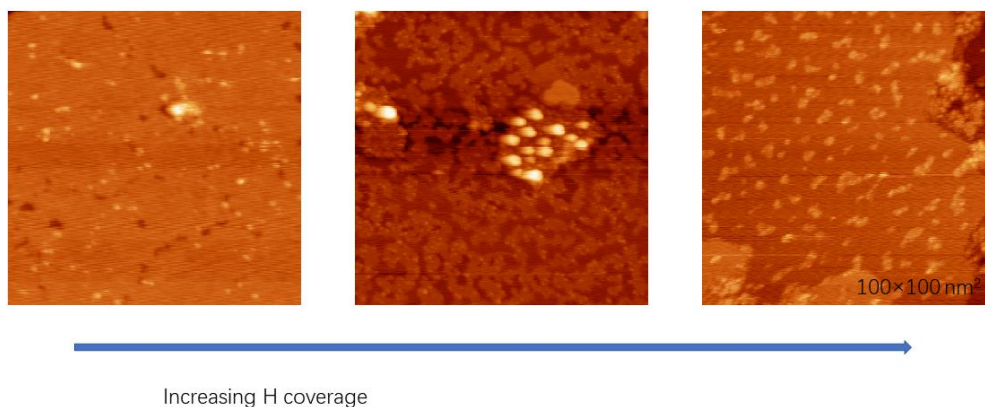Ya Feng[1,2], Baojie Feng[2],Shaolong He[1]and Kenya Shimada[2]

[1]*Ningbo Institute of Materials Technology and Engineering, Chinese Academy of Sciences, Ningbo, Zhejiang 315201, China*
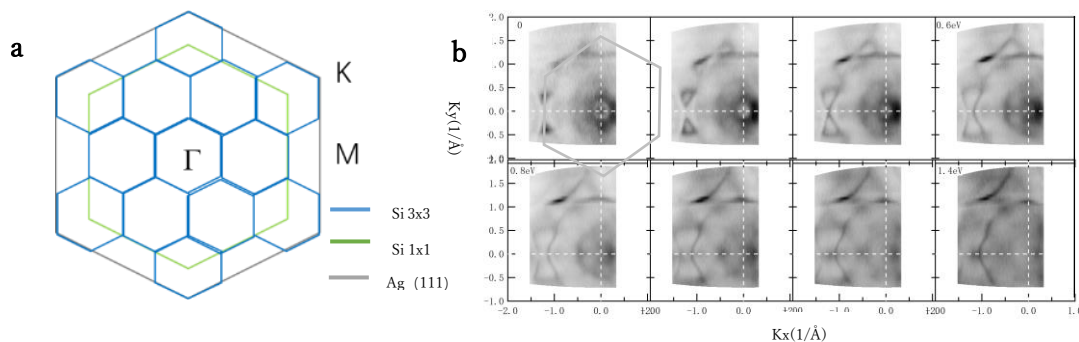[2]*Hiroshima Synchrotron Radiation Center, Hiroshima University, Higashi-Hiroshima, Hiroshima 739-0046, Japan*

Keywords: Silicene, magnetism , ARPES, Hydrogenation.

Silicene, analogous to graphene, is a one-atom-thick two-dimensional crystal of silicon, which is expected to share many of the remarkable properties of graphene [1-4]. For example, it harbors the characteristic low-energy Dirac cone states [5-9]. On the other hand, the buckled honeycomb structure of silicene, along with enhanced spin-orbit coupling, endows silicene with considerable advantages over graphene in that the spin-split states in silicene are tunable with external fields [10-14]. The unique advantages of silicene and its compatibility with the traditional silicon industry make it an attractive materials platform for next generation nanoelectronics applications.

Moreover, the theoretical calculations show that silicene will be magnetic after adsorption of hydrogen atoms and the Curie temperature can reach 300K [15]. Once combined with advanced nanotechnology based on silicon, the magnetic silicene possibly becomes a very promising nanotechnology application on spintronics. The long-range ferromagnetic ordering may simulate its application potential in spintronics.

Increasing H coverage

FIGURE 1. STM images with increasing Hydrogen atoms coverage.

FIGURE 2. Brillouin zone of silicene/Ag(111) and constant energy contours of pure silicene/Ag(111).

Last year we grew hydrogenated 3×3 silicene/Ag(111) on STM system and grew it again and did measurement on BL-1 in HiSOR. Figure 1 shows the STM images of hydrogenated silicene with different amount of hydrogenation. Although the hydrogenation is successful, more hydrogen atoms make less silicene on Ag(111).
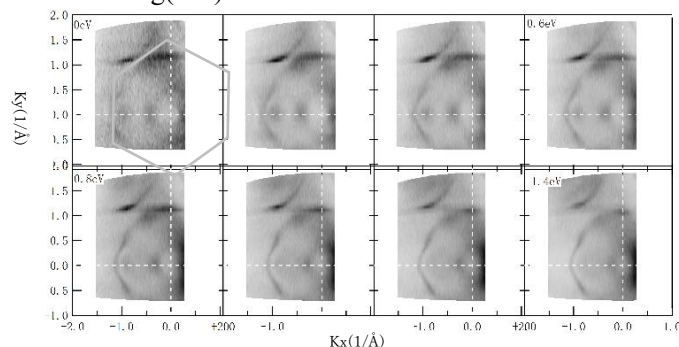

FIGURE 3. The constant energy contours of hydrogenated silicene.
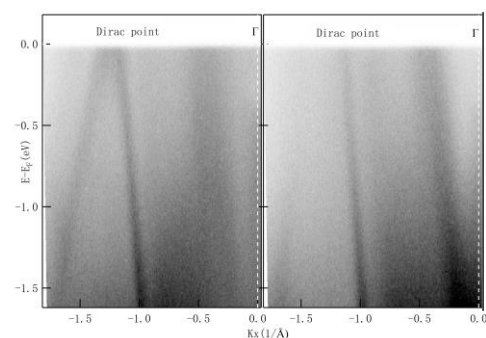
FIGURE 4. Compare of Dirac cone before and after hydrogenation.

According to the growth condition on STM system, we grew 3×3 silicene/Ag(111) and hydrogenated it in the prep-chamber and measured it by ARPES *in situ*. We got similar results as before[16] which showed twelve Dirac cone on the edge of Brillouin Zone of Ag(111). Figure 2.b shows the constant energy contours of pure silicene. There are twelve Dirac points on the Fermi surface, areas of which enlarge with higher binding energies. Figure 3 shows the constant energy contours of hydrogenated silicene. Figure 4 shows band structures along the momentum line acrossing the Dirac points before and after hydrogenation. The Dirac points are indeed corrsponding to linear dispersions. However, no matter from Fig.2 or Fig.3, we can not see obvious difference between the pure and the hydrogenated silicene but only weekness of the Dirac bands of silicene after hydrogenation. This result is consistant with the phenomena observed by STM that more hydrogen atoms makes less silicene. Maybe we hydrogenated the silicene too much that it became more than half hydrogenation. Some hydrogen atoms insert between the silicene and Ag(111), which makes some silicene seperated from Ag(111). Next time, we should control the amount of hydrogen atoms more carefully to avoid more hydrogenation.

REFERENCES

1. Novoselov KS, et al. Electric field effect in atomically thin carbon films. Science 306:666–669 (2004).
2. Novoselov KS, et al. Two-dimensional gas of massless Dirac fermions in graphene. Nature 438:197–200 (2005).
3. Zhang Y, Tan YW, Stormer HL, Kim P. Experimental observation of the quantum Hall effect and Berry's phase in graphene. Nature 438:201–204 (2005)
4. Castro Neto AH, Guinea F, Peres NMR, Novoselov KS, Geim AK. The electronic properties of graphene. Rev Mod Phys 81:109–162 (2009).
5. Bansil A, Lin H, Das T. Colloquium: Topological band theory. Rev Mod Phys 88:021004 (2016).
6. Takeda K, Shiraishi K. Theoretical possibility of stage corrugation in Si and Ge analogs of graphite. Phys Rev B Condens Matter 50:14916–14922 (1994).
7. Guzman-Verri GG, Lew Yan Voon LC. Electronic structure of silicon-based nanostructures. Phys Rev B 76:075131 (2007)
8. Cahangirov S, Topsakal M, Akturk E, Sahin H, Ciraci S. Two- and one- dimensional honeycomb structures of silicon and germanium. Phys Rev Lett 102:236804 (2009).
9. Lebegue S, Eriksson O. Electronic structure of two-dimensional crystals from ab initio theory. Phys Rev B 79:115409 (2009).
10. Ni Z, et al. Tunable bandgap in silicene and germanene. Nano Lett 12:113–118 (2012).
11. Drummond ND, Zolyomi V, Fal'ko VI. Electrically tunable band gap in silicene. Phys Rev B 85:075423 (2012).
12. Ezawa M. A topological insulator and helical zero mode in silicene under an inhomogeneous electric field. New J Phys 14:033003 (2012).
13. Ezawa M. Valley-polarized metals and quantum anomalous Hall effect in silicene. Phys Rev Lett 109:055502 (2012).
14. Stille L, Tabert CJ, Nicol EJ. Optical signatures of the tunable band gap and valley-spin coupling in silicene. Phys Rev B 86:195405 (2012).
15. Zheng, et al. Nanoscale Research Letters 7:422 (2012)
16. Ya Feng, Defa Liu, BaojieFeng and XuLiu et.al. PNAS 113: 51:14656-14661.(2016)

Photoemission Study of the Dirac cone state splitting at the Dirac point for Gd-doped Topological Insulators

D. Estyunin[a], A.V. Koroleva[a], A.M. Shikin[a],

S. Kumar[b], E.F. Schwier[b], A. Kimura[b,c]

[a]*Saint Petersburg State University, 198504 Saint Petersburg, Russia*
[b] *Hiroshima Synchrotron Radiation Center, University of Hiroshima, Higashi-Hiroshima 739-0047, Japan*
[c] *Graduate School of Science, Hiroshima University , Higashi-Hiroshima 739-8526, Japan*

Keywords: Topological Insulators, ARPES, Electronic Structure.

In recent years, magnetically-doped topological insulators (TIs) have attracted enhanced interest due to possibility of effective realization Quantum Anomalous Hall effect (QAHE) [1,2]. For the effective realization of the QAHE in magnetically-doped TIs the Dirac gap should be located at the Fermi level (FL) [1,2] and the developed surface ferromagnetism (FM) should survive in the insulating regime, i.e. should be independent on bulk carriers.

The key challenge to realizing the QAHE is to achieve simultaneously a low bulk carrier density together with an appropriate ferromagnetic ordering. Unfortunately, the incorporated transition metal (TM) atoms act as not only magnetic dopants. The doping by magnetic TM impurities leading to opening the Dirac gap is also followed by the charge carrier doping effects simultaneously. TMs are usually divalent and, therefore, substitution of Bi^{+3} with TM^{+2} creates hole dopants into the system. On the other hand, if the doping elements are rare-earth metals such as Gd, which are trivalent, no charge carriers are doped and only magnetic moments can be induced [3]. Gd has an equal number of bonding electrons to Bi, therefore, the isoelectric substitution with Gd into Bi_2Te_3 takes place. Under Gd-doping the lattice parameters of the host TI are not changed due to the Gd substitution.

The current work is devoted to study of the features of electronic structure and magnetic properties of Gd-doped TIs with stoichiometry $Bi_{2-x}Gd_{0.06}Sb_xTe_3$, for x is between 0.75 and 0.95, when the Dirac gap is located in the region of the FL and analysis of the gap open at the Dirac point (DP) at different positions of the DP relative to the FL.

Fig. 1.a shows the ARPES dispersion map measured for Gd-doped topological insulators with stoichiometry $Bi_{1.19}Gd_{0.06}Sb_{0.75}Te_3$ at temperature 15K at photon energy of 28 eV under photoexcitation by linear p-polarized synchrotron radiation SR. In Fig. 1.b the ARPES dispersion maps in the form d^2N/dE^2 are also presented for better visualization of the electronic structure in the region of the DP and possible splitting of the Dirac cone states at the DP developed due to influence of the magnetic doping. One can distinguish formation of the dip at the DP testifying to splitting of the Dirac cone states at the DP. Fig. 1.c shows the EDC-profile cut directly at the DP (at $k_{II}=0$). The fitting of the EDC demonstrates decomposition on two spectral components related to the Dirac cone states at the DP (red lines) separated by the energy of about 30 meV and the spectral component corresponding to the valence band states (black line). We relate this splitting (30 meV) to the splitting between the upper and lower Dirac cone states due to spontaneous out-of-plane magnetic moment developed for $Bi_{1.19}Gd_{0.06}Sb_{0.75}Te_3$ at temperature of 15 K.
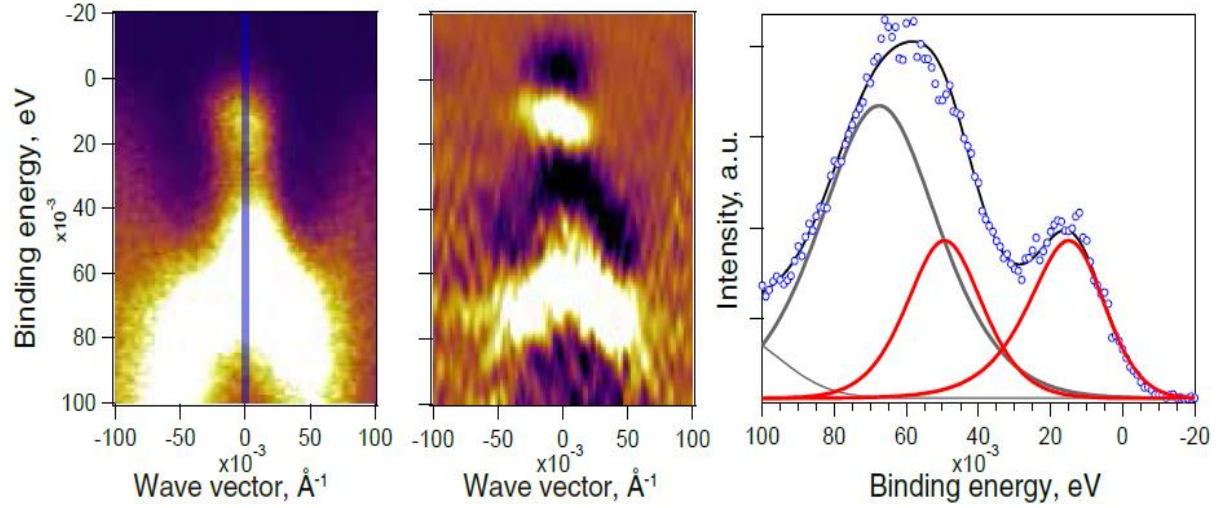
Fig.1. The ARPES dispersion maps for the DC states measured for $Bi_{1.19}Gd_{0.06}Sb_{0.75}Te_3$ at temperature 15K and photon energy of 28 eV in the form of N(E) – (a) and d2N/dE2 – (b) presentations. (c) - the corresponding EDC-profile measured directly at the Γ-point (kII=0) with fitting on the spectral components related to the DC states (red lines) and the upper edge VB state contribution (grey line)

It means that the Gd-doping open the Dirac gap at the DP for $Bi_{1.19}Gd_{0.06}Sb_{0.75}Te_3$ at temperature of 15 K up to 30 meV. In future experiment we will study how the Dirac gap will depend on the Gd-concentration and the position of the DP relative to the FL for different stoichiomentry of Gd-doped TI.

REFERENCES

1. C.-Z. Chang et al., Science **340**, 167 (2013).
2. C.-Z. Chang et al.,, Nat Mater **14**, 473 (2015).
3. J. Kim et al., Sci. Rep 5, 10309 (2015)

Resonant Photoemission Study of Mn-doped Topological Insulators

A.M. Shikin[a], D. Estyunin[a], A.V. Koroleva[a], I.I. Klimovskikh[a],

S. Kumar[b], E.F. Schwier[b], A. Kimura[b,c]

[a]*Saint Petersburg State University, 198504 Saint Petersburg, Russia*
[b] *Hiroshima Synchrotron Radiation Center, University of Hiroshima, Higashi-Hiroshima 739-0047, Japan*
[c] *Graduate School of Science, Hiroshima University , Higashi-Hiroshima 739-8526, Japan*

During recent decades active research into fundamentally new structures – topological insulators (TIs) – is one of the priority areas in the physics of nanosystems. An intriguing electronic structure configuration of TI defines the researchers' special expectations for their application in spintronics, optoelectronics, quantum computations and other technologically important fields. Recently, it has been demonstrated that at very low temperatures (~ 1 K) the topological insulators with time-reversal symmetry broken due to the magnetic doping (Cr, V) exhibit the possibility of the quantum anomalous Hall effect (QAHE) realization [1,2]. Such effect becomes possible due to the local magnetic gap opening at the Dirac point caused by lifting Kramers degeneracy between up and down spins.

Significantly larger Dirac point gap has been observed in Mn-doped topological insulator, and the hedgehog out-of-plane spin structure, linked to the magnetic interaction has been confirmed [3]. However, recent detailed investigations of the electronic structure of Mn-doped TIs reveal the survival of the Dirac point gap up to the room temperature, and moreover, similar gap values had been observed for non-magnetic doping of TIs [4]. Resonant photoemission on the Mn-edge confirms the presence of Mn d states near the Dirac point, that can induce the apparent gap to the ARPES spectrum via the hybridization with topological surface states.

Nevertheless, more recent studies demonstrate the possibility of transformation of the TI's surface layers under the Mn doping with formation of the novel magnetic compounds [5]. Such a structure is characterized by the large magnetic Dirac point gap that is caused by surface magnetic ordering. Thus, the main aim of the present work is the investigation of the electronic structure of highly Mn-doped topological insulators, including the resonant photoemission analysis in order to distinguish the Mn impurity states at the Dirac point and reveal the surface magnetic ordering.

The experimental ARPES images of Mn-doped Bi2Te3 taken at the photon energies of 48 and 50 eV are shown in Fig. 1a,b. These photon energies correspond to off- and on- Mn-edge resonance, relatively. One can clearly see the dispersion relations of the valence band of topological insulator in the region of 0.5-5 eV of binding energy.   In the region of BE of 0-0.5 eV the Dirac cone states are located takes plce while having the very low intensity at these photon energies. Fig. 1 c shows the normalized difference between the ARPES dispersion maps measured off- and on- Mn-edge resonance (a and b), where one can distinguish the well pronounced Mn resonant state at ~3.8 eV. It is well visible in Fig. 1.d. Additionally, Mn impurity states are visible at the BE of 1 eV. Most import that there is no any enhancement of the intensity visible in the region of the Dirac cone, i.e. 0-0.5 eV. It means that the gap open at the Dirac point for highly Mn-doped topological insulator is not related to the hybridization effect. It is rather related to the induced magnetic moment influence.
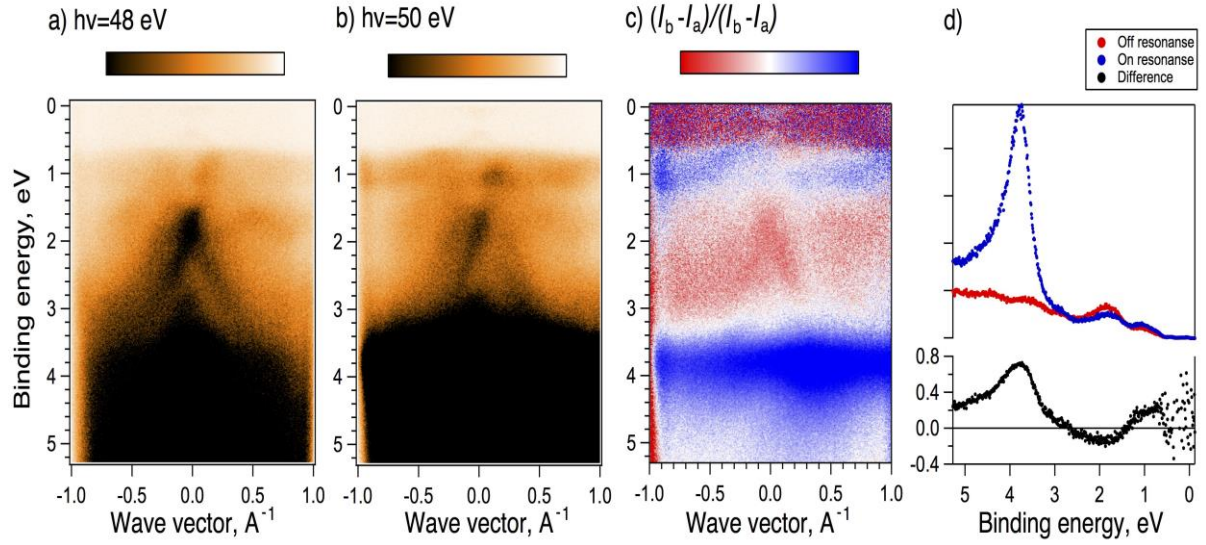
Fig.1 ARPES images of Mn-doped Bi2Te3 taken at 48 (a) and 50 eV (b). (c) - Normalized difference between images a and b.. (d) - EDC spectra at the Gamma-point at photon energy of 48 (red) and 50 eV (blue). Normalized difference between the spectra is presented by black curve.

Thus, our results show the large resonant signal from the Mn impurity states of highly Mn-doped topological insulator Bi2Te3 located in the region of the bulk valence band of TI at the binding energy of 3.8 eV. The absence of the resonant features in the region of the Dirac point allows to ascribe the gap open at the Dirac point to influence of magnetic ordering. Detailed investigation of the Dirac cone structure will be carried in the future experiments.

REFERENCES

1. C.-Z. Chang et al., *Science 340, 167-170*2 (2013)
2. S. Qi et al., Phys. Rev. Lett. 117, 056804 (2016)
3. S. Y. Xu. et al., Nat. Phys. 8, 616 (2012)
4. J. Sanchez-Barriga et al., Nat. Commun. 7, 10559 (2016)
5. T. Hirahara et al., Nano Lett., 7, 3493–3500 (2017)

Probing Correlated Topological Phase in CeBi
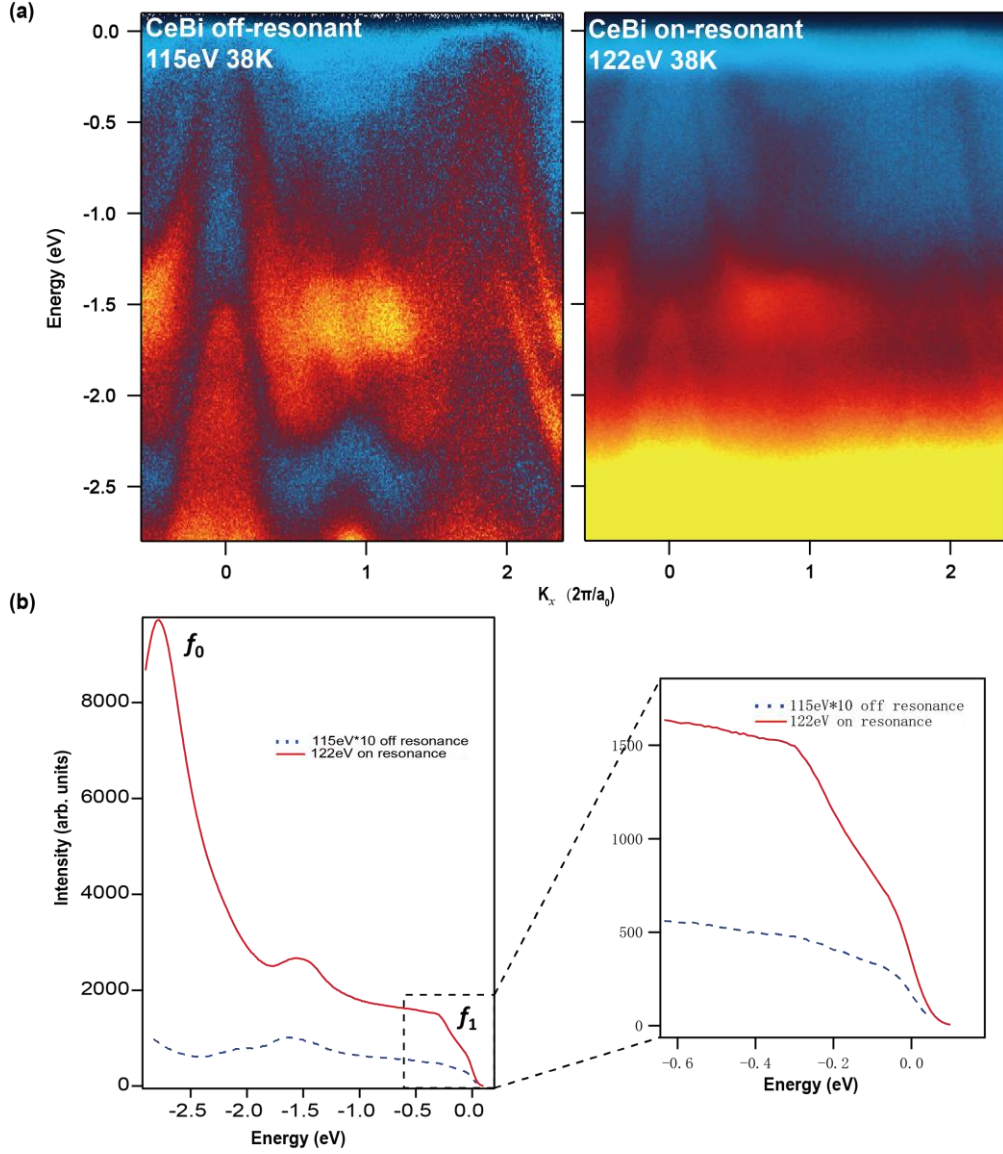
Peng Li, Zhongzheng Wu, Yang Liu[*]

Center for Correlated Matter and Department of Physics, Zhejiang University, Hangzhou, China

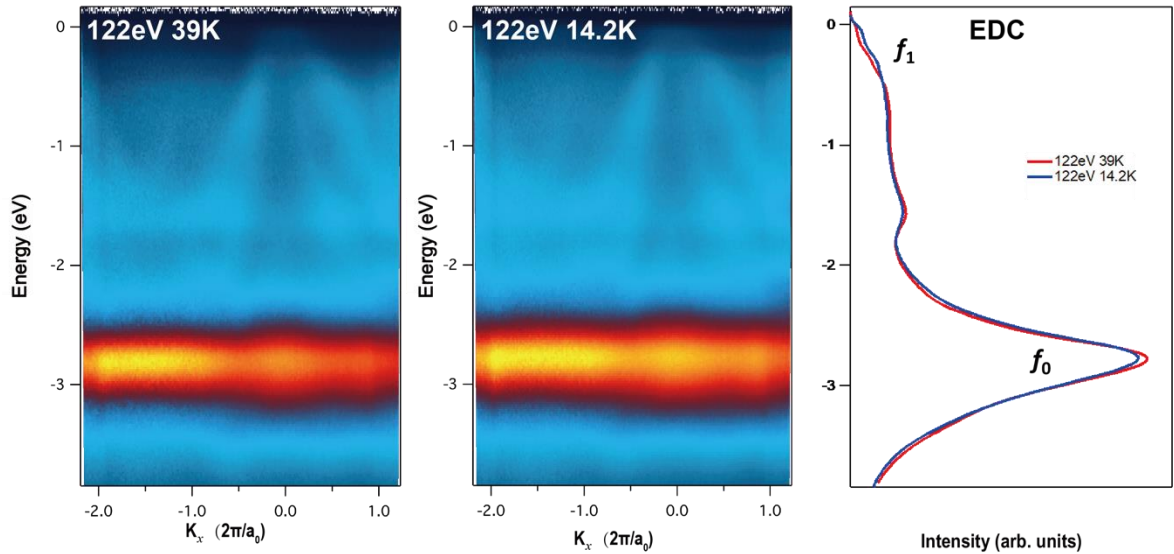**Keywords:** Topological Insulator/semimetal, Electron Correlation.

Recently topological insulators and semimetals have attracted considerable research interest. Interplay between nontrivial band topology and strong electron correlation could induce exotic electronic phase, including weyl-kondo semimetal [1]. Here, we focus on CeBi, a kind of topological insulator with partial gap, to find evidence of correlated topological states via angle resolved photoemission spectroscopy (ARPES). Rare earth mono-bismuthides have a simple rocky-salt structure, and the electronic structure at high temperature has been well studied by several groups [2-4] and in our former paper [5], which features two holes pockets at $\bar{\Gamma}$ point, one electron pocket at $\bar{X}$ point in momentum space with non-trivial band topology. CeBi has exotic magnetic properties where a PM to type-I AFM transition takes place at 25 K and type-I AFM to type-II AFM transition occurs at 11 K [6]. Meanwhile with decreasing temperature, f-electron could hybridize with conduction electrons and become partially itinerant, as proposed by previous theoretical calculations. Actually, transport experiments have revealed the kondo-like features, so our main purpose is to find the evidence of the (weak) hybridizations between f and conduction electrons.

The cross-section of f orbital is generally small in low photon energy range. So we did the resonant photoemission experiments which occur at ~122 eV (4d to 4f transition), at BL-1 in HiSOR. Because of the large enhancement of f-orbital features, resonant photoemission experiment can be used to identify the f electron spectral feature. Fig. 1 shows the results from on and off resonance ARPES experiments, where we use 115 eV as off resonance photon energy and 122 eV as on resonance photon energy. Fig.1(a) shows the energy-momentum dispersion on 115 eV and 122 eV, respectively. Compared with off resonance data, 4f electron peaks at binding energy 2.82eV and 0.3eV show up under resonance condition, which corresponds to $4f^0$ and $4f^1$ final state, respectively. We also integrate the energy distribution curve (EDC) as Fig.1 (b), one can see the obvious enhancement of the 4f peaks, i.e., on-resonant intensity (122eV) is more than 10 times larger than off-resonant intensity (115eV). A zoom-in view near the Fermi level (the right-bottom panel) reveals the fine structure such as the spin-orbit coupling satellite of Kondo resonance state at 0.3 eV [7], although the Kondo resonance peak right below the fermi level is rather weak due to the low carrier density (corresponding to a low single-impurity Kondo temperature).

We also performed temperature dependent measurements, from 39 K (PM phase) to 14.2 K (AFM phase). The left and middle panels in fig. 2 show on resonance spectrum taken above and below magnetic transitions, respectively. Small yet obvious intensity weight changes can be found in EDC, where the local $4f^0$ state's intensity decreases upon cooling down towards AFM phase, while more itinerant $4f^1$ state intensity grows up. More importantly, if one integrates each EDC, one could find the overall spectral weight to be conserved, indicating that the increase of $4f^1$ spectral weight originates from the decreasing intensity from $4f^0$. In other words, more f electrons of CeBi become itinerant when temperature goes down from PM to AFM. However, no direct signature of f-c hybridization could be observed in the momentum-energy dispersion relations, likely due to the rather weak Kondo interaction in such a low carrier density system. Nevertheless, the subtle spectral weight shift indicates (at least) weak Kondo hybridization at low temperature, whose origin remains to be revealed.

FIGURE 1. Off and on resonant measurements of CeBi. (a) off and on resonant spectrum at 115 eV and 122 eV, respectively. And all measurements ware at PM state (38K). (b) the integrated EDC of (a), and the right-bottom panel is the zoom-in version near the fermi level.

FIGURE 2. Temperature dependence measurements on 122eV, from high temperature 39K (PM state) to low temperature 14.2K (AFM state), the right panel is the integrated EDC of these two cases.

REFERENCES

1. Hsin-Hua Lai, Sarah E. Grefe, Silke Paschen, and Qimiao Si, "Weyl-Kondo semimetal in heavy-fermion systems", PNAS, 2018, pp. 93-97.
2. Jayita Nayak, Shu-Chun Wu, eg. "Multiple Dirac cones at the surface of the topological metal LaBi", Nature Communications 8, 13942 (2017).
3. H. Kumugashira, S.-H. Yang, eg, "High-resolution angle- resolved photoemission spectroscopy of CeBi", Phys. Rev. B 54, 9341 (1996).
4. Kenta Kuroya, M. Ochi, eg, "Experimental Determination of the Topological Phase Diagram in Cerium Monopnictides", Phys. Rev. Lett. 120, 086402 (2018).
5. Peng Li, Zhongzheng Wu, Yang Liu, eg, "Tunable Electronic Structure and Possible Topological Surface States in rare Earth Mono-Bismuthides with Partially Filled f shell", arXiv: 1802.03111(2018).
6. H. Bartholin, D. Florenoe, Wang Tcheng-si, and O. Vogt, "Magnetic Properties of CeBi", Phys. stat. sol. (a) 24, 631 (1974).
7. Sooyoung Jang, Robert Kealhofer, et al., "Direct visualization of coexisting channels of interaction of CeSb", arXiv: 1712.05817 (2017).

ARPES study of Gd: Bi_2Se_3 topological insulators

Rahul Singh[a], Shiv Kumar[b], Eike F. Schwier[b], Kenya Shimada[b], Anup K. Ghosh[c] and Sandip Chatterjee[a]

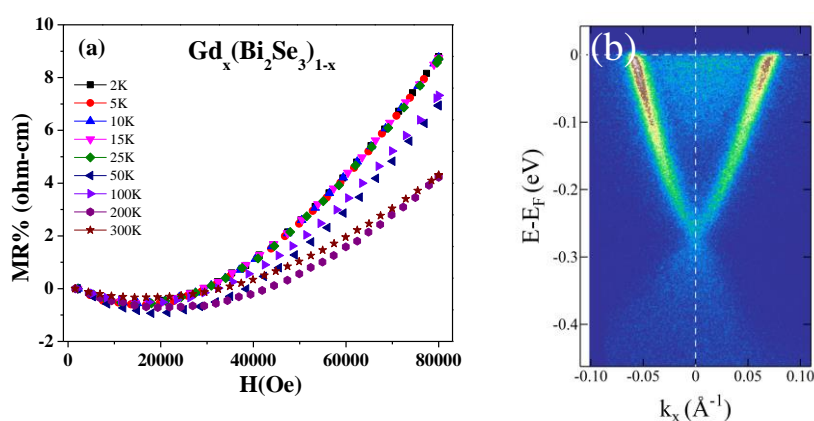[a]*Department of Physics, Indian Institute of Technology (BHU), Varanasi-221005, India*
[b]*Hiroshima Synchrotron Radiation Center, Hiroshima University, Higashi-Hiroshima 739-0046, Japan*
[c]*Department of Physics, Banaras Hindu University, Varanasi-221005, India*

Keywords: Topological insulators, electronic structure, negative magnetoresistance.

In recent years magnetic three-dimensional topological insulators (MTIs) based on Bi_2Te_3 and Bi_2Se_3 have been interesting subject due to their fundamental interesting phenomena viz. quantum anomalous Hall effect, three-dimensional Weyl fermion etc. The strong spin-orbit coupling (SOC) leads nontrivial band topology in these material, in which spin of an electron is locked perpendicular to its momentum in chiral spin structure, whereas electrons with the opposite momenta have opposite spin that makes topological insulator potentially very promising material that could be used in spintronics and for quantum computing applications. [1-4]

The transport studies of topological surface state (TSS) have revealed such as Aharonov-Bhom oscillation in Bi_2Se_3 nano-ribbon [5] weak antilocalization in Bi_2Se_3 and Bi_2Te_3 film and two dimensional (2D) Shubnikov-de Hass (SdH) oscillations are powerful means to distinguish between bulk and surface charge carrier via angle-dependent. [6] Recently, magnetotransport measurement on Bi_2Se_3 epitaxial layers in the magnetic field shows negative magnetoresistance (NMR) when the magnetic field applied parallel to I ($I \parallel B_x$). [7] However, the recent explosion of interest in 3D massless Dirac fermions in 3D Dirac Weyl semimetals shows an extremely large positive magnetoresistance under perpendicular magnetic field and more specially, the negative longitudinal magneto-resistance (NLMR) predicated to appear in Weyl semimetals when the magnetic and electric field coaligned to axial anomaly. [8] Consequently, NLMR is not a unique property of Weyl semimetal. We have observed first-time NLMR in $Gd_{0.5}(Bi_2Se_3)_{0.95}$ sample which persist until 2.5 tesla under perpendicular magnetic field parallel to c-axis up to room temperature.

FIGURE 1: Fig (a) shows the longitudinal resistance vs temperature of $Gd_{0.5}(Bi_2Se_3)_{0.95}$ sample. Fig. (b) displays the band structure near Fermi surface of $Gd_{0.5}(Bi_2Se_3)_{0.95}$ by angle-resolved photoemission spectroscopy (ARPES) at 18 K.

The band dispersion measured by Laser-ARPES along high symmetry direction (K-Γ-K) shows that $Gd_{0.5}(Bi_2Se_3)_{0.95}$ sample is n-type, which is consistent with Hall-resistivity data. The binding energy of Dirac point relative to the Fermi level − 0.302 eV, it is due to e⁻ doping in the sample, in this case, e⁻ is generated by Gd-intercalation.

In summary, we have synthesized and study the bulk and surface state electronic properties of $Gd_{0.5}(Bi_2Se_3)_{0.95}$ using Laser-ARPES. We have also studied the magnetotransport properties of Gd-intercalated Bi_2Se_3 TI material and observed NMR exist when we have applied magnetic field perpendicular to the electric field.

REFERENCES

1. J. Y. Ando, *J. Phys. Soc. Jpn.* **82**, 102001 (2013)
2. R. Yu, W. Zhang, H.-J. Zhang, S.-C. Zhang, X. Dai, and Z. Fang, *Science* **329**, 61 (2010).
3. X.-L. Qi, R. Li, J. Zang, and S.-C. Zhang, *Science* **323**, 1184 (2009).
4. S.-W. Kim and M.-H. Jung, *Appl. Phys. Lett.* **112**, 202401 (2018).
5. G. Li, D. Liang, R. L. J. Qiu, and X. P. A. Gao, *Appl. Phys. Lett.* **102**, 043104 (2013).
6. Y.-Y. Lv, B.-B. Zhang, X. Li, K.-W. Zhang, X.-B. Li, S.-H. Yao, Y. B. Chen, J. Zhou, S.-T. Zhang, M.-H. Lu, S.-C. Li, and Y.-F. Chen, *Phys. Rev. B* **97**, 115137 (2018).
7. S. Wiedmann, A. Jost, B. Fauqué, J. van Dijk, M. J. Meijer, T. Khouri, S. Pezzini, S. Grauer, S. Schreyeck, C. Brüne, H. Buhmann, L. W. Molenkamp, and N. E. Hussey, *Phys. Rev. B* **94**, 081302 (2016).
8. F. C. Chen, H. Y. Lv, X. Luo, W. J. Lu, Q. L. Pei, G. T. Lin, Y. Y. Han, X. B. Zhu, W. H. Song, and Y. P. Sun, *Phys. Rev. B* **94**, 235154 (2016).

ARPES Study on the New Fermion in ZrTe and the electronic structure of Monolayer MoTe$_2$

Qiang Gao[1,2], Wenjuan Zhao[1,2], Wenliang Zhu[1,2], Genfu Chen[1], Yuan Huang[1],
Ya Feng[3], E. Schwier[3], K. Shimada[3], Guodong Liu[1*], Xingjiang Zhou[1,4*]

[1] National Laboratory for Superconductivity, Beijing National Laboratory for Condensed Matter Physics, Institute of Physics, Chinese Academy of Sciences, Beijing, 100190, China
[2] University of Chinese Academy of Science, Beijing, 100049, People's Republic of China
[3] Hiroshima Synchrotron Radiation Center, Hiroshima University, 2-313 Kagamiyama, Higashi-Hiroshima, Hiroshima 739-0046,, Japan
[4] Collaborative Innovation Center of Quantum Matter, Beijing 100871, China

Keywords: new fermion,   ZrTe, 2D material, transition metal dichalcogenids (TMDCs), mono-layer MoTe$_2$, ARPES.

The topological quantum materials, representing a new state of condensed matter, have attracted remarkable interest in recent years. Many of them have been predicted in theory and realized in experiment, including three-dimensional or two-dimensional topological insulators [1–3], three- dimensional Dirac semimetals [4–6], three-dimensional Weyl semimetals [7–9], and nodal line semimetals [10,11]. The latest development is the theoretical prediction and experimental verification on the "new Fermion" topological semimetal with quite interesting physical properties [12-15], which are characterized by three-, six- or eight-fold degenerate band crossing points. Many candidate materials hosting such "new Fermions" have been proposed through ab-initio calculation. Among such materials, only the MoP and WC have been preliminarily confirmed by recent ARPES measurements to own a triply degenerate point in the band structure [16, 17]. ZrTe, one of the WC-structure family of materials, was reported as an intriguing material that hosts both the "three-fold degenerate new Fermion" state and Weyl Fermion state near Fermi energy [14,18]. It calls for a systematic research on the electronic structure to study the topological nature on the new fermion in ZrTe.

Transition metal dichalcogenides (TMDCs) are currently hot-spot materials for their rich physical and optical properties. Among various MX$_2$, MoTe$_2$ comes into notice for its structural phase transition from 2H to 1T' by an electrostatic-doping in monolayer[19]. However, there's almost no band structure study on 2D MoTe$_2$ with 2H-type lattice [20], which calls for a systematic ARPES study on them.
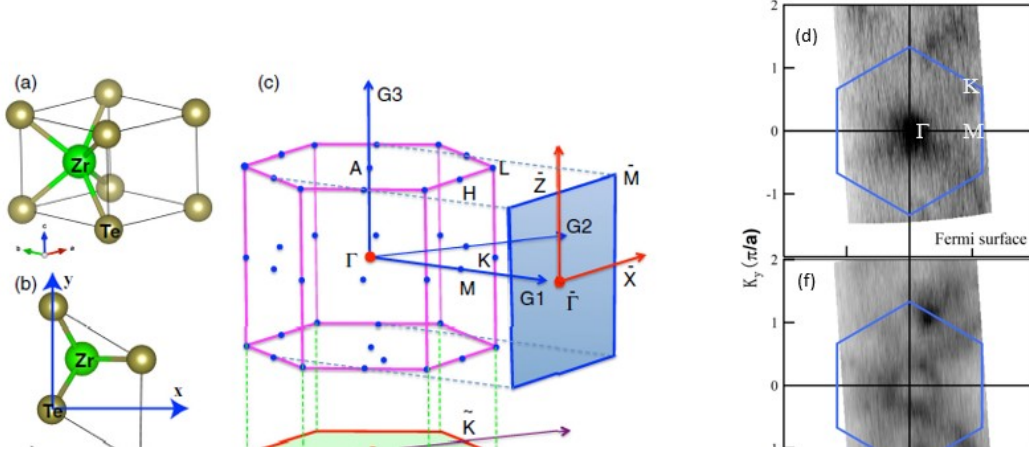
The approved beam time in HiSOR were used to do Angle Resolved photoemission Spectroscopy (ARPES) measurements on new fermion semimetal ZrTe and monolayer MoTe2.

First, we measured ZrTe. We changed the photon energy from 30eV to 100eV, and found the band structure is clear at 52eV. Then we fixed the photon energy at 52eV and got good mapping. In Fig.1 (c), we can see that the projected brillouin zone on (001) surface is six-fold symmetrical. And in Fig.1 (d) to (g), we got a six fold symmetrical electronic structure. This indicates that the cleaved surface is (001) plane. As the sample size is too small, and the photon beam size is much bigger than sample, the signal is weak and the background is high. But we can still recognize hole pockets around Γ and K poins.
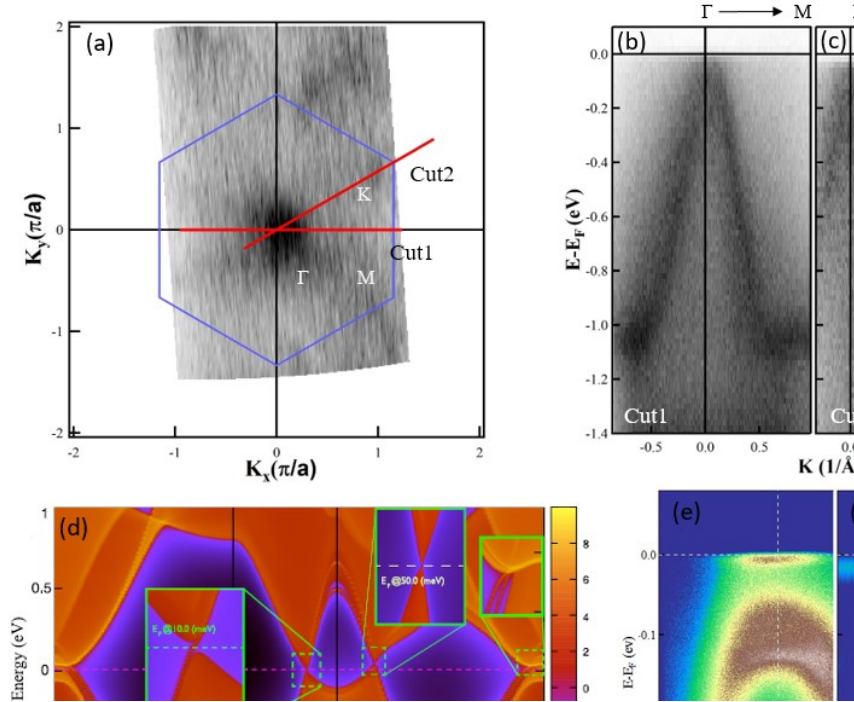
In Fig.2, we show band structures on the high symmetry cuts along Γ M and Γ K direction. In Fig.2(b) we can only resolve one hole-like band at Γ point. While Fig.2(c) along Cut2 shows more hole like bands at K point but not being clearly resolved. They look very similar to the calculated band structures in Fig.2(d). Fig.2(e) and (f) show the detailed band structure crossing Γ point measured with 7eV laser, we can see clear band splitting of the hole like band and a very flat band bottom of an electron pocket lying at Fermi level.

In summary, we got good band mapping along high symmetry cuts in ZrTe at (001) surface. The band structure in the whole Brillouin zone can roughly fit the band calculation. But we miss some critical details due to sample size and instrument resolution issue, even 7eV laser data can be a supplement. To pin down the topological nature of ZrTe, we need to measure other cleaved surfaces and do photon energy
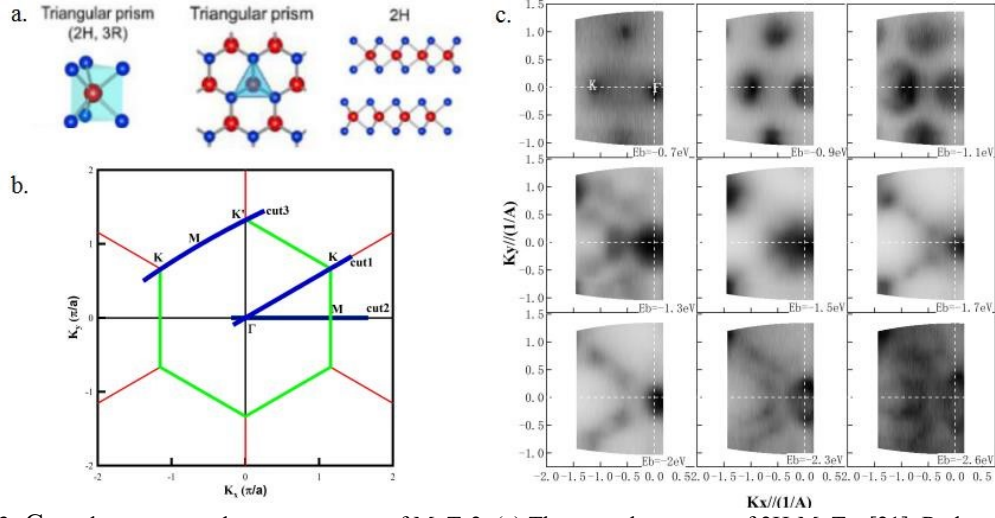
dependence mapping.

FIGURE 1. The electronic structure of ZrTe. (a) The crystal structure of WC-type ZrTe and (b) the top view [14]. (c) The bulk Brillouin Zone and its projection onto the (100) and (001) surface. The high symmetrical crystal momenta are indicated with letters[14]. (d)-(g) The Fermi surface and constant energy contours of ZrTe on (001) surface measured with photon energy at 52eV.
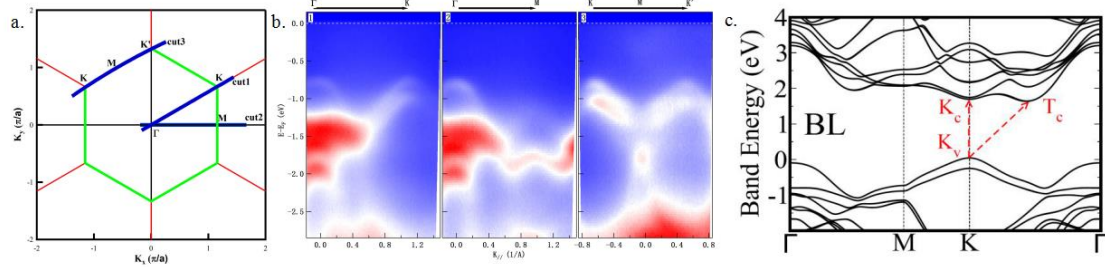

Figure 2. (a) Fermi surface of ZrTe with guideline of cuts. Band dispersion on Cut 1 along Γ M direction(b) and on Cut 2 along Γ K direction (c). (d) Calculated band structure along high symmetry direction [14]. (e) The measured band along a cut at Γ point measured with 7eV laser in our home lab and (f) The EDC second derivative image for (e).

For monolayer $MoTe_2$ sample, we first annealed the sample in the preparation chamber, and then transferred to analysis chamber. In Fig.3, it gives the crystal structure and energy contour of $MoTe_2$ film. Fig.3(a) and (b) show the crystal structure [21] and Brillouin zone (BZ). We got energy contour by ARPES in Fig.3(c). Because $MoTe_2$ is a typical semiconductor, there's no electron density of states between Fermi energy and -0.7 eV binding energy. At -1.1eV binding energy, the energy contour clearly show a splitting triangle at K point, which is corresponding with the SOC splitting at K.

Fig.4 shows the electronic structure along high symmetry direction. We can see the classical SOC splitting at K. Compared with the reported data, our ARPES result is consistent with band calculation of bi-layer $MoTe_2$. By Lorentz fitting of EDC, we get a band splitting of ~ 200meV at K point.

FIGURE 3. Crystal structure and energy contour of MoTe2. (a) The crystal structure of 2H-MoTe$_2$ [21]. Red and blue balls stand for Mo and Te atoms, respectively. (b) The hexagonal Brillouin zone (BZ) of MoTe$_2$. Green line and Red line constitute MoTe$_2$ BZ. Blue lines are momentum position in Fig.2. (c) Energy contour of bi-layer MoTe$_2$ film.

FIGURE 4. Band structure of MoTe$_2$ film along high symmetry directions.(a) The Brillouin zone of MoTe$_2$ and cuts in measurements. (b) Electronic band structures along high symmetry direction. The corresponding momentum positions are shown in (a) by blue lines. (c) The calculated band structure for double layer MoTe$_2$ [22].

In conclusion, we get some good experimental results about ZrTe and bilayer MoTe$_2$ which have not been reported in literature. The band structures are basically in accord with band calculations. To publish the obtained results, more experiments need to be done on other cleaved surfaces of ZrTe and mono layer MoTe$_2$.

REFERENCES

1. Hasan MZ and Kane CL. , Rev Mod Phys **82**, 3045 (2010).
2. Qi XL and Zhang SC , Rev Mod Phys **83**, 1057(2011).
3. Ando Y. , J Phys Soc Jpn **82**, 102001 (2013).
4. Liu ZK, Zhou B, Zhang Y, et al., Science **343**, 864 (2014).
5. Xu SY, Liu C, Kushwaha SK, et al., Science **347**, 294 (2015).
6. Liu ZK, Jiang J, Zhou B, et al., Nat Mater **13**, 677-681 (2014).
7. Xu SY, Belopolski I, Alidoust N, et al., Science **349**, 613-617 (2015).
8. Lv BQ, Weng HM, Fu BB, et al., Phys Rev X **5**, 031013 (2015);5:031013.
9. Yang LX, Liu ZK, Sun Y, et al., Nat Phys **11**, 728-732 (2015).
10. Neupane M, Belopolski I, Hosen MM, et al., Phys Rev B **93**, 201104 (2016).
11. Schoop LM, Ali MN, Strasser C, et al., Nat Commun **7**, 11696 (2016).
12. B. Bradlyn, J. Cano, Z. Wang, et al., , Science **353**, aaf5037 (2016).
13. Zhu, Z., Winkler, G. W., Wu, Q. S., et al., Phys. Rev. X **6**, 031003 (2016).
14. Weng, H., Fang, C., Fang, Z. & Dai, X., Phys. Rev. B **94**, 165201 (2016).
15. Chang, G. et al,. Scientific Reports **7**, 1688 (2017).
16. B. Lv, Z.-L. Feng, Q.-N. Xu, et al., Nature **546**, 627 (2017).
17. J.-Z. Ma, J.-B. He, Y.-F. Xu, et al., Nature Physics **14**, 349-354 (2018).
18. W. L. Zhu, J. B. He, S. Zhang, et al., arXiv:1707.00942.
19. Ying Wang, Jun Xiao, et al., Nature **550**, 487-491 (2017).
20. Th. Boker, A. Muller, et al, Phys. Rev. B 60, 4675 (1999).
21. YJ Zhang, et al., 2D Mater **2**, 044004 (2015).
22. C. Robert, et al., Phys. Rev. B, **94**, 155425 (2016).

XPS study of boron-doped diamond films covered by V_2O_5
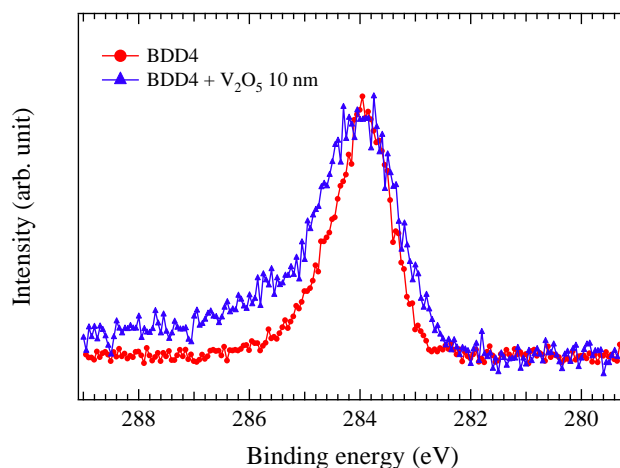
Y. Muraoka[a], T. Wakita[a], T. Yokoya[a]

[a]Research Institute for Interdisciplinary Science, Okayama University Okayama 700-8530, Japan

Keywords: XPS, Boron-doped diamond(100) films, V_2O_5

X-ray photoemission spectroscopy (XPS) study of the boron-doped diamond films covered by V_2O_5 thin films is performed. It is reported that in H-terminated diamond (100) films covered by V_2O_5 the efficient surface transfer doping of H-diamond by V_2O_5 takes place due to the nature of negative electron affinity in H-diamond (100) surface [1, 2]. It would be interesting to see whether the boron-doped diamond(100) superconducting films are available instead of the diamond(100) films. In this work, we investigate the valence state of carbon and vanadium in boron-doped diamond films without and with the cover of V_2O_5 films to clarify the possibility of surface transfer doping of the boron-doped diamond by V_2O_5 films.

Boron-doped diamond(100) films are prepared by a hot-filament chemical vapor deposition method on diamond(100) substrates [3]. The thickness of the boron-doped films is about 0.5 micrometer. V_2O_5 thin films are fabricated on the boron-doped diamond(100) films by a pulsed laser deposition (PLD) technique. The thickness of V_2O_5 films is approximately 10 nm. XPS measurements were carried out on the beamline BL-5, at the Hiroshima Synchrotron Radiation Center in Hiroshima University. Photon energy was set at 350 and 660 eV. Fermi level position was determined by measuring the molybdenum spectra. All measurements are carried out at room temperature.

Figure 1 shows the C $1s$ core-level spectra of the boron-doped diamond(100) films without and with the cover of V_2O_5 thin films. The C $1s$ signal is clearly observed for both films. The peak position for the films without the cover of V_2O_5 is 284.0 eV which is the same as that for the films with V_2O_5 cover, while the peak width of the former films is narrower compared to the latter. In the presentation, the results of vanadium $2p$ core-level spectra will be shown.

FIGURE 1. C1s core-level spectra for boron-doped diamond(100) films without and with the cover of V_2O_5 thin films. Photon energy of 350 eV was used.

REFERENCES

1. K. G. Crawford, L. Cao, D. Qi, A. Tallaire, E. Limiti, C. Verona, A. T. S. Wee, and D. A. J. Moran, Appl. Phys. Lett. **108,** 042103 (2016).
2. C. Verona, W. Ciccognani, S. Colangeil, E. Limiti, M. Marinelli, and G. V. Rinati, J. Appl. Phys. **120,** 025104 (2016).
3. T. Doi, T. Fukaishi, C. Hiramatsu, T. Wakita, M. Hirai, Y. Muraoka, T. Yokoya, Y. Kato, Y. Izumi, T. Muro, and Y. Tamenori, Diam. Relat. Mater. **25,** 5 (2012).

Photoelectron Spectra of Lutetium Encapsulated Fullerenes

T. MIYAZAKI[a], T. Wakita[a], T. YOKOYA[a], H. SHINOHARA[b] and S. HINO[c]

[a] *Research Laboratory for Surface Science, Okayama University, Okayama 700-8530, Japan*
[b] *Graduate School of Science, Nagoya University, Chikusa-ku, Nagoya, 464-8602, Japan*
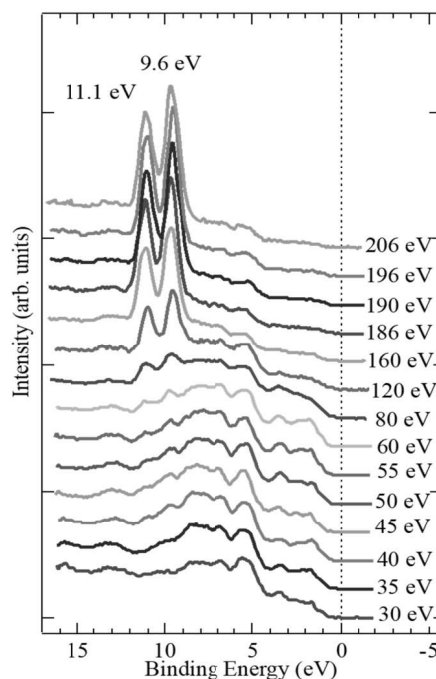[c] *Graduate School of Science and Engineering, Ehime University, Matsuyama, 790-8577, Japan*

Fullerene cages often encapsulate metal atom(s). The encapsulated atom(s) donate electrons to fullerene cages which induces the change of their electronic structure. Ultraviolet photoelectron spectroscopy is a direct method to determine the electronic structure. Recently, Lutetium atoms encapsulated C_{82} fullerenes have been isolated. In this article, ultraviolet photoelectron spectra (UPS) of $Lu_2@C_{82}$ are presented with $hv = 30 \sim 200$ eV incident photon energy and are discussed on the electronic structure.

The UPS of the endohedral fullerenes were measured at the beam line 5 of HISOR of Hiroshima University. Specimens for the measurement of the photoelectron spectra were prepared by vacuum deposition of the fullerenes onto a gold deposited metal disk using a resistive heating quartz crucible in a sample preparation chamber directly attached to the measurement chamber. The measured UPS were referenced against Fermi level (E_F) of gold and were plotted as a function of binding energy relative to E_F.

The valence band UPS of $Lu_2@C_{82}$ obtained with $hv = 30 - 206$ eV incident photon energy are shown in Figure 1. The peak intensity in the upper than 9 eV regions monotonously decrease in accordance with the increase of the incident photon energy. This depends on the decrease in excitation cross section of C2p (2s). Their electronic structures in the UPS of fullerenes and endohedral fullerenes appeared in the deeper than 5 eV region are strongly due to σ–electrons that constitutes the C_{82} skeletal C–C bonds and those between $0 - 5$ eV are due to π –electrons. Remarkable difference among these UPS is observed at 9.6 and 11.1 eV. Two structures are only observed in the UPS of Lu entrapped fullerenes. These structures are not observed when the incident photon energy is less than 35 eV, but their intensity becomes stronger in accordance with the increase of the incident photon energy. The ionization energies of Lu $4f_{7/2}$ and $4f_{5/2}$ levels of Lu metal are 7.5 eV and 8.9 eV, respectively [1]. But their binding energies are much higher than those of Lu metal atoms by 2.1 eV. Because of this donation entrapped metal atoms become electron deficit, which brings the ionization energy of entrapped atoms large. These results suggest that two structures are not derived from the electrons of the carbon cage but derived from Lu atom. $Lu4f_{7/2}$ and $Lu4f_{5/2}$ peak are observed

FIGURE 1. The UPS of $Lu_2@C_{82}$ at hv =30-206 eV incident photon energy.

and their binding energies deviate, which could be a good indicator of the electron configuration of these endohedral fullerenes. Thus, the encapsulated metal atoms donate electrons to the cage.

REFERENCE
1. M. Cardona, L. Ley, Photoemission in Solids. I: General Principles, Springer-Verlag, Berlin, 1978.

Current activities of research and education on BL-5 (FY2017)

T. Yokoya, T. Wakita, Y. Muraoka and K. Terashima

Research Institute for Interdisciplinary Science, Okayama University
Research Laboratory for Surface Science, Okayama University, Okayama 700-8530, Japan

Keywords: photoemission spectroscopy, photoelectron emission microscopy

We present an overview of our resent research and educational activities on beamline 5 (BL5) in the fiscal year 2017. Our beamline has two experimental stations in a tandem way. The first station is equipped with an angle-resolved photoemission spectrometer (ARPES), a low energy electron diffraction (LEED) apparatus and an X-ray source. The hemispherical analyzer of ARPES spectrometer (HA54, VSW) has a mean radius of 50 mm and is mounted on a twin axis goniometer in ultra-high vacuum chamber. Using this goniometer, one can perform ARPES and photoelectron diffraction (PED) measurements. It is also possible to perform resonant photoemission spectroscopy (RPES) measurements by using photon energy tunability of synchrotron radiation with X-ray absorption spectroscopy (XAS) measurement. With the X-ray source (XR2E2, FISONS), we can perform an X-ray photoelectron spectroscopy (XPS) measurement for the chemical state analysis and the PED. At the second station, we have installed a photoelectron emission microscope (PEEM, 'PEEM III', Elmitec). PEEM provides a magnified image of lateral intensity distribution of photo-emitted electrons from a sample surface. The spatial resolutions are several ten nanometers with Hg lamp and a few micrometers with synchrotron radiation. The sample is transferred between the ARPES and the PEEM chamber *in-situ*, and one can perform measurements at both stations for the same sample.

In the recent researches on BL-5, we have studied the electronic structure of potassium doped aromatic molecule (K_x picene) [1], iron-based superconductor ($FeSe_xTe_{1-x}$) [2], transition metal di-oxide films such as VO_2 thin films which exhibits a first-order metal-to-insulator transition at 340 K [3], CrO_2 thin films which are known as a half-metallic material [4], and TaO_2 film which is stabilized with a new technique developed in our group [5]. We have also studied the electronic structures of a high quality boron doped diamond film which shows a signature of the highest superconducting transition temperature of 25 K [6] and a high quality single crystal of $YbFe_2O_4$ which is one of multiferroic materials [7], by utilizing RPES at B-K and Fe-$M_{2,3}$ edges, respectively. In this fiscal year, we are studying the electronic states of the boron-doped diamond films covered by the V_2O_5 thin films by the core-level photoemission spectroscopy, and the charge states of Lu atoms in $Lu_2@C_{82}$ by the photon-energy dependence of the valence band photoemission spectra, as presented in this symposium.

We have used the BL-5 for education activity as well, for example, practical education for undergraduate students of Okayama University. The students have an opportunity to study the synchrotron radiation mechanism and to experience XPS measurement which is very useful for the surface science research. We accepted more than 100 students from 2006 to 2012. From 2014, we have started to join the practical lecture for experiments using the beamline end stations in HiSOR for both graduate school students of Hiroshima and Okayama Universities.

REFERENCES

1. H. Okazaki *et al*., *Phys. Rev* **82**, pp. 195114 (5 pp.) (2010).
2. Y. Yoshida *et al*., *J. Phys. Soc. Jpn* **78**, pp. 034708 (4 pp.) (2009).
3. K. Saeki *et al*., *Phys. Rev* **80**, pp. 125406 (5 pp.) (2009).
4. Y. Muraoka *et al*., *MRS Proceedings* **1406** (2012).
5. Y. Muraoka *et al*., *Thin Solid Films* **599**, pp. 125-132 (2016).
6. H. Okazaki *et al*., *Appl. Phys. Lett* **106**, pp. 052601 (5 pp.) (2015).
7. K. Fujiwara *et al*., *Trans. Mater. Res. Soc. Jpn.* **41**, pp. 139-142 (2016).

The Electronic States of D/L Amino Acid Absorbed on WO$_3$

Yoshihiro Nakao[a], Hiroki Ito[b], Yui Ohno[b], Hiroaki Yoshida[c, d] Kenta Adachi[a] and Yuka Horikawa[a]

[a]*Graduate School of Sciences and Technology for Innovation, Yamaguchi University*
1677-1 Yoshida, Yamaguchi, Yamaguchi 753-8512 Japan
[b]*Physics and Informatics, Faculty of Science, Yamaguchi University*
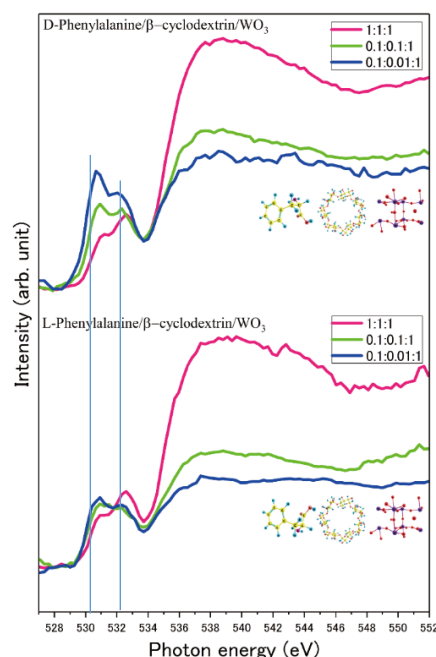*1677-1 Yoshida, Yamaguchi, Yamaguchi 753-8512 Japan*
[c]*Department of Physical Science, Graduate School of Science, Hiroshima University*
1-3-1 Kagamiyama, Higashi-Hiroshima, Hiroshima 739-8526 Japan
[d]*Hiroshima Synchrotron Radiation Center, Hiroshima University*
2-313 Kagamiyam , Higashi-Hiroshima, Hiroshima 739-0046 Japan

A tungsten(VI) oxide (WO$_3$) is the most typical photochromic metal oxide semiconductors. It is known that a color change (colorless $\rightarrow$ blue) corresponding to the reduction of W^{6+} into W^{5+} states in WO$_3$ nanoparticles occurs under UV illumination. It is also known that the photochromism is enhanced when some molecules are adsorbed on the WO$_3$ nanoparticles. For example, when phenylalanine molecules are adsorbed on the WO$_3$ nanoparticles, a color of the WO$_3$ aqueous solution shows darker blue under UV illumination. Phenylalanine is an α-amino acid and has D/L enantiomer. An adsorption ratio of phenylalanine to the WO$_3$ particles is same for D/L phenylalanine in a solution of phenylalanine and WO$_3$. However, when a cyclodextrin(CD) is added in the solution, L-phenylalanine/CD/WO$_3$ solution shows darker blue, that is, the adsorption ratio becomes higher in the L-phenylalanine/CD/WO$_3$ solution. It is proposed that a cyclodextrin inclusion complex with L-phenylalanine is selectively formed and the complex has a high affinity for the WO$_3$ particle.

We have performed soft X-ray absorption spectroscopy of L-phenylalanine/CD/WO$_3$ powder made by solvent drying of the aqueous solution under helium environment. We have confirmed that phenylalanine has a π^* peak at 532.6 eV and WO$_3$ shows a strong resonant peak at 530.8 eV. Figure 1 shows absorption spectra of D (upper) and L-phenylalanine/CD/WO$_3$ (bottom). Graph legends are the component molar fraction of D/L-phenylalanine/CD/WO$_3$. Resonant peak shows characteristic changes for D and L-phenylalanine mixture. When the fraction is 1:1:1, a component fraction of phenylalanine is the highest among all samples and absorption spectra of this sample shows strong resonant peak at 532.6 eV. The spectral shape of 1:1:1 sample is same for D and L-phenylalanine contained powder. A resonance peak at 530.8 eV of upper graph is enhanced when the fraction of phenylalanine decreases (0.1:0.1:1 and 0.1:0.01:1) because a molar fraction of WO$_3$ increases. However, the enhancement of the peak is weak in the bottom graph. We consider it as a result of increase of the adsorption fraction of L-phenylalanine on the WO$_3$ particles; WO$_3$ is less irradiated when the particles are covered with phenylalanine.

FIGURE 1. O K-edge X-ray absorption spectra of Phenvlalanine/ß-cvclodextrin/WO₃.

Development of an apparatus for soft X-ray absorption experiments of solid and liquid samples under atmospheric helium gas environment

Yoshihiro Nakao[a], Hiroki Ito[b], Yui Ohno[b], Hiroaki Yoshida[c, d],
Takashi Tokushima[e, f] and Yuka Horikawa[a]

[a]*Graduate School of Sciences and Technology for Innovation, Yamaguchi University*
1677-1 Yoshida, Yamaguchi, Yamaguchi 753-8512 Japan
[b]*Physics and Informatics, Faculty of Science, Yamaguchi University*
1677-1 Yoshida, Yamaguchi, Yamaguchi 753-8512 Japan
[c]*Department of Physical Science, Graduate School of Science, Hiroshima University*
1-3-1 Kagamiyama, Higashi-Hiroshima, Hiroshima 739-8526 Japan
[d]*Hiroshima Synchrotron Radiation Center, Hiroshima University*
2-313 Kagamiyam , Higashi-Hiroshima, Hiroshima 739-0046 Japan
[e]*SANKA High Technology Co. Ltd.,*
90-1 Kurimachi, Shingu-cho, Tatsuno-shi, Hyogo 678-5148 Japan
[f]*Laboratory of Advanced Science and Technology for Industry, University of Hyogo*
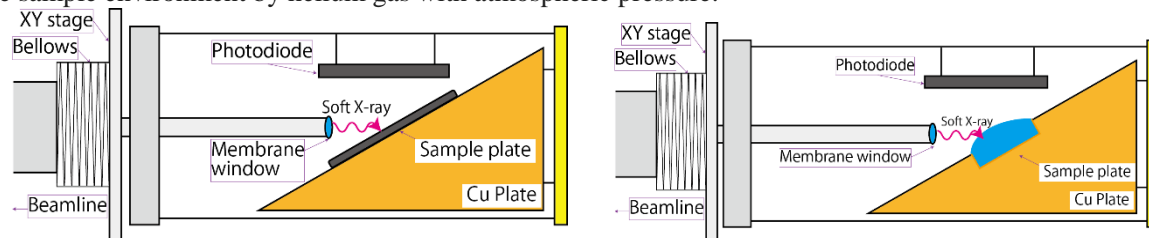*3-1-2 Koto, Kamigori-cho, Hyogo 678-1205 Japan*

1. Introduction

Soft X-ray absorption experiments are normally performed in a vacuum environment to avoid attenuation by air. It was generally considered that measurements of liquids by soft X-ray is difficult due to the attenuation. Recently, thin films with a thickness around 100 nm made of silicon nitride (Si_3N_4) or silicon carbide (SiC), which can be used as a window for soft X-ray transmission, are commercially available [1-2]. For example, we have developed an experimental apparatus in which a vacuum chamber and a liquid sample under atmospheric pressure were separated by the thin film window [1]. However, since thin films of window is fragile, there is a danger that the liquid samples flow into the vacuum chamber when the membrane window breaks. It is difficult to install liquid flow cells using thin film window in a normal soft X-ray beam line without cares for window break accidents. Therefore, we have developed a new apparatus for soft X-ray absorption experiments for liquids and solid with helium environment. In the helium gas environment, it is possible to arrange the sample away from the window surface since the attenuation length of the soft X-ray is longer by about 10 to 100 times than in the air [3]. Even if the window material breaks, only environment gas could flow into the vacuum chamber, and samples are stay on sample plate. Therefore newly designed apparatus requires much less cares for connecting it to the beamline.

2. Development of an apparatus

Fig. 1 is a schematic illustration of a apparatus for soft X-ray absorption experiments of solid and liquid samples under atmospheric helium gas environment. The left panel shows the apparatus for solid samples, and the right shows the apparatus for liquid samples. In this apparatus, we have used 100nm thick membrane window with 0.5mm×0.5mm opening made of silicon nitride on φ3mm silicon frame (NT050C, Norcade, Canada). In order to shorten the distance between the sample and window for reducing attenuation of soft X-rays, the membrane window was glued directly on the tip of a 3 mm diameter tube which was connected to the chamber of the end-station. For solids, the sample was mounted on the copper plate slope by a double sided adhesive carbon tape. For liquid samples, the sample was dropped on a pit of a copper plate and kept by surface tension. A photodiode sensitive in the soft X-ray region was also placed near sample to detect soft X-ray emission (fluorescence) caused by soft X-ray irradiation. Then finally, the

whole apparatus including a sample and the detector was covered with a vacuum piping so as to replace the sample environment by helium gas with atmospheric pressure.
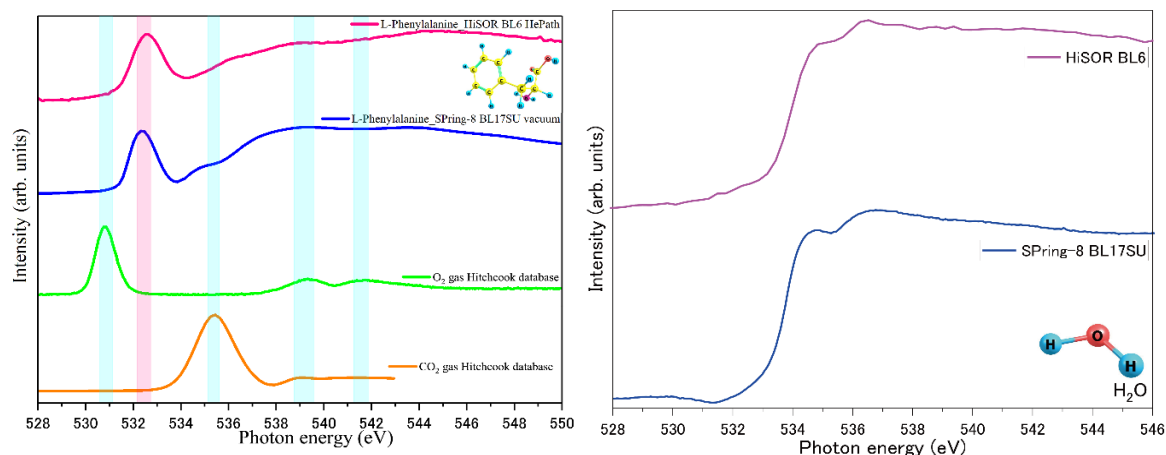

Fig. 1 Schematic illustration of sample apparatus including a membrane window, XY stage to adjust optical axis , a photodiode to detect fluorescence yield and a sample plate. The left panel is apparatus for solid samples and the right is apparatus for liquid samples.

3. Experiments

The developed apparatus was installed in the end station of the at HiSOR BL6 [4]. Soft X-ray absorption experiments were performed in oxygen K-edge of L-phenylalanine (powder) and H_2O under He gas environment. For the evaluation of this apparatus, we compared the spectra obtained at HiSOR BL6 with the spectra of same sample measured at BL17SU in SPring-8. We have also compare previously reported spectrum of oxygen and carbon dioxide gas to confirm whether the sample environment is sufficiently replaced with helium or not.

4. Results

Fig. 2 shows obtained spectra of L-phenylalanine (left panel) and H_2O (right panel) in O K-edge.

Fig. 2 The left panel shows absorption spectra of L-phenylalanine in O K-edge taken at HiSOR BL6 and SPring-8 B17SU. In lower part of the left panel, reference spectra of gas phase oxygen [5] and carbon dioxid [6] in O K-edge were plotted. The right panel shows absorption spectra of H_2O in O K-edge at HiSOR BL6 (top) and at SPring-8 B17SU (bottom).

Spectral shapes of the absorption spectra obtained at HiSOR BL6 are consistent with that obtained at SPring-8 BL17SU as shown in left panel of Fig. 2. In addition, there is no peaks assignable to peaks of oxygen and carbon dioxide in spectra of L-phenylalanine (top). Therefore, we conclude that the sample environment was successfully replaced with helium gas. The absorption spectra of liquid H_2O obtained at HiSOR BL6 is also consistent with the spectrum of SPring-8 BL17SU. According to these results, we conclude that the developed apparatus works fine for x-ray absorption measurements under He gas with atmospheric pressure.

REFERENCES

1. T. Tokushima et. al., Phys. Chem. Chem. Phys., 11(2009), 1679-1682.
2. M. Nagasaka and N. Kosugi, J. Vac. Soc. Jpn., Vol. 59, No. 11, 2016, 301-306.
3. Y. Tamenori, J. Vac. Soc. Jpn., Vol. 59, No. 12, 2016, 333-340.
4. H. Yoshida, Y. Senba, T. Goya et. al., J. Elec. Spectrosc. Relat. Phenom., 144-147 (2005) 1105.
5. Hitchcook Research Group   http://unicorn.mcmaster.ca/
6. B.X. Yang, et. al., Phys. Rev. A 36 (1987) 4298

Soft x-ray absorption measurement of hybrid organic-inorganic perovskite, a material for dye-sensitized solar panels, under atmospheric pressure He environment

Takashi Tokushima[a,b], Masahito Niibe[a], Sho Yokouchi[a], Yuka Horikawa[c], Yoshihi Nakao[c] and Hiroaki Yoshida[d,e]

[a] *Laboratory of advanced science and technology for industry, University of Hyogo, 3-1-2 Koto, Kamigori-cho, Ako-gun, Hyogo, JAPAN*
[b] *SANKA high technology Co. Ltd., 90-1 Kurimachi, Shingu-cho, Tatsuno-shi, Hyogo*
[c] *Physics and Informatics, Faculty of Science, Yamaguchi University, 1677-1 Yoshida, Yamaguchi, Yamaguchi*
[d] *Department of Physical Science, Graduate School of Science, Hiroshima University, 1-3-1 Kagamiyama, Higashi-Hiroshima, Hiroshima*
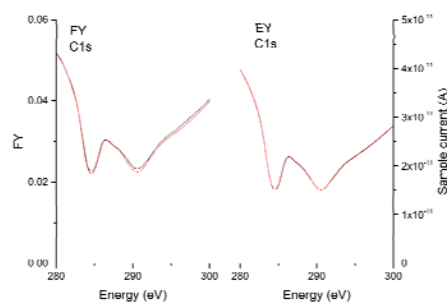[e] *Hiroshima Synchrotron Radiation Center, Hiroshima University, 2-313 Kagamiyama, Higashi-Hiroshima, Hiroshima*

Keywords: Soft x-rays, X-ray absorption, He environment.

Hybrid organic-inorganic perovskite is a candidate for a material for dye-sensitized solar panels [1]. However, these materials show degradation when exposed to humid atmospheres. Therefore, it is important to know electronic structure at realistic condition rather than under vacuum [2].

We have recently been developing helium path apparatus where air is replaced by He gas to improve transmission of soft x-rays. Because of strong K-edge absorption of nitrogen and oxygen, 5 mm of light path in air is enough to decay less than 1% in intensity for soft x-rays from N 1s absorption (around 400eV) above O 1s absorption (around 530eV). Owing to He path, transmission is expected to recover over 90%. This technique is well known and frequently used in experiments in hard x-ray region. However, applications using helium environments for soft x-ray region (around 100-1000eV) are still small in number. In our new apparatus, a commercially available silicon nitride membrane (Norcada Inc., Canada) made from Si wafer, which is around 100nm in thickness and have high transmission for soft x-rays, was used as a window to separate vacuum and He gas at atmospheric pressure.

FIGURE 1. FY intensity and sample current (EY) plot vs incident energy for C1s edge of $(CH_3NH_3)PbI_3$ (red lines) and PbI_3 (solid lines).

Figure 1 shows fluorescence intensity and sample current plot vs incident energy for C1s edge under atmospheric He gas. One can observe small differences between $(CH_3NH_3)PbI_3$ and PbI_3, however the difference is not enough to clarify electronic structure. It is required to improve signal to noise ratio. According to obtained energy profile of incident beam intensity, mirrors and gratings of the beamline might be contaminated by carbon. Hence cleaning of the optics is required for further experiments using C1s edge.

REFERENCES

1.   H Zhu, K.Miyata *et al.*, Science **353** (6306), pp.1409-1413(2016).
2.   J. Chun-Ren Ke, A. Walton *et al.*, *Chem. Commun.* **53** (37), pp. 5231–5234 (2017).

Electronic Structures and Impurity Cluster Features in Mg-Zn-Y Alloys with a Synchronized Long-Period Stacking Ordered Phase

Shinya Hosokawa[a], Kenji Maruyama[b], Kentaro Kobayashi[b],
Jens Rüdiger Stellhorn[a], Benedict Paulus[a], Akihide Koura[a], Fuyuki Shimojo[a],
Michiaki Yamasaki[c,d], Yoshihito Kawamura[c,d], Satoru Yoshioka[e], Hitoshi Sato[f]

[a]*Department of Physics, Kumamoto University, Kumamoto 860-8555, Japan*
[b]*Department of Chemistry, Niigata University, Niigata 950-2181, Japan*
[c]*Department of Materials Science, Kumamoto University, Kumamoto 860-8555, Japan*
[d]*Magnesium Research Center, Kumamoto University, Kumamoto 860-8555, Japan*
[e]*Department of Applied Quantum Physics and Nuclear Engineering, Kyushu University, Fukuoka 819-0395, Japan*
[f]*Hiroshima Synchrotron Radiation Center, Hiroshima University, Higashi-Hiroshima 739-0046, Japan*

In the recent fifteen years, novel Mg-based alloys with microstructures forming a long-period stacking ordered (LPSO) structure, the so-called KUMADAI Magnesium [1], have achieved much attention due to the potential for widespread applications as structural materials because these alloys are light-weighted rather than Al. By adding a small amount of Zn and rare-earth (Y or Gd) impurities, the soft and flammable Mg metal turns to much strong and non-flammable with high thermal stability. Because of such excellent properties together with the ease of recycling, these Mg alloys are expected as next-generation structural materials for, e.g., bodies of subways or even aircrafts.
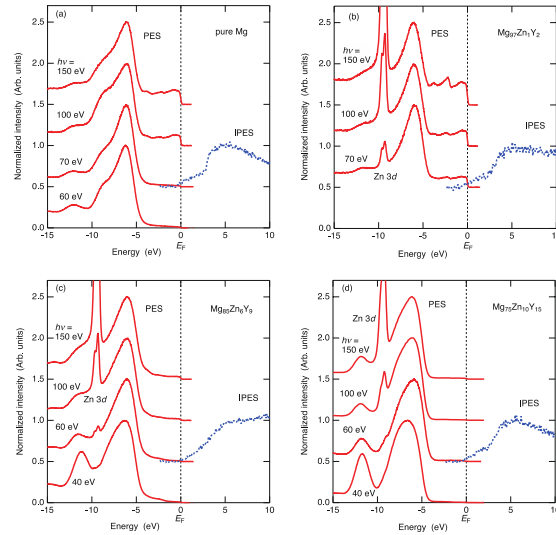
According to an atomic-resolution angle annular dark field scanning transmission electron microscope observations by Abe et al. [2], it was found that the Zn and Y impurities are enriched around the stacking faults, and thus, this curious structure is referred to as the synchronized LPSO phase. The existence of $L1_2$-type clusters formed by the impurities in the Mg-Zn-Y alloys was proposed by Egusa and Abe [3], which were composed of Zn_6Y_8 and embedded in the stacking faults.

From the structural point of view, the overall features of the $L1_2$ clusters are well described as cited in Ref. [3]. However, the electronic structures should be clarified for the understandings of the electronic properties and the chemical natures of the Zn/Y impurities, which may be highly influenced for the stability of the $L1_2$ clusters in the Mg LPSO alloys. We have recently investigated the valence- and conduction-band electronic structures of $Mg_{97}Zn_1Y_2$, $Mg_{85}Zn_6Y_9$, and $Mg_{75}Zn_{10}Y_{15}$ polycrystalline alloys together with pure α-Mg by measuring photoemission and inverse-photoemission spectroscopies (PES and IPES), respectively. Here, the $Mg_{97}Zn_1Y_2$ and $Mg_{85}Zn_6Y_9$ alloys have 18R type LPSO structures and the $Mg_{75}Zn_{10}Y_{15}$ alloy has a 10H type after the Ramsdell notation with the volume fractions of the LPSO phase up to ~24%, ~100%, and ~100%, respectively. The core levels of the constituent elements were also studied using core-level PES to examine the chemical natures of the elements. From these results, we found clear heterogeneous indications concerning the $L1_2$ clusters.

The cast ingots of the samples were prepared using high frequency induction melting of pure Mg (99.99 wt.%), Zn (99.9 wt.%), and Y (99.9 wt.%) metals in a cylindrical carbon crucible in a pure Ar atmosphere. The ingots were cut to be a rectangle plate with a size of $3 \times 3 \times 1$ mm^3. The PES spectra were measured using a spectrometer installed at BL-7 of HSRC. The IPES spectra were obtained using the RIPES spectrometer at HSRC. All of the measurements were performed at room temperature.
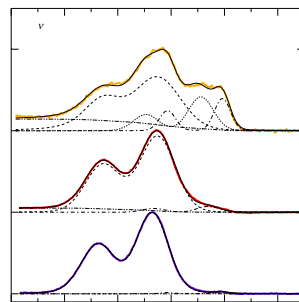
Figure 1 shows the PES and IPES spectra of (a) pure Mg, (b) $Mg_{97}Zn_1Y_2$, (c) $Mg_{85}Zn_6Y_9$, and (d) $Mg_{75}Zn_{10}Y_{15}$. The magnitudes of the PES spectra are normalized to the maximum values at about -6 eV, and the IPES spectra were normalized so that the intensities show 0.5 at 5 eV. With increasing the impurity

fraction, the Zn $3d$ core-level peaks appear, and show high incident photon energy, $h\nu$, dependence. The impurity fraction dependence in the magnitude of the Zn $3d$ peak is unusual, indicating that this signal may originate from the Zn atoms in the Mg host, and not in the Zn_6Y_8 clusters or their fragments. Small spectral changes are observed in the PES spectra, a small shoulder at about -7.8 eV and a large peak at about -12.0 eV. The IPES spectra show large impurity effects in the slope at about 3 eV and the tail beyond 5 eV.

FIGURE 1. The valence-band PES and conduction-band IPES spectra of (a) pure α-Mg, (b) $Mg_{97}Zn_1Y_2$, (c) $Mg_{85}Zn_6Y_9$, and (d) $Mg_{75}Zn_{10}Y_{15}$ polycrystals indicated by the solid and dashed curves, respectively.

The thick solid curves in Fig. 2 show the Y $3d$ core-level PES spectra of the $Mg_{97}Zn_1Y_2$, $Mg_{85}Zn_6Y_9$, and $Mg_{75}Zn_{10}Y_{15}$ alloys from top to bottom measured at $h\nu$ = 230 eV with the energy resolution of 0.23 eV. The intensities are reduced by the Y $3d_{5/2}$ peak height with respect to the background at the shallower energy of -153 eV. For the $Mg_{85}Zn_6Y_9$, and $Mg_{75}Zn_{10}Y_{15}$ alloys, mostly one doublet is observed, which may originate from the Y atoms in the Zn_6Y_8 clusters. On the other hand, the spectrum of $Mg_{97}Zn_1Y_2$ has at least three doublets, suggesting that the Y atoms in this alloy exhibit different chemical natures. The spectrum was fitted using three doublets, and the results are given by the dashed, dotted, and chain curves. The largest one is located at the same energy of others, confirming that mostly a half of the Y atoms may belong to the Zn_6Y_8 clusters, and other two may indicate that the Y atoms are located alone in the host Mg or in fragments of the $L1_2$ clusters. Detailed analysis is now in progress.

FIGURE 2. Y $3d$ core-level PES spectra measured at $h\nu$ = 230 eV. The spectra are fitted with at most three pairs of the Y $3d_{5/2}$ and $3d_{3/2}$ core electrons (the dashed, dotted, and chain curves) and the background (the two-dot chain curve).

REFERENCES

1. Y. Kawamura et al., *Mater. Trans.* **42**, 1172-1176 (2001).
2. E. Abe et al., *Philos. Mag. Lett.* **91**, 690-696 (2011).
3. D. Egusa and E. Abe, Acta Mater. **60**, 166-178 (2012).

The seeds of Zn_6Y_8 L1$_2$-type clusters in amorphous $Mg_{85}Zn_6Y_9$ alloy investigated by photoemission spectroscopy

Shinya Hosokawa[a], Jens Rüdiger Stellhorn[a], Benedict Paulus[a],
Kenji Maruyama[b], Kentaro Kobayashi[b], Hiroshi Okuda[c], Michiaki Yamasaki[d,e],
Yoshihito Kawamura[d,e], Hitoshi Sato[f]

[a]*Department of Physics, Kumamoto University, Kumamoto 860-8555, Japan*
[b]*Department of Chemistry, Niigata University, Niigata 950-2181, Japan*
[c]*Department of Materials Science and Engineering, Kyoto University, Kyoto 606-8501, Japan*
[d]*Department of Materials Science, Kumamoto University, Kumamoto 860-8555, Japan*
[e]*Magnesium Research Center, Kumamoto University, Kumamoto 860-8555, Japan*
[f]*Hiroshima Synchrotron Radiation Center, Hiroshima University, Higashi-Hiroshima 739-0046, Japan*

In the recent fifteen years, novel Mg-based alloys with microstructures forming a long-period stacking ordered (LPSO) structure, the so-called KUMADAI Magnesium [1], have achieved much attention due to the potential for widespread applications as structural materials because these alloys are light-weighted rather than Al. By adding a small amount of Zn and rare-earth (Y or Gd) impurities, the soft and flammable Mg metal turns to much strong and non-flammable with high thermal stability. Because of such excellent properties together with the ease of recycling, these Mg alloys are expected as next-generation structural materials for, e.g., bodies of subways or even aircrafts.

According to an atomic-resolution angle annular dark field scanning transmission electron microscope observations by Abe et al. [2], it was found that the Zn and Y impurities are enriched around the stacking faults, and thus, this curious structure is referred to as the synchronized LPSO phase. The existence of L1$_2$-type clusters formed by the impurities in the Mg-Zn-Y alloys was proposed by Egusa and Abe [3], which were composed of Zn_6Y_8 and embedded in the stacking faults.
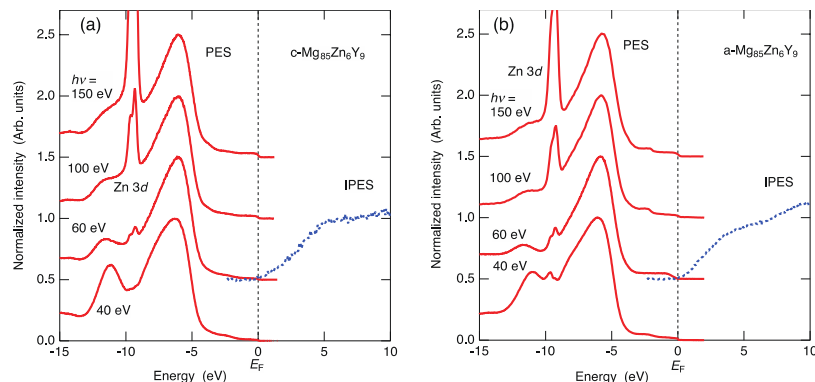
Recently, Okuda et al. [4] investigated the transformation process of amorphous-to-crystal in $Mg_{85}Zn_6Y_9$ LPSO alloy using small angle x-ray scattering. They found a novel hierarchical phase transformation that the clustering of the impurity atoms occurs first, and the spatial rearrangement of the clusters induces a secondary transformation leading to two-dimensional ordering of the clusters. From their results, we expect that the seeds of impurity clusters are already implanted even in the amorphous phase.

The electronic structures will give valuable hints for the understandings of the electronic properties and chemical natures of the Zn/Y impurities in the amorphous and crystalline Mg LPSO alloys, which may be highly influenced for the stability of the L1$_2$ clusters. We have recently investigated the valence- and conduction-band electronic structures of amorphous and crystalline $Mg_{85}Zn_6Y_9$ alloys by measuring photoemission and inverse-photoemission spectroscopies (PES and IPES), respectively. The core-levels were also studied using core-level PES to examine the chemical natures of the constituent elements. From these results, we found clear heterogeneous indications concerning the Zn_6Y_8 L1$_2$ clusters.

An amorphous sample was manufactured at Magnesium Research Center, Kumamoto University by a normal melt-spinning technique. The amorphous phase of the obtained ribbons was examined by x-ray diffraction and transmission electron microscopy. The composition of the sample was confirmed to be nominal value within 1 at.% by an electron-probe micro-analysis equipment. The PES spectra were measured using a spectrometer installed at BL-7 of HSRC. The IPES spectra were obtained using the RIPES spectrometer at HSRC. All of the measurements were performed at room temperature.
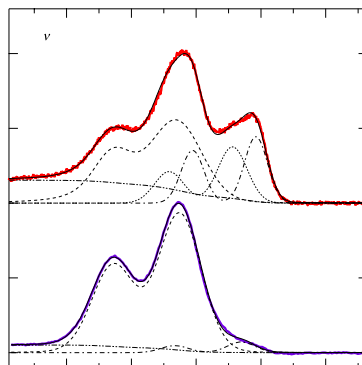
Figure 1 shows the PES and IPES spectra of (a) crystalline and (b) amorphous $Mg_{85}Zn_6Y_9$ alloys. The magnitudes of the PES spectra are normalized to the maximum values at about -6 eV, and the IPES spectra

were normalized so that the intensities show 0.5 at 5 eV. The spectral features of the both phases look very similar to each other.

FIGURE 1. The valence-band PES and conduction-band IPES spectra of (a) crystalline and (b) amorphous $Mg_{85}Zn_6Y_9$ indicated by the solid and dashed curves, respectively.

The thick solid curves in Fig. 2 show the Y $3d$ core-level PES spectra of amorphous (upper) and crystalline (lower) $Mg_{85}Zn_6Y_9$ alloys measured at the incident photon energy $h\nu = 230$ eV with the energy resolution of 0.23 eV. The intensities are reduced by the Y $3d_{5/2}$ peak height with respect to the background at the shallower energy of -153 eV. For the crystalline phase, mostly one doublet is observed, which may originate from the Y atoms in the Zn_6Y_8 clusters. On the other hand, the spectrum of the amorphous phase has at least three doublets, suggesting that the Y atoms in this amorphous alloy exhibit different chemical natures.

FIGURE 2. Y $3d$ core-level PES spectra measured at $h\nu = 230$ eV. The spectra are fitted with at most three pairs of the Y $3d_{5/2}$ and $3d_{3/2}$ core electrons (the dashed, dotted, and chain curves) and the background (the two-dot chain curve).

The spectrum was fitted using three doublets, and the results are given by dashed, dotted, and chain curves. The largest contribution is located at the same energy of that of the crystalline phase, confirming that mostly a half of the Y atoms may belong to the Zn_6Y_8 clusters, and other two indicate that the Y atoms are located alone in the host Mg or in fragments of the $L1_2$ clusters. Detailed analysis is now in progress.

REFERENCES

1. Y. Kawamura et al., *Mater. Trans.* **42**, 1172-1176 (2001).
2. E. Abe et al., *Philos. Mag. Lett*. **91**, 690-696 (2011).
3. D. Egusa and E. Abe, Acta Mater. **60**, 166-178 (2012).
4. H. Okuda et al., *Sci. Rep.* **5**, 14186-1-6 (2015).

Photoemission Study of Sr-Cu-O Compounds With Multi CuO$_2$ Layer

S. Tsuda[a], H. Yamaoka[b], H. Sakurai[c], H. Sato[d], and K. Shimada[d]

[a]National Institute for Materials Science 3-13 Sakura, Tsukuba 305-0003, Japan
[b]RIKEN SPring-8 Center, Sayo, Hyogo 679-5148, Japan
[c]National Institute for Materials Science 1-1 Namiki, Tsukuba 305-0044, Japan
[d]Hiroshima Synchrotron Radiation Center, Hiroshima University, Higashi-Hiroshima, Hiroshima 739-0046, Japan

Keywords: Photoemission spectroscopy, transition metal oxides

After the pioneer work by Dr. Matsuno[1], there had been no report on the systematic study of electronic structure of layered Perovskite compounds of 3d transition metal oxides. While the former study is on thin films, recently high quality bulk samples are available [2,3]. In this study, we performed photoemission measurements of bulk Sr$_2$MO$_4$ with M = V(3d^1), Cr(3d^2), Mn(3d^3) and Sr$_{n+1}$Cr$_n$O$_{3n+1}$ with n= 1, 2, 3 at BL-07 in HiSOR.

Figure 1 shows valence band photoemission spectra of Sr$_2$MO$_4$ (M = V, Cr, Mn) obtained by hν = 60 eV. Those spectra contains mainly two components ; (A) huge peak around -5 eV mostly due to O 2p (B) relatively small but finite humps below -3 eV probably due to 3d (and lower Hubbard) bands. With increasing the 3d electron number, the intensity (B) increases.
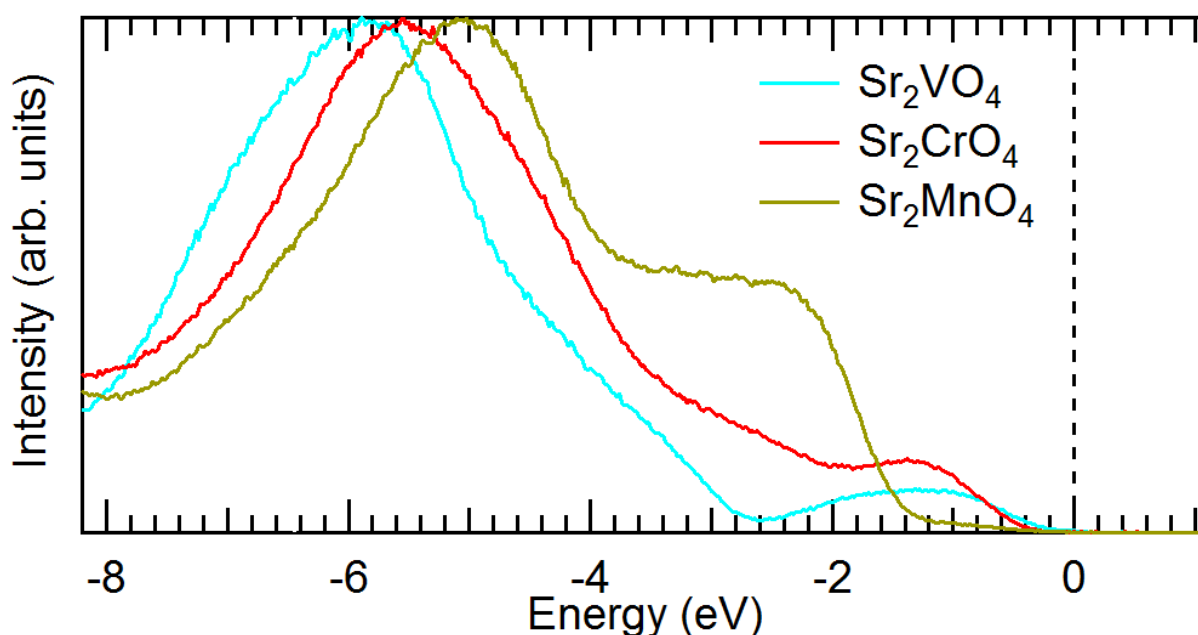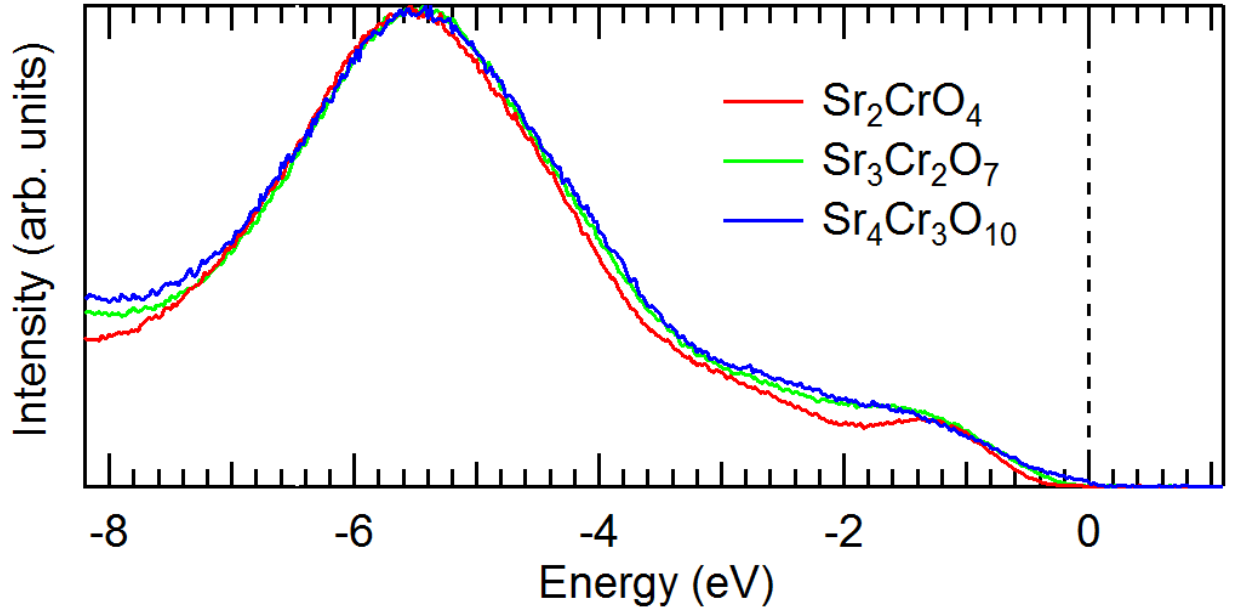

FIGURE 1. Valence band photoemission spectra of Sr$_2$MO$_4$ (M = V, Cr, Mn) obtained by hν = 60 eV.

FIGURE 2. Valence band photoemission spectra of $Sr_{n+1}Cr_nO_{3n+1}$ (n= 1~3) obtained by hν = 60 eV.

Figure 2 shows valence band spectra of $Sr_{n+1}Cr_nO_{3n+1}$ (n= 1~3) obtained by hν = 60 eV. With increasing the n (the number of the CrO_2 layer), the humps around -1.2 eV are broadened and the intensity at Fermi level is increased. The increase of the n corresponds to the increase of the dimensionality (from 2 dimensional to 3 dimensional). In the limit of n -> ∞, $Sr_{n+1}Cr_nO_{3n+1}$ becomes $SrVO_3$, which is known as a correlated metal. This trend is consistent with our results

A first principle calculation [4] predicts that Sr_2CrO_4 shows negative charge transfer ($\Delta < 0$). Now we are trying to evaluate physical parameters such as U and Δ within cluster model.

REFERENCES

1. J. Matsuno *et al.*, *Phys. Rev. Lett.* **95**, 176404 (2005).
2. H. Sakurai, *Physics Procedia* **75**, 829 (2015).
3. H. Sakurai, *J. Phys. Soc. Jpn.* **83**, 123701 (2014).
4. T. Ishikawa *et al.*, *J. Phys. Soc. Jpn.* **86**, 033701 (2017).

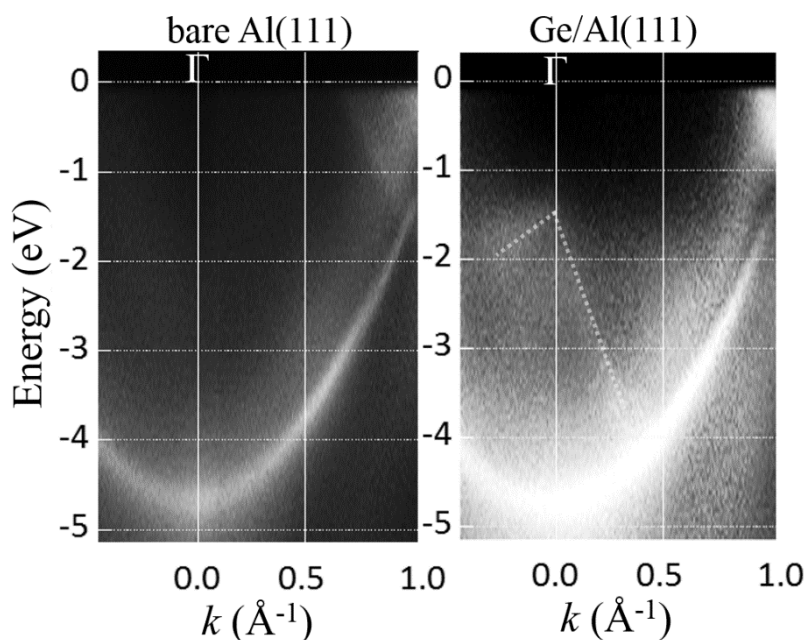# Elucidation of Electronic Band Structure of Monolayer Germanium Film

Osamu Kubo[a], Satoshi Endo[a], Hitoshi Sato[b] and Taichi Okuda[b]

[a]Graduate School of Engineering, Osaka University,
2-1 Yamadaoka, Suita, Osaka 565-0871, Japan
[b]HiSOR, Hiroshima University,
2-313 Kagamiyama, Higashi Hiroshima, Hiroshima 739-0046, Japan

Keywords: germanene, ARPES

Monolayer sheets of group IV materials such as Si and Ge were also predicted to have Dirac cone analogous to graphene. They are composed of buckled honeycomb structure which is predicted to introduce very curious physical properties, such as quantum-spin Hall effect and tunable band gap by external electric field [1,2]. These properties are more likely to be able to observe in germanene as compared with silicene owing to its relatively large spin-orbit coupling [2]. Currently, formation of germanene has been reported mainly on metal substrates such as Au(111), Pt(111), Al(111), and so forth. [3-5]. However, it is still controversial whether the reported germanenes have Dirac cone. We have recently reported that germanene is formed on Al(111) surface with a periodicity of Al(111)$\sqrt{7}\times\sqrt{7}$ [6], which is different from the previously reported 3×3 phase [4]. However, the electronic band structures of both $\sqrt{7}\times\sqrt{7}$ and 3×3 phases have not yet been reported. Thus, we have studied on the electronic band structure of the germanene with $\sqrt{7}\times\sqrt{7}$ phase measured using angle-resolved photo emission spectroscopy.

FIGURE 1. Band dispersions for clean Al(111) along Γ-K direction of Al(111) brillouin zone obtained by ARPES.

Figure 1(a) shows the band dispersion for a clean Al(111) obtained along Γ-K direction of Al(111) brillouin zone. The band dispersion after germanene formation is show in Fig. 1(b), in which two linear bands crossing at Γ point are seen. We then calculated the band dispersions along the same direction as the spectra shown in Fig. 1 by using DFT. The atomic structure of germanene reported in ref. 6 is

adopted in the calculation. From the DFT calculation, it is suggested that the newly formed bands are caused by subsurface Al layers rather than by top germanene layer.

REFERENCES

1. C.-C. Liu, et al., Phys. Rev. Lett. 107, 076802 (2011).
2. M. Ezawa, New J. Phys. 14, 033003 (2012).
3. M. E. Dávila, et al., New J. Phys. 16, 095002 (2014).
4. M. Derivaz, et al., Nano Lett. 15, 2510 (2015).
5. L. Li, et al., Adv. Mater. 26, 8420 (2014).
6. S. Endo, et al., Appl. Phys. Express 11, 015502 (2018).

Photoelectron Spectroscopy of Thin-film Beta Tungsten

H.T. Lee[a], H. Yamaoka[b], A. Nagakubo[a] and H. Sato[c]

[a]*Graduate School of Engineering, Osaka University, Suita 565-0871, Japan*
[b]*RIKEN SPring-8 Center, Hyogo 679-5148, Japan*
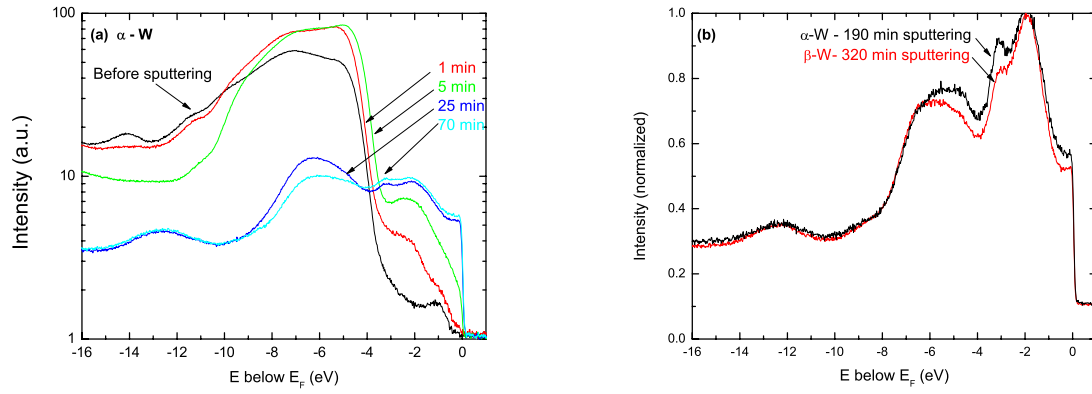[c]*Hiroshima Synchrotron Radiation Center, Hiroshima University, Higashi-Hiroshima 739-0046, Japan*

Tungsten (W) is a refractory metal ranging in applications such as armor material in magnetic fusion devices or as replacement of copper metallic interconnects in microelectronics. In such applications, the bcc cubic crystal structure α-W is used. An alternative A15 structure, β-W, is meta-stable and is considered for use in spintronic devices. Spintronic devices utilize both the charge and the spin of electrons and have the potential to overcome issues facing conventional semiconductor electronics. The transfer efficiency of the charge-to-spin current is defined by the spin-Hall angle which is ~0.3 for β-W in comparison to <0.07 for α-W at 300 K. Many studies have examined the magnitude of the spin Hall angle as a function of W structure, but to date, hardly any experimental measurements of the electronic states of β-W have been reported.

The reason for the large magnitude of the spin Hall angle in β-W is presently not known. The spin Hall effect can arise: (1) extrinsically, such as asymmetric scattering for spin-up and spin-down electrons from impurities, or (2) intrinsically, where spin imbalance occur as a result of the band structure even in the absence of scattering. Recently, first principle calculations have shown that the spin Hall angle of the transition metals like W depends on the electron filling of the *d*-orbitals (i.e. band structure related) suggesting spin Hall effect arises from intrinsic properties [1]. Clarifying whether the spin Hall effect arises from extrinsic or intrinsic properties is the first step in understanding and thus controlling the spin Hall effect in β-W. The experimental goal was thus to characterize the electron density of states of deposited β-W films by measuring high-resolution valence band spectra near the Fermi level and making comparison to reference α-W.
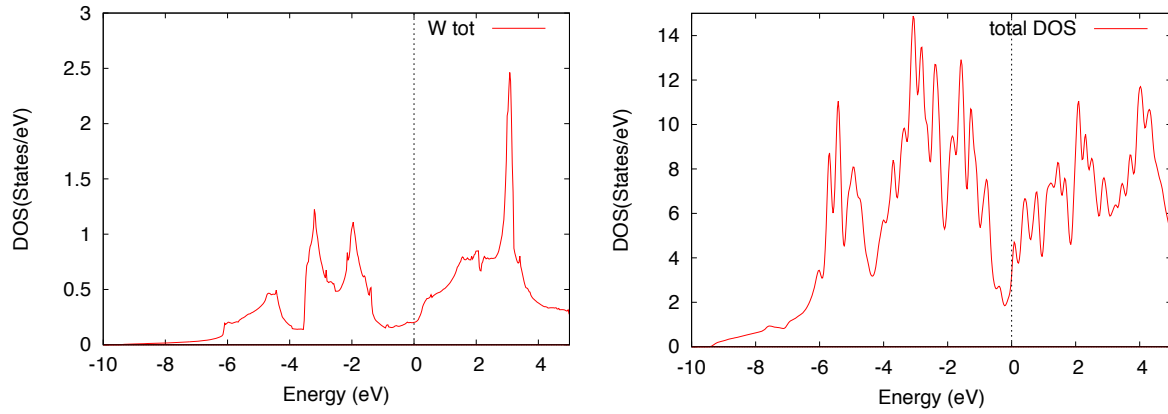
Thin (~50 nm) α-W and β-W films on silicon substrates were produced using physical vapor deposition technique. The mechanical and structural properties were characterized using a combination of X-ray diffraction and picosecond ultrasonic measurements [2]. The elastic constants of pure α-W and β-W were 5–10% lower than the reported bulk values for α-W. The calculated elastic constants using density functional theory agreed within 10% of the experimental values.

Figure 1(a) shows the photoelectron spectroscopy (PES) results of α-W film as function of in-vacuo Ar sputtering time. The tungsten oxide layer formed due to air transport is sputtered away following approximately 25 minutes of Ar sputtering (1 keV). Figure 1(b) compares the photoelectron spectrum between α-W and β-W samples. Fine difference in the structure between -2 and -4 eV is observed. Specifically, α-W clearly shows a double peak structure, which is less prominent in β-W. Figure 2 shows preliminary results of calculated valence bands for α-W and β-W, respectively. The calculations are qualitatively similar to the experimental results with the α-W exhibiting a sharp two-peak structure between -2 and -4 eV, which is less prominent in β-W. However, such comparisons in peak magnitudes are complicated by the fact that there is an additional broad peak observed between -4 and -6 eV in experiments. This signal continuously decreases with increasing sputtering time as illustrated in both Figures 1(a) and (b) - suggesting partial contribution from oxygen contamination. While calculations also show a peak between -4 and -6 eV, it is not possible at this stage to associate such structure entirely to W due to the possible oxygen contamination. Future work performed on bulk high purity W samples are planned to clarify this effect. These experiments lay the groundwork in performing PES on thin magnetic multilayered β-W films (e.g. W-Mn) and further analysis of the data should provide insight into the spin orbit interaction difference in α-W and

β-W which is responsible for the spin hall and inverse spin hall effect.

FIGURE 1. Photoemission spectra for (a) α-W as function of Ar sputtering time, and (b) comparison of α-W and β-W samples showing the difference in peak structure between -2 and -4 eV.

FIGURE 2. Calculated valence band spectra of α-W and β-W samples, respectively.

REFERENCES

1. T. Tanaka, H. Kontani, M. Naito, T. Naito, D. S. Hirashima, K. Yamada, and J. Inoue, Phys. Rev. B 77, 165117 (2008).
2. A. Nagakubo et al., "Elastic constant of alpha and beta tungsten films studied by picosecond ultrasonics" USE2017
https://www.use-jp.org/proceedings/USE17/pdf/1P1-9.pdf

Angle-resolved photoemission study of WTe₂

R. Matsumoto[a], T. Sugimoto[a], T. Mizokawa[a], N. L. Saini[b], M. Arita[c],
H. Namatame[c], M. Taniguchi[c], R. Jha[d], R. Higashinaka[d], T. D. Matsuda[d],
and Y. Aoki[d]

[a]*Department of Applied Physics, Waseda University, Shinjuku, Tokyo 169-8555, Japan*
[b]*Department of Physics, University of Roma "La Sapienza", 00185 Roma, Italy*
[c] *HiSOR, Hiroshima University, Higashi-hiroshima, Hiroshima 739-0046, Japan*
[d] *Department of Physics, Tokyo Metropolitan University, Hachioji 192-0397, Japan*

INTRODUCTION

  Various narrow gap semiconductors and semimetals possessing band structure with non-trivial topological number have been attracting great interest due to their spin textured surfaces states which can be applied for the future spintronics devices [1-8]. In addition, the coexistence of electron and hole carriers can provide dramatic transport properties such as non-saturating magnetoresistance [9-16]. Among the semimetals with non-saturating magnetoresistance, electronic structure of WTe₂ has been studied in detail by means of angle-resolved photoemission spectroscopy (ARPES) [17-19]. A pair of electron pockets and hole pockets were reported in refs. 17 and 18 whereas five hole pockets and four electron pockets were identified in ref. 19. It is difficult to reconcile the three different ARPES results by chemical potential shift alone. The authors of ref. 19 pointed out that the number of Fermi surfaces is very sensitive to atomic position and the observed nine Fermi surfaces would be explained by calculation with some atomic arrangement. However, the band dispersions near the Fermi level reported in the three ARPES works largely deviate from band structure calculations which cannot be explained by adjusting atomic position. In this content, it is interesting and important to examine the band dispersion considering their orbital character and to reconsider the assignment of Fermi surfaces.
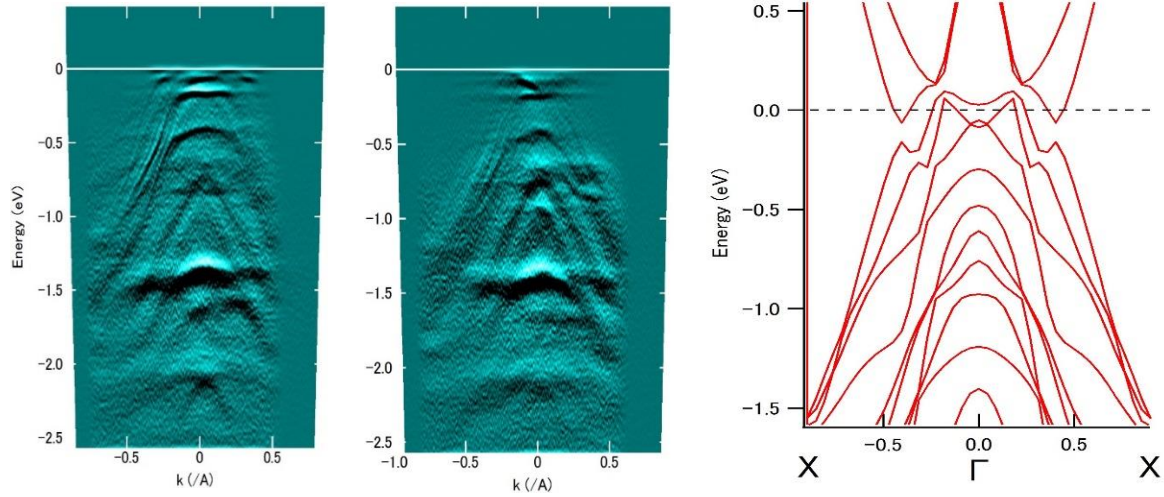
EXPERIMENTAL

   ARPES measurements were performed at beamline 9A of Hiroshima Synchrotron Radiation Center(HiSOR). The base pressure of the spectrometer of HiSOR BL-9A was in the 10^{-9} Pa range. The crystals were cleaved at 300 K under the ultrahigh vacuum and then cooled to 20 K for the ARPES measurements. The ARPES data were obtained within 12 hours after the cleavage. The total energy resolution was set to about 15 meV for excitation energies of 22.9-33.9 eV in order to observe the valence band top near the zone cernter (Γ or Z point). Binding energies were calibrated using the Fermi edge of gold reference samples.

RESULTS & DISCUSSION

  Figure 1 shows band maps near the zone center constructed from second derivatives of energy distribution curves. The observed band dispersions are compared with the band-structure calculation indicated in the right panel of Fig. 1. At photon energy of 22.9 eV, one hole pocket at the zone center and two electron pockets around $k \sim$ -0.3 and 0.3 Å^{-1} are observed as predicted by the calculation. Their observed positions are much closer to the zone center than the calculated positions. In addition, the hole band at the zone center is very flat compared to the calculation. The photon energy dependence of the hole band excludes possibility of surface states. Therefore, the poor agreement between the experiment and theory can be assigned to correlation effect between W $5d$ holes and electrons near the Fermi level. The present results suggest that electron-hole correlation effect or excitonic correlation should be taken into account for understanding of transport properties of WTe₂.

FIGURE 1. Band maps near the zone center of WTe$_2$ taken at photon energies of 22.9 eV (left) and 25.9 eV (middle). The right panel shows band structure calculation around Γ pioint.

CONCLUSION

In conclusion, we have studied the electronic structure of WTe$_2$ by means of angle-resolved photoemission spectroscopy and band structure calculation. The valence band top reaches the Fermi level and forms a complicated hole pocket around the zone center. In addition, two electron pockets are observed besides the hole pocket which are modified from the prediction of band calculation. The disagreement between the experiment and theory indicates importance of electron-hole correlation in WTe$_2$.

REFERENCES

1 D. Hsieh, Y. Xia, L. Wray, D. Qian, A. Pal, J. H. Dil, J. Osterwalder, F. Meier, G. Bihlmayer, C. L. Kane, Y. S. Hor, R. J. Cava, and M. Z. Hasan, Science 323, 919 (2009).

2 D. Hsieh, Y. Xia, D. Qian, L. Wray, J. H. Dil, F. Meier, J. Osterwalder, L. Patthey, J. G. Checkelsky, N. P. Ong, A. V. Fedorov, H. Lin, A. Bansil, D. Grauer, Y. S. Hor, R. J. Cava, and M. Z. Hasan, Nature 460, 1101 (2009).

3 C. Jozwiak, Y. L. Chen, A. V. Fedorov, J. G. Analytis, C. R. Rotundu, A. K. Schmid, J. D. Denlinger, Y.-D. Chuang, D.-H. Lee, I. R. Fisher, R. J. Birgeneau, Z.-X. Shen, Z. Hussain, and A. Lanzara, Phys. Rev. B 84, 165113 (2011).

4 Z.-H. Pan, E. Vescovo, A. V. Fedorov, G. D. Gu, and T. Valla, Phys. Rev. B 88, 041101(R) (2013).

5 B. Yan, B. Stadtmuller, N. Haag, S. Jakobs, J. Seidel, D. Jungkenn, S. Mathias, M. Cinchetti, M. Aeschlimann, and C. Felser, Nat. Commun. 6, 10167 (2015).

6 Peng Zhang, J.-Z. Ma, Y. Ishida, L.-X. Zhao, Q.-N. Xu, B.-Q. Lv, K. Yaji, G.-F. Chen, H.-M. Weng, X. Dai, Z. Fang, X.-Q. Chen, L. Fu, T. Qian, H. Ding, and S. Shin, Phys. Rev. Lett. 118, 046802 (2017).

7 B. Q. Lv et al., Phys. Rev. Lett. 115, 217601 (2015).

8 S. Y. Xu et al., Phys. Rev. Lett. 116, 096801 (2016).

9 R. Xu, A. Husmann, T. F. Rosenbaum, M.-L. Saboungi, J. E. Enderby, and P. B. Littlewood, Nature 390, 57 (1997).

10 M. Lee, T. F. Rosenbaum, M.-L. Saboungi, and H. S. Schnyders,Phys. Rev. Lett.88, 066602 (2002).

11 F. Y. Yang, K. Liu, K. Hong, D. H. Reich, P. C. Searson, and C. L. Chein, Science 284, 1335 (1999).

12 F. Y. Yang, K. Liu, K. Hong, D. H. Reich, P. C. Searson, C. L. Chien, Y. Leprince-Wang, K. Yu-Zhang, and K. Han, Phys. Rev. B 61, 6631 (2000).

13 D.-X. Qu, Y. S. Hor, J. Xiong, R. J. Cava, and N. P. Ong, Science 329, 821 (2010).

14 T. Liang, Q. Gibson, M. N. Ali, M. Liu, R. J. Cava, and N. P. Ong, Nat. Mater.14, 280 (2015).

15 M. N. Ali, J. Xiong, S. Flynn, J. Tao, Q. D. Gibson, L. M. Schoop, T. Liang, N. Haldolaarachchige, M. Hirschberger, N. P. Ong, and R. J. Cava, Nature 514, 205 (2014).

16 K. Wang, D. Graf, L. Li, L. Wang, and C. Petrovic, Sci. Rep. 4, 7328 (2014).

17 I. Pletikosić, Mazhar N. Ali, A. V. Fedorov, R. J. Cava, and T. Valla, Phys. Rev. Lett. 113,216601 (2014).

18 J. Jiang, F. Tang, X. C. Pan, H. M. Liu, X. H. Niu, Y. X. Wang, D. F. Xu, H. F. Yang, B. P. Xie, F. Q. Song, P. Dudin, T. K. Kim, M. Hoesch, P. Kumar Das, I. Vobornik, X. G. Wan, and D. L. Feng, Phys. Rev. Lett. 115,166601 (2015).

19 Y. Wu , N. H. Jo, M. Ochi, L. Huang, D. Mou, S. L. Bud'ko, P. C. Canfield, N. Trivedi, R. Arita, and A. Kaminski, Phys. Rev. Lett. 115,166602 (2015).

Angle-Resolved Photoemission Study
of SnSe and Na-doped SnSe

M. Maeda[a], S. Suzuki[a], K. Yamamoto[a], T. Mizokawa[a], N. L. Saini[b], M. Arita[c],
H. Namatame[c], M. Taniguchi[c], G. Tan[d], L. D. Zhao[d], and M. G. Kanatzidis[d]

[a] Department of Applied Physics, Waseda University, Shinjuku, Tokyo 169-8555, Japan
[b] Department of Physics, University of Roma "La Sapienza", 00185 Roma, Italy
[c] Hiroshima Synchrotron Radiation Center, Hiroshima University,
Higashi-hiroshima, Hiroshima 739-0046, Japan
[d] Department of Chemistry, Northwestern University, Evanston, IL 60208, USA

Keywords: ARPES, doped semiconductor, thermoelectric material, Seebeck coefficient

INTRODUCTION

The recent discovery of ultrahigh thermoelectric performance in hole-doped SnSe has shown that band engineered SnSe is one of the key materials for the future thermoelectric devices [1]. The performace is determined by the dimensionless figure of merit ZT:

$$ZT = \frac{S^2 \sigma}{\kappa} T$$

where S, σ, κ and T are the Seebeck coefficient, the electrical conductivity, the thermal conductivity and the temperature. SnSe has a layered structure constructed with strong bonds along the b-c plane and weak bonds along the a-axis as shown in Figure 1(a) [2]. SnSe commonly exhibit high thermoelectric performance with the large Seebeck coefficient due to the multiple valence band maxima [4]. The Seebeck effect of SnSe is enhanced by the smaller energy separation between the multiple valence band maxima [5]. Although band structure calculations on SnSe are consistent with the transport properties [6-9], it is rather difficult to estimate the effect of Na doping from the theoretical calculation. The Na doping is expected to introduce atomic and electronic disorder to the system in a complicated manner which should be studied using spectroscopic experiments.
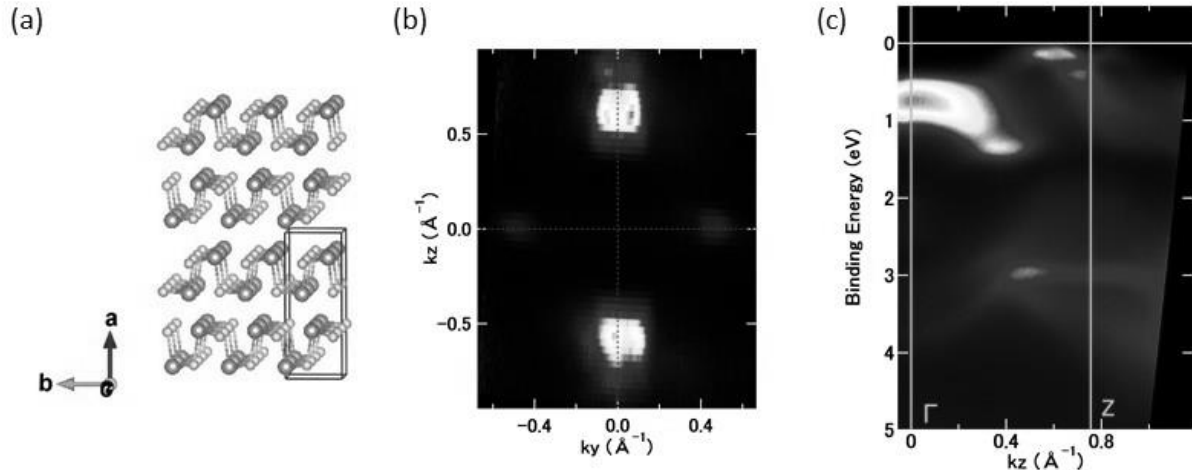
EXPERIMENTE

Single crystals of SnSe and $Sn_{0.985}Na_{0.015}Se$ were grown as reported in the literature [1]. ARPES measurements were done at beamline 9A of HiSOR. The crystals were cleaved at 300 K under the ultrahigh vacuum of 10^{-9} Pa range and then gradually cooled to 20 K for the ARPES measurements at various temperatures. The ARPES data were obtained within 12 hours after the cleavage. The excitation energy was set to 22.8 eV in order to observe the valence band top of the surface including Γ point. Binding energies were calibrated using the Fermi edge of gold reference samples. The total energy resolution was 22 meV.

RESULTS & DISCUSSION

In the ARPES measurement for Na-doped SnSe, multi hole pockets are observed around the Fermi level as shown in Figure 1(b). The valence band maximum touches the Fermi level around the Z point [Figure 1(c)]. The band structure of SnSe and Na-doped SnSe is basically consistent with the band structure calculations as reported elsewhere [10]. There are recent ARPES works on SnSe by Wang et al. [11] and Pletikosić et al. [12]. In the present work, the energy position of the valence band maximum is ~ 200 meV below the Fermi level. On the other hand, it is located at the Fermi level in the work by Wang et al. [11] indicating that the SnSe crystals by Wang et al. are hole doped due to some defects. In the study by Pletikosić et al. [12], it is located ~ 120 meV below the Fermi level which is slightly smaller than the present result. After confirming the band structure, we performed ARPES for SnSe and Na-doped SnSe with changing temperature. From changing temperature, the chemical potential shift of SnSe and Na-doped

SnSe are estimated. The large chemical potential shift of SnSe is consistent with that of undoped semiconductors. On the other hand, the chemical potential shift of Na-doped SnSe is also large compared to that expected for degenerate semiconductors. Although the observed band structure of Na-doped SnSe is consistent with the electrical conductivity expected for a degenerate semiconductor, the large chemical potential shift and the large Seebeck coefficient of Na-doped SnSe indicate that the carriers in Na-doped SnSe have localized character.

FIGURE 1. (a) Crystal structure of SnSe created by VESTA[3]. (b) Mapping of the ARPES intensity at the valence ban maximum in the BZ of Na-doped SnSe. (c) Energy versus momentum maps along the Γ-Z direction (k_z cut) for Na-doped SnSe.

CONCLUSION

In conclusion, the present ARPES study has revealed that the valence band top of SnSe reaches the Fermi level by the Na doping, and that Na-doped SnSe can be viewed as a degenerate semiconductor. This behavior is consistent with the canonical hole doping in semiconductors and with the electrical conductivity of Na-doped SnSe. However, in Na-doped SnSe, the chemical potential shift with temperature is unexpectedly large, inconsistent with the degenerate semiconductor picture. The large chemical potential shift suggests that the holes in Na-doped SnSe cannot be described by a simple itinerant picture or by a simple impurity level picture.

REFERENCES

1. L.-D. Zhao, G. Tan, S. Hao, J. He, Y. Pei, H. Chi, H. Wang, S. Gong, H. Xu, V. P. Dravid, C. Uher, G. J. Snyder, C. Wolverton, and M. G. Kanatzidis, Science **351**, 141 (2016).
2. T. Chattopadhyay, J. Pannetier, and H. G. Von Sshnering, J. Phys. Chem. Solids **47**, 879 (1986).
3. K. Momma and F. Izumi, J. Appl. Crystallogr., **44**, 1272 (2011).
4. C. W. Li, J. Hong, A. F. May, D. Bansal, S. Chi, T. Hong, G. Ehlers, and O. Delaire, Nat. Phys. **11**, 1063 (2015).
5. L.-D. Zhao, S.-H. Lo, Y. Zhang, H. Sun, G. Tan, C. Uher, C. Wolverton, V. P. Dravid, and M. G. Kanatzidis, Nature **508**, 373 (2014).
6. R. Car, G. Ciucci, and L. Quartapelle, Phys. Sat. Sol. 86, 471 (1978).
7. L. Makinistian and E. A. Albanesi, Phys. Status Solidi B 246, 183 (2009).
8. K. Kutorasinski, B. Wiendlocha, S. Kaprzyk, and J. Tobola, Phys. Rev. B 91, 205201 (2015).
9. G. Shi and E. Kioupakis, J. App. Phys. 117, 065103 (2015).
10. M. Maeda, K. Yamamoto, T. Mizokawa, N. L. Saini, M. Arita, H. Namatame, M. Taniguchi, G. Tan, L. D. Zhao and M. G. Kanatzidis, submiited to Phys. Rev. B.
11. Z.Wang, C. Fan, Z. Shen, C. Hua, Q. Hu, F. Sheng, Y. Lu, H. Fang, Z. Qin, J. Lu, Z.-A. Xu, D. W. Shen, and Y. Zheng, arXiv:1706.10054v1.
12. I. Pletikosić, F. von Rohr, P. Pervan, P. K. Das, I. Vobornik, R. J. Cava, and T. Valla, arXiv:1707.04289v1.

Photon energy dependence of photoelectron intensity angular distribution of topological surface states

Daiki Matsumaru[a], Kenta Kuroda[a], Jiahua Cheng[b], Akio Kimura[b], Masahi Arita[c], Shik Shin[a], and Takeshi Kondo[a]

[a]*ISSP, University of Tokyo, Kashiwa, Chiba 277-8581, Japan*
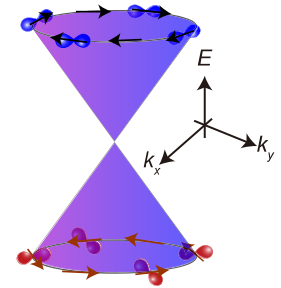[b]*Graduate School of Science, Hiroshima University, 1-3-1 Kagamiyama, Higashi-Hiroshima 739-8526, Japan*
[c]*Hiroshima Synchrotron Radiation Center, Hiroshima University, Higashi-Hiroshima, 739-0046, Japan*

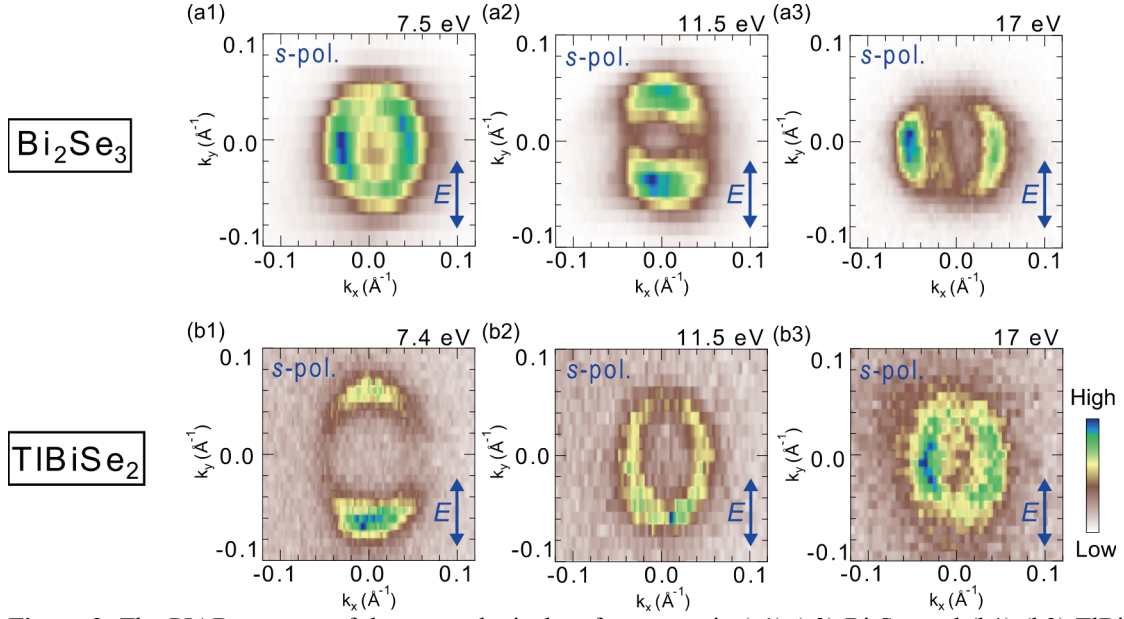**Keywords:** Topological insulator, Spin-orbit interaction, Surface-state

On the surface of solids, space inversion symmetry breaking combined with strong spin-orbit (SO) coupling lifts the spin-degeneracy. In the past decade, such spin-polarized states have been extensively investigated for Rashba surface states and topological surfaces states. In the conventional model to describe these states, the eigenstates split by the SO-interaction are treated as pure spin states, which are fully helical spin-polarized, thus protected from backscattering. However, this assumption is generally broken in real materials because the SO coupling can mix different orbital states with orthogonal spinors to generate an eigenstate of quasiparticles. Therefore, it is essentially important to experimentally explore the SO coupling effect not only on the lifting of spin degeneracy but also on the orbital wave-functions as eigenstates. Recently, some groups have reported, by using angle-resolved photoemission spectroscopy

Figure 1. Sketch of the spin-orbit coupling state in Dirac-cone-like topological surface state (in plene orbital componets) [1].

(ARPES) at 37-67 eV, evidence for this effect of SO coupling and its strong momentum dependence in a topological insulator Bi_2Se_3 [1]. In particular, the momentum dependence of the orbital components was deduced from the obtained photoelectron intensity angular distributions (PIAD), which was consistent with theoretical predictions (Fig. 1) [2].

In this study, we have performed ARPES with low-energy photons ranging over 6.4-21 eV at BL-9A of HiSOR, and directly mapped PIAD in the two topological insulators, Bi_2Se_3 and $TlBiSe_2$. We have obtained two important results: One is that the PIAD measured for the two materials at higher photon energies share the similar fearture which shows a good agreement with the previsouly reported orbital texture [1]. Second is that the PIAD, however, exhibits a significant photon energy dependence when the low photon energies below 17 eV are used. This dramatic photoen energy dependence suggests that complex matrix element effect contributes to the PIAD pariculary for the measurements at low photon energies.

Figure 2 presents the PIAD patterns of the topological surface states in Bi_2Se_3 (a1)-(a3) and $TlBiSe_2$ (b1)-(b3) obtained at various photon energies of s-polarized light. In Bi_2Se_3, we detect large intsties of photoelectrons around $(k_x, k_y)=(\pm k_F, 0)$ at 17 eV, while the intensity gets very weak around $(0, \pm k_F)$ [see Fig. 2 (a3)]. This PIAD pattern is consistent with that in the previous works

Figure 2. The PIAD patterns of the topogological surface states in (a1)-(a3) Bi$_2$Se$_3$ and (b1)-(b3) TlBiSe$_2$. These patterns were obtained by various photon energies and s-polaized light indicated by arrows.

[1], which attribute it to the momentum dependence of orbital component, so-called orbital-texture [2]. We observe the similar PIAD pattern in TlBiSe$_2$ at 17 eV [see Fig. 2 (b3)], and also no photon energy dependence at higer photon energies. On the basis of these resutls, we conculde that the SO coupling in these two materials establishes the smilar orbital texture.

Interestingly, we find that the PIAD pattern drastically changes in both materials when lower photon energies are used [Fig. 2(a1)-(a2) and (b1)-(b2)]. For example, in Bi$_2$Se$_3$, we see the different PIAD pattern at 11.5eV [see Fig. 2(a2)], in which the photoelectron itensityies get large around $(0, \pm k_F)$, but weaker around $(\pm k_F, 0)$ with a sharp contrast to the PIAD for 17 eV [Fig. 2(a3)]. At lower photon energies, the PIAD pattern is, however, found to show back to the same as that for 17 eV. Furtheremore, we find the similar photon energy dependence of the PIAD pattern in TlBiSe$_2$, [Fig. 2(b1)-(b2)]. Thease resutls indicate that the PIAD pattern can be changed by the photon energy pariculary less than 17 eV, probablly due to the matrix element effect. To unravel the origin of these PIAD patterns and their photon enery dependence, further systematic investigations combined with one-step theorey are strongly required.

REFERENCES
1. Y. Cao *et al*., Nat. Phys. **9**, 499-504 (2013).
2. H. Zhang *et al*., Phys. Rev. Lett. **111**, 066801 (2013).

Temperature dependence of the pseudogap in $Bi_2Sr_2Ca_2Cu_3O_{10+\delta}$ studied by angle-resolved photoemission spectroscopy.

S. Kunisada[a], S. Adachi[b], M. Nakayama[a], S. Akebi[a], M. Arita[c], T. Watanabe[b], and T. Kondo[a]

[a] *The Institute for Solid State Physics, Tokyo University, Kashiwa 277-8581, Japan*
[b] *Graduate School of Science and Technology, Hirosaki University, Hirosaki 036-8561, Japan*
[c] *Hiroshima Synchrotron Radiation Center, Hiroshima University, Higashi-Hiroshima 739-0046, Japan*
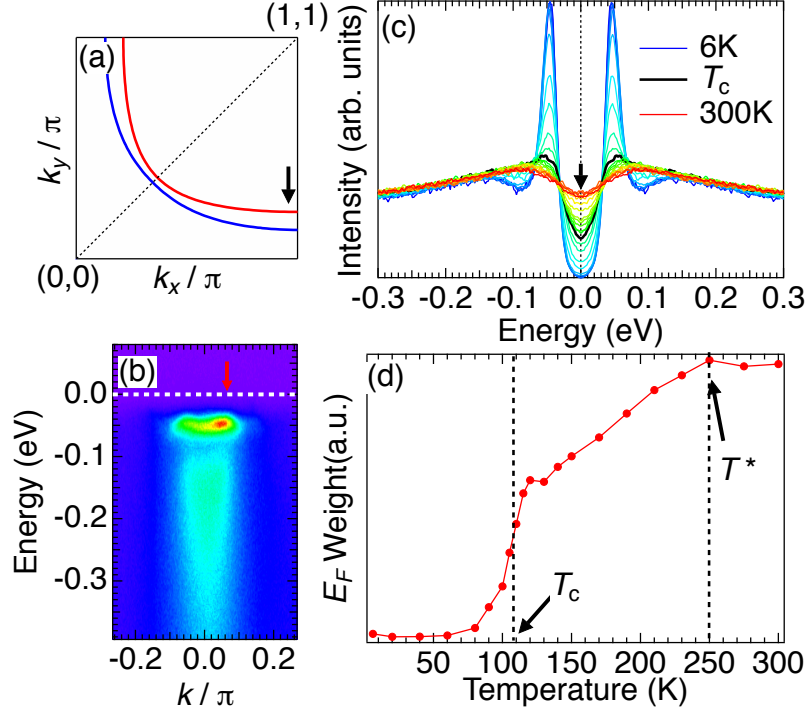
Keywords: copper oxide high-Tc superconductor, ARPES

While a huge effort has been made to elucidate the mechanism of high-transition-temperature (high-T_c) superconductivity in cuprates, the consensus on it has not reached yet. These materials significantly change physical properties with carrier doping. In particular, one of the most fascinating features in cuprates is pseudogap state, which appears in the underdoped regime. The pseudogap develops around $(\pi,0)$, and angle-resolved photoemission spectroscopy (ARPES) observes arc-like intensities of photoelectrons around the gap node. The understanding of this unique phenomenon is a hot topic in this field. There are manly two notions about the role of the psedgap state on the superconductivity: One is that it is a precursory phenomenon of superconducting state, and the other is that it is rather competing against superconducting state. It is crucial to fully understand the relationship between the psugogap and superconductivity to elucidate the mechanism of high-T_c superconductivity in cuprates.

In this study, we have performed ARPES measurements to investigate the temperature dependence of energy gaps (superconducting gap and pseudogap) in $Bi_2Sr_2Ca_2Cu_3O_{10+\delta}$ (Bi2223) with triple layers of CuO_2 in unit cell. Previous report on the same compound measured the antinodal spectra by using He Iα (21.218 eV) in the temperature range from 40K to 170K [1]. After this report, it was revealed that Bi2223 has actually two bands with different magnitudes of superconducting gap by using low photon energies (7-11eV) [2]. This anomaly in the trilayer system has been attributed to non-uniform distribution of doped carriers over the CuO_2 layers. It is therefore significant to investigate the behavior of superconducting gap and pseudogap at elevated temperatures for each band in Bi2223 to understand the nature of these gaps.

We have carried out ARPES measurements at BL-9A of Hiroshima Synchrotron Radiation center. The samples of single crystals were cleaved *in situ* to prepare a clean surface required to obtain sharp spectra. The photon energy used was $h\nu = 22\ eV$, which selectively observe the band with smaller superconducting gap. Energy resolution was set to 14 meV in our measurements.

The physical properties we focus on is the loss of spectral weight at the Fermi level (E_F) due to a gap opening [arrows in (c)]. Before extracting these values, the original spectra obtained are symmetrized about the Fermi level to eliminate the effect of Fermi cut-off near E_F. Moreover, each curve is normalized to its area in order to investigate the intrinsic temperature variation of the spectral weight. We found that the estimated values become constant at high temperatures, signifying that there is no gap at these temperatures. Our important finding is that a decrease of

the spectral weight at E_F due to a gap opening starts round 250K upon cooling. This result is consistent to the pseudogap temperature estimated from the resistivity behavior of Bi2223 [3].

Fig. 1. (a) Schematic Fermi surfaces in Bi2223. Red and blue curves indicate two different bands. (b) ARPES dispersions measured in the direction marked by an arrow in (a). (c) Temperature scan of EDCs at a k_F pointed by an arrow in (b) over a wide range from 6K up to 300K. The original spectra obtained are symmetrized about E_F to eliminate the Fermi cut-off. (d) Temperature variation of the spectral loss at the Fermi level [arrow in (c)].

In summary, we report ARPES studies on temperature dependence of Bi2223 around the antinode. We have investigated the temperature evolution of pseudogap at $h\nu = 22\ eV$, and obtained a pseudogap temperature higher than that in the previous report mostly owing to a precise estimation of it using detailed spectral weight. For the next step, we will investigate the other band with a higher superconducting gap by tuning photon energies especially around low energies (8-10 eV) to fully understand the nature of pseudogap state in Bi2223.

REFERENCES

1. T. Sato *et al.*, Phys. Rev. Lett. **89**, 067005 (2002).
2. S. Ideta *et al.*, Phys. Rev. Lett. **104**, 227001 (2010).
3. S. Adachi *et al.*, J. Phys. Soc. Jpn. **84**, 024706 (2015).

Self-energy in the superconducting states of the high-T_c cuprates Bi$_2$Sr$_2$CaCu$_2$O$_{8+\delta}$

T. Yoshida[a], D. Ootsuki[a], K. Yamawaki[a], D. Shimonaka[a], D. Shibata[a],
H. Eisaki[b], T. Sasagawa[c], A. Fujimori[d], M. Arita[e], H. Namatame[e], M. Taniguchi[e]

[a]Graduate School of Human and Environmental Studies, Kyoto University, Sakyo-ku, Kyoto 606-8501, Japan.
[b]National Institute of Advanced Industrial Scienceand Technology (AIST), Tsukuba305-8562, Japan
[c]Materials and Structures Laboratory, Tokyo institute of Technology, Yokohama, Kanagawa 226-8503, Japan
[d]Department of Physics, University of Tokyo, Bunkyo-ku, Tokyo 113-0033, Japan
[e]Hiroshima Synchrotron Radiation Center, Hiroshima University, Higashi-Hiroshima 739-0046, Japan

Keywords: high-T_c cuprates, Cooper pair, self-energy

While the energy scales of phonons appear in the superconducting gap function $\Delta(\omega)$ in conventional BCS superconductors, the $\Delta(\omega)$ of the high-T_c cuprate superconductors has not been investigated well by experimental studies because of the complexity in the d-wave superconducting gap. In previous angle-resolved photoemission (ARPES) studies, self-energy analyses have been done mostly in the nodal direction where the superconducting gap closes. In order to approach the information of the Cooper paring, the self-energy in the anti-nodal direction in the superconducting state is important. Several ARPES studies have reported the self-energy for the spectra with superconducting gap [1,2] and pointed out that there is bosonic structure in the self-energy. However, the origin of the bosonic mode has not been clarified yet.

Recently, the analysis of the two-dimensional Hubbard model calculated with the cellular dynamical mean-field theory (CDMFT) have shown that the energy scale of the pole in the normal and anomalous self-energies does not appear in the spectral function, while they have a pole at the same energy [3,4]. This is because the pole in the both self-energy cancels out each other in the total self-energy. The origin of the pole has been interpreted as composite fermions.
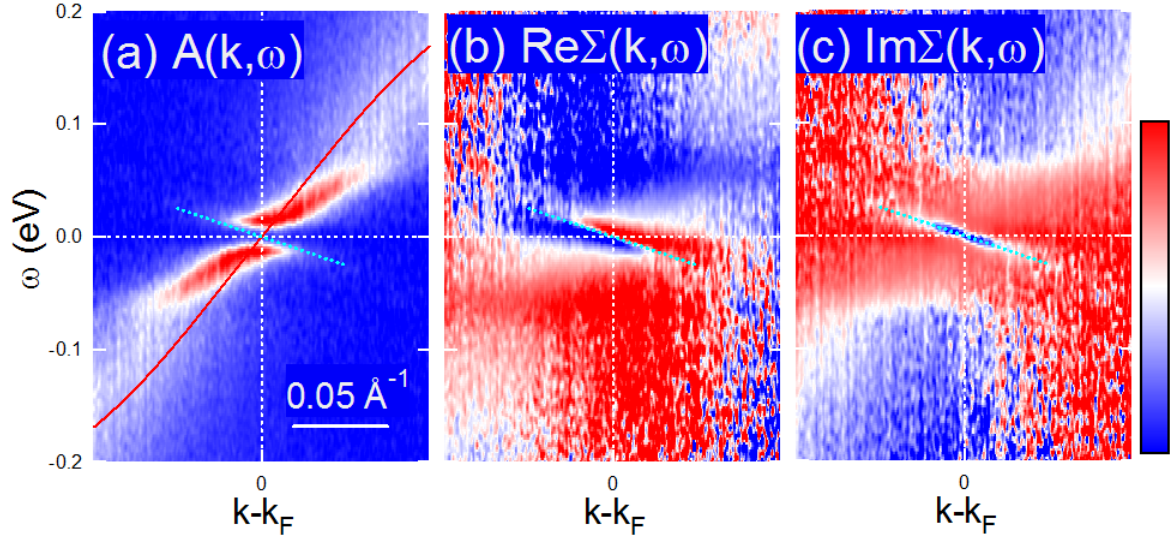
In the present study, we have performed ARPES study of the optimally doped Bi$_2$Sr$_2$CaCu$_2$O$_{8+\delta}$ (Bi2212) (T_c = 91 K) and have extracted the self-energy from the ARPES spectra. As shown in Fig. 1(a), the ARPES spectra in the off-nodal direction are symmetrized by assuming electron-hole symmetry. By applying the Kramers-Kronig transformation, we have obtained the total self-energy along the cut direction as shown in Figs. 1(b)(c). Here, bare electron band dispersion ε_k is assumed as indicated by red line in panel (a). In addition to ~70 meV kink structure, clear dispersive structure appears near the E_F.

Total self-energy $\Sigma_{tot}(k,\omega)$ in superconducting states is given by following formula

$$\Sigma_{tot}(\omega) = \Sigma_{nor}(\omega) + \frac{\Sigma_{ano}(\omega)^2}{\omega + \varepsilon_k + \Sigma_{nor}(-\omega)^*}$$

where $\Sigma_{nor}(\omega)$ and $\Sigma_{ano}(\omega)$ are normal and anomalous self-energy, respectively. In Figs. 1(b) and 1(c), the total self-energy shows a sharp and clear dispersive structure near the E_F as indicated by light blue dotted

lines. This structure is originated from the pole in the second term of the formula mentioned above and indicates a renormalized "hole" band near the E_F. Such a strong renormalization has been pointed out in previous self-energy analysis in the superconducting states [5] and may be related to small kink in the nodal direction [6]. While the renormalization near E_F has been interpreted as the effect of impurity scattering [5], the origin of the small kink in the nodal direction has been interpreted as phonon mode [6]. Such a low-energy mode appears in the superconducting states has important implications for the origin of the high-T_c superconductivity.

FIGURE 1. ARPES spectra of Bi2212 in the off-nodal direction taken at T = 10 K and total self-energy. (a) Symmetrized ARPES spectra corresponding to spectral function $A(k,\omega)$. (b) (c) Real and imaginary part of the total self-energy deduced from $A(k,\omega)$ by applying Kramers Kronig transformation.

REFERENCES

[1] M. R. Norman *et al.* Phys. Rev. B **60**, 7585 (1999).
[2] J. M. Bok *et al.*, Sci. Adv. **2**, e1501329 (2016).
[3] S. Sakai, M. Civelli, and M. Imada, Phys. Rev. Lett. **116**, 057003 (2016).
[4] S. Sakai, M. Civelli, and M. Imada, Phys. Rev. B **94**, 115130 (2016).
[5] S. H. Hong *et al.*, Phys. Rev. Lett. **113**, 057001 (2014).
[6] J. D. Rameau *et al.*, Phys. Rev. B **80**, 184513 (2009).